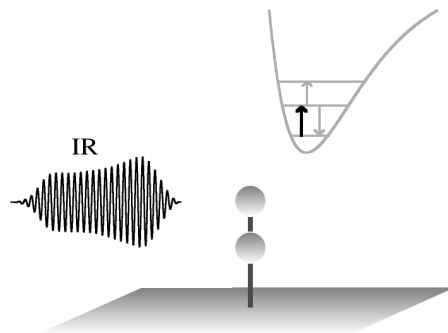


Selective excitation of adsorbate vibrations on dissipative surfaces



Dissertation

zur Erlangung des akademischen Grades

“doctor rerum naturalium”

(Dr. rer. nat.)

in der Wissenschaftsdisziplin Theoretische Chemie

eingereicht an der

Mathematisch-Naturwissenschaftlichen Fakultät

der Universität Potsdam

von

Stephanie Beyvers

aus Mallersdorf-Pfaffenberg

Potsdam, im Juli 2008

1. Gutachter:

Prof. Dr. P. Saalfrank

2. Gutachter:

Prof. Dr. T. Klüner

3. Gutachter:

Prof. Dr. R. Marquardt

Tag der Disputation: 29. Oktober 2008

This work is licensed under a Creative Commons License:
Attribution - Noncommercial - Share Alike 2.0 Germany
To view a copy of this license visit
<http://creativecommons.org/licenses/by-nc-sa/2.0/de/deed.en>

Online published at the
Institutional Repository of the Potsdam University:
<http://opus.kobv.de/ubp/volltexte/2008/2551/>
[urn:nbn:de:kobv:517-opus-25516](http://nbn-resolving.org/urn:nbn:de:kobv:517-opus-25516)
[<http://nbn-resolving.de/urn:nbn:de:kobv:517-opus-25516>]

Publications (7)

- 1 **“Quantum dynamics of laser-induced desorption from metal and semiconductor surfaces, and related phenomena”**
P. Saalfrank, M. Nest, I. Andrianov, T. Klamroth, D. Kröner, and S. Beyvers
J. Phys.: Condens. Matter **18**, 1425 (2006)

- 2 **“Optimal control in a dissipative system: Vibrational excitation of CO/Cu(100) by IR pulses”**
S. Beyvers, Y. Ohtsuki, and P. Saalfrank
J. Chem. Phys. **124**, 234706 (2006)

- 3 **“Mode-selective excitation of hydrogen atoms on a Si surface: Non-Markovian and Markovian treatment of infrared-laser driven dissipative quantum dynamics”**
G. K. Paramonov, S. Beyvers, I. Andrianov, and P. Saalfrank
Phys. Rev. B **75**, 045405 (2007)

- 4 **“Vibrationally enhanced associative photodesorption of molecular hydrogen from Ru(0001)”**
T. Vazhappilly, S. Beyvers, T. Klamroth, M. Luppi, and P. Saalfrank
Chem. Phys. **338**, 299 (2007)

- 5 **“A hybrid local / global control algorithm for dissipative systems with time-dependent targets”**
S. Beyvers and P. Saalfrank
J. Chem. Phys. **128**, 074104 (2008)

- 6 **“Selective excitation of coupled CO vibrations on a dissipative Cu(100) surface by shaped infrared laser”**
J. C. Tremblay, S. Beyvers, and P. Saalfrank
J. Chem. Phys. **128**, 194709 (2008)

- 7 **“Controlling the photodesorption of adspecies from surfaces”**
P. Saalfrank, T. Vazhappilly, S. Beyvers, G. K. Paramonov, and T. Klamroth
Surf. Sci. **602**, 3153 (2008)

Contents

1	Introduction	1
2	Theoretical methods	5
2.1	Stationary solution of the adsorbate/surface system	6
2.1.1	Time-independent Schrödinger equation	6
2.1.2	Solution	6
2.2	Dissipative dynamics: The Liouville-von Neumann equation	7
2.3	Dissipation model	10
2.3.1	Nonadiabatic molecular orbital theory for the calculation of vibrational lifetimes	10
2.3.2	Harmonic and anharmonic approaches for higher rates	13
2.4	Optimal control theory (OCT)	16
2.4.1	Global and local optimal control for wavefunctions	17
2.4.2	Global optimal control for density matrices	18

2.4.3	Pulse analysis by Husimi quasiprobability distribution	20
3	Adsorbate/surface systems	22
3.1	CO/Cu(100)	22
3.1.1	Potential energy surface and stationary solution	24
3.1.2	Dipole function	30
3.1.3	Dissipation and dephasing rates	33
3.2	H/Si(100)	38
3.2.1	Potential energy surface and vibrational states	38
3.2.2	Dipole function	39
3.2.3	Dissipation and dephasing rates	40
3.3	2H/Ru(0001)	43
3.3.1	Potential energy surface, stationary solution and dipole function . . .	43
3.3.2	Calculation of vibrational lifetimes	45
4	Control of vibrational excitation in dissipative systems	50
4.1	CO/Cu(100) [96,97]	51
4.1.1	One-dimensional model (r) [96]	51
4.1.2	Two-dimensional model (r,Z)	54
4.1.3	Three-dimensional model (r,Z,X) [96]	59

4.1.4	Four-dimensional model (r, Z, θ, ϕ) [97]	65
4.2	H/Si(100) [104]	70
4.2.1	One-dimensional model (r)	70
4.2.2	Two-dimensional model (r, ϕ) [104]	72
4.3	2H/Ru(0001) [111]	79
4.3.1	Excitation of the Z mode	80
4.3.2	Excitation of the r mode	82
5	Optimal control with time-dependent targets	85
5.1	Algorithm	86
5.2	Numerical tests	88
5.3	Applications	92
5.3.1	Creation and preservation of a wavepacket	92
5.3.2	Controlling a multi-level system	94
6	Summary	96
A	Numerical methods for solving the stationary problem	102
A.1	Sinc-function discrete variable representation	102
A.2	Fourier Grid Hamiltonian	105
A.3	Iterative two-term Lanczos eigensolver	107

B	Boundstate calculations for CO/Cu(100)	109
C	Numerical methods to solve the Liouville-von Neumann equation	113
D	Numerical method to solve the TDSE: The split-operator propagator method	118
E	Quantum chemical methods	119
E.1	Hartree-Fock theory	119
E.1.1	Hartree-Fock Equations	120
E.2	Density functional theory	121
E.2.1	Basics	121
E.2.2	Kohn-Sham equations	123
E.3	Effective core potentials	123
F	A new parametrization of the CO/Cu(100) dipole function	125
G	Non-Markovian theory	130
H	Local control of vibrational excitation in a non-dissipative system	134

Chapter 1

Introduction

Time-resolved monitoring of photochemical and photophysical processes in adsorbate systems has seen good progress in the past years [1,2]. Interesting in the context of this work is that the *selective* preparation of molecular vibrations by infrared (IR) light proves as a powerful tool to control the photoreactivity prior to electronic excitation by light in the ultraviolet/visible (UV/Vis) regime. This scheme is known as “vibrationally mediated chemistry” [3]. Extending this to adsorbates, it has been theoretically suggested that IR preexcitation will lead to larger UV/Vis photodesorption yields [4–9] as well as to larger cross sections for other photoreactions [8,10–12]. Particularly for adsorbate/metal systems this approach is promising as IR photons cannot penetrate the metal surface. They couple therefore directly to the adsorbate, thus are directly controllable and can be employed to vibrationally excite the adsorbate molecule. Ideally, the adsorbate vibrational excitation is state- or mode-selective in accordance with the “goal” of IR (pre)excitation.

It is even possible to induce photodesorption via IR radiation alone. Observed, some time ago, was the *thermal* desorption of NH_3 from Cu(100) [13], where the IR-excited N–H stretch bond (“antenna”) directs the radiation energy via surface phonons to the molecule-surface bond and eventually breaks it. There is no isotope selectivity (which supports the idea of a thermal mechanism): Co-adsorbed ND_3 desorbs as well. Contrary, Liu *et al.* [14] were able to selectively desorb molecular hydrogen from a Si(111) surface covered with atomic hydrogen and deuterium. This suggests a real vibrational mechanism of desorption, with the H–Si stretch bond as likely candidate to absorb the energy needed to break the bond with aid of

energy set free by the formed H–H bond.

The goal of the present thesis is to explore to what extent selective vibrational IR excitation is feasible in multi-dimensional adsorbate systems by means of pulsed IR light. Losses of selectivity and yield are possible due to inter-mode coupling and coupling to the “bath” (dissipation). Thereby, vibrations of the adsorbate (“system”) couple to phonons and, in case of metals, to electron-hole (e/h) pairs of the substrate (“bath”), energy and phase relaxation take place which counteracts IR excitation. If dissipation occurs (mainly) via the phononic channel, as is the case for insulators and semiconductors like silicon, the vibrations of the adsorbate have lifetimes in the order of milliseconds [15], nanoseconds [16–18] and down to picoseconds [19], depending on the availability of phonon energies fitting the respective vibrational quantum. For metals like copper or ruthenium, providing e/h pairs of energy differences suitable to vibrational quanta, vibrational lifetimes are normally considerably shorter, in the range from picoseconds [20] to some hundreds of femtoseconds [21]. This is problematic, as picoseconds are the “natural” timescale for the IR pulses used in the present work to vibrationally excite the adsorbate. Further, possible obstacles to IR excitation are weak dipole activities (“dark” modes) and a distinct harmonicity of certain modes. The latter does not hurt if only *mode*-selectivity is desired, as a single pulse of constant frequency (\sim resonant to the fundamental transition) allows to populate also higher lying states of the addressed mode. *State*-selectivity, *i. e.* population of a single vibrational level, however, is rendered difficult to impossible for harmonic modes. In order to achieve, nevertheless, maximum population in the target state (or mode), optimal control theory (OCT) [22–27] is used here to improve, as well as to compare to, simple \sin^2 -shaped pulses which are convenient as an initial “guess”.

The principle of OCT algorithms is to pre-define the final state of the system after the pulse is off and to iteratively (“global control”) or non-iteratively (“local control”) calculate a control field suitable to do so. A drawback of most OCT schemes, particularly of those designed for dissipative scenarios [28–30], is the time-independence of the so-called target operator. That is, one cannot control the transient population dynamics as to impose a certain “mechanism” of excitation, only the final outcome can be controlled. The time-dependent control of populations and/or coherences (quantum interferences between vibrational states) would be of particular interest for quantum computing employing vibrationally excited states as “qubits” [31,32]. OCT algorithms for dissipative systems which contain an explicitly time-dependent target operator are still rare [33]. The algorithm of Ref. [33], however, requires further parameters to guarantee monotonic convergence and has been tested only on small

models (up to four vibrational states) so far. Therefore a novel algorithm is presented here which combines the iterative OCT scheme and local control theory [34, 35], preserving the advantages (good target yields, monotonic and quadratic convergence) of the (global) OCT algorithm [30] it is based on, but being less demanding in computational memory requirements and allowing to explicitly give forth a target operator for each point in time.

Three adsorbate/surface systems are investigated in this work:

- CO/Cu(100) for which a full-dimensional potential energy surface (PES) [36, 37] as well as theoretical [36, 37] and experimental [20] vibrational lifetimes are accessible. Being well-studied (see for example Refs. [38–45]) and exhibiting lifetimes for the different modes and bath temperatures ranging from >100 to about two picoseconds, CO/Cu(100) serves as ideal, multi-dimensional model for the attempt of state-selective vibrational IR excitation.
- H₂/Ru(0001) for which likewise a full-dimensional PES [46, 47] exists as well as estimates [21, 48] for vibrational lifetimes. In experiment, femtosecond-laser (UV) induced photoreactions have been carried out [21, 49, 50]. There are indications that the associative desorption of hydrogen proceeds via a “hot electron” mechanism which promises to be enhanced by a IR+UV strategy.
- H/Si(100), which has been previously studied theoretically [51, 52], providing vibrational lifetimes in good agreement with experimental findings [53], is an interesting microlab for phenomena in fundamental and applied surface science. Most striking, the experiment [14] in the similar system H/Si(111), where molecular hydrogen is selectively desorbed from H+D/Si(111), proceeds very likely by an IR-induced *vibrational* mechanism.

Density matrix theory [54] is a very powerful technique to treat “open systems” in general, and for the special case of vibrational IR excitation of adsorbates at dissipative surfaces it already has proven successful in the past [9–12, 55, 56]. Thus, reduced density matrices are used here to solve the (Liouvillian) dynamics within the Markovian approximation and the Lindblad [57] form of dissipation. Further, to investigate the effect of neglecting the so-called “memory effects” within the Markov approximation, comparisons to non-Markovian calculations are also presented and discussed.

This work is organized as follows. Chapter 2 summarizes the employed theoretical methods and models, with Appendices A, C and D providing further details on the numerical methods used to solve the stationary, vibrational problem as well as dissipative and non-dissipative dynamics. An overview of quantum chemistry methods needed to calculate vibrational lifetimes according to Refs. [36, 37] is given in Appendix E. Chapter 3 presents the stationary solutions (see also Appendix B) of the adsorbate/metal systems listed above, considering up to four-dimensional models for the adsorbate vibration. Shown further is the calculation of other quantities (dipole transition moments, rates for energy and phase relaxation) needed to solve the dynamics. An example of how one can obtain a dipole function from quantum chemistry calculations on cluster models of the adsorbate/metal system is reviewed in Appendix F. Chapter 4 presents the calculations performed to state-/mode-selectively IR-excite adsorbate vibrations for various dimensionalities of the treated systems and with dissipation included. Both (sub)ps \sin^2 -shaped pulses and pulses obtained from global OCT are employed. The effects of various parameters (pulse duration, bath temperature, pure dephasing, target operator set-up) and interesting applications (“hot-band” excitation, excitation of combination mode states, high-energetic “ladder climbing”, “dark mode” excitation, exploitation of dissipation for vibrational excitation) are studied. Appendix G thereby introduces the non-Markovian theory used for comparison in case of H/Si(100) and Appendix H presents local control calculations carried out for CO/Cu(100), neglecting dissipation, in order to gain experience with time-scales, control fields and the system itself. Chapter 5 presents the novel, hybrid local/global OCT algorithm, numerical tests and first applications to excitation scenarios of interest in “time-dependent control”. Chapter 6, finally, summarizes the work and hints at future developments.

Chapter 2

Theoretical methods

In the following, the theoretical models and methods are described which are used to simulate vibrational IR excitation of molecules adsorbed on dissipative surfaces and to achieve the creation of suitable pulsed light for state or mode selectivity.

Section 2.1 treats the set-up and numerical solution of the field-free “system”, that is the adsorbed molecule as a multi-dimensional oscillator. The semiclassical interaction of the molecule with the electric field as well as the inclusion of the “bath”, *e. g.*, the surface’s electronic and phononic degrees of freedom, via an open-system density matrix description is expounded in Sec. 2.2. The non-adiabatic molecular orbital model to gain vibrational lifetimes and the harmonic and anharmonic schemes to realize energy and phase relaxation rates are presented in Sec. 2.3. Finally, in Sec. 2.4, global and local optimal control schemes for calculating the pulsed IR light are reviewed as well as the preferred method to analyse complex fields – the Husimi transformation.

2.1 Stationary solution of the adsorbate/surface system

2.1.1 Time-independent Schrödinger equation

As the dynamical treatment of IR-induced vibrational excitation is done in this work in the basis of adsorbate vibrational states $|\phi_{n_i}\rangle$, the field-free time-independent Schrödinger equation

$$\hat{H}_0|\psi\rangle = E|\psi\rangle \quad (2.1)$$

is solved in system eigenstate representation

$$\hat{H}_0|\phi_{\underline{n}}(\underline{q})\rangle = E_{\underline{n}}|\phi_{\underline{n}}(\underline{q})\rangle \quad . \quad (2.2)$$

According to the dimensionality F considered, $\underline{n} = (n_1, n_2, \dots, n_F)$ and $\underline{q} = (q_1, q_2, \dots, q_F)$ are F -tuples of quantum numbers n_i and vibrational coordinates q_i , respectively. (Note, that the unique assignment of quantum numbers n_1, \dots, n_F is normally only possible for low-lying states.) $E_{\underline{n}}$ are the eigenvalues of the system, constituting the vibrational energy ladder. The field-free Hamiltonian \hat{H}_0 consists of the (vibrational) kinetic energy operator \hat{T} and the potential energy V as a function of coordinates \underline{q}

$$\hat{H}_0 = \hat{T} + V(\underline{q}) \quad . \quad (2.3)$$

2.1.2 Solution

There are various approaches to solve the time-independent Schrödinger equation; mostly used in the present work are the sinc-function DVR (discrete variable representation) and the Fourier Grid Hamiltonian (FGH) methods, which numerically represent the Hamiltonian of Eq.(2.3) on a grid, simplifying the diagonalization in order to obtain the eigenvalues $E_{\underline{n}}$ and eigenvectors $\phi_{\underline{n}}(\underline{q})$. Both methods are summarized in Appendix A.

2.2 Dissipative dynamics: The Liouville-von Neumann equation

Describing the time-evolution of a quantum system by the time-dependent Schrödinger equation (TDSE)

$$i\hbar \frac{\partial}{\partial t} |\psi(t)\rangle = [\hat{H}_0 - \hat{\mu}F(t)] |\psi(t)\rangle \quad , \quad (2.4)$$

where $F(t)$ is the external electric field driving the system and $\hat{\mu}$ the dipole operator coupling field and system¹, is only possible for closed systems (no energy/phase exchange with a “bath”) and pure states ($T = 0$ K) which can be expressed by a single state vector. Contrary, a system at $T > 0$ K is a so-called thermal ensemble, composed of the eigenstates of \hat{H}_0 (denoted $|\phi_i\rangle$ or $|i\rangle$ for short), each populated according to the Boltzmann weight by

$$p_i = \frac{e^{-\frac{E_i}{k_B T}}}{\text{Tr}[e^{-\frac{\hat{H}_0}{k_B T}]} \quad , \quad (2.5)$$

with k_B being the Boltzmann constant and the sum of populations $\sum_i p_i = 1$. In a closed scenario, that is an external field may drive the system but no energy dissipation from the system to a “bath” occurs, the dynamics can still be solved in the wave packet representation of Eq. (2.5). Thereby, one first has to propagate a TDSE for every thermally populated initial wavefunction according to

$$|\psi_i(t)\rangle = e^{-\frac{i\hat{H}t}{\hbar}} |\phi_i\rangle \quad , \quad (2.6)$$

where $\hat{H} = \hat{H}_0 - \hat{\mu}F(t)$. Then the desired time-dependent observables $\langle \hat{A} \rangle(t)$ can be retrieved from incoherent averaging [58, 59]

$$\langle \hat{A} \rangle(t) = \sum_i p_i \langle \psi_i(t) | \hat{A} | \psi_i(t) \rangle \quad . \quad (2.7)$$

An alternative to incoherent averaging, is to represent the system of interest in terms of a density operator $\hat{\rho}(t)$ [60–62] and carrying out a single propagation of this object. To be more specific, here a reduced density operator for the system S is considered where the bath modes (B) have been “traced out”, *i. e.* $\hat{\rho} = \hat{\rho}_S = \text{Tr}_B\{\hat{\rho}\}$ – a trace over all degrees of freedom

¹The vector character of both electric field and dipole operator is omitted here for simplicity. Further, the semiclassical dipole approximation is made for the matter-field interaction.

of the bath. The concept of a reduced density operator is useful if *open* quantum systems are of interest (see below). For thermal ensembles, the initial density $\hat{\rho}(0)$ is constructed from the vibrational eigenstates $|\phi_i\rangle$ and the Boltzmann weights of Eq. (2.5) as

$$\hat{\rho}(0) = \sum_i p_i |\phi_i\rangle\langle\phi_i| \quad (2.8)$$

and it is propagated according to the Liouville-von Neumann (LvN) equation

$$i\hbar \frac{\partial}{\partial t} \hat{\rho}(t) = \mathcal{L}_0 \hat{\rho}(t) \quad (2.9)$$

with the formal solution

$$\hat{\rho}(t) = e^{-\frac{i}{\hbar} \mathcal{L}_0 t} \hat{\rho}(0) \quad . \quad (2.10)$$

\mathcal{L}_0 is the Liouville super-operator corresponding to the system Hamiltonian \hat{H}_0 which acts on the density operator in the form of a commutator

$$\mathcal{L}_0 \hat{\rho} = \left[\hat{H}_0, \hat{\rho} \right] \quad . \quad (2.11)$$

Extending this to cases where semiclassical system field interaction enters in the Hamiltonian via the term $-\hat{\mu}F(t)$, \mathcal{L}_0 has to be replaced by \mathcal{L}_H

$$\mathcal{L}_H \hat{\rho} = \left[\hat{H}_0 - \hat{\mu}F(t), \hat{\rho} \right] \quad . \quad (2.12)$$

Further, for open systems, where energy and phase information dissipates from “system” (here: adsorbate vibrations) to the “bath” (electronic and phononic degrees of freedom of the surface), a total Liouvillian $\mathcal{L} = \mathcal{L}_H + \mathcal{L}_D$ has to be formulated, where \mathcal{L}_D governs the dissipative contributions to the dynamics of the system. The corresponding open-system LvN equation is

$$i\hbar \frac{\partial \hat{\rho}(t)}{\partial t} = (\mathcal{L}_H + \mathcal{L}_D) \hat{\rho}(t) \quad (2.13)$$

For the dissipative part, the Lindblad [57] approximation

$$\mathcal{L}_D \hat{\rho} = i\hbar \sum_{j=1}^K \left(\hat{C}_j \hat{\rho} \hat{C}_j^\dagger - \frac{1}{2} \left[\hat{C}_j^\dagger \hat{C}_j, \hat{\rho} \right]_+ \right) \quad (2.14)$$

is used, where $[\cdot, \cdot]_+$ denotes an anti-commutator. The Lindblad form has the advantage that the diagonal elements of the density matrix remain positive and the trace is conserved², thus allowing for a physical interpretation of the diagonal elements as state populations. Each j of Eq. (2.14) thereby is one of K dissipative channels with \hat{C}_j being the associated Lindblad operator, which can be chosen semi-phenomenologically as to describe the dissipative process occurring for this channel, see for example Ref. [64].

When the LvN equation (2.13) is represented in the basis of the vibrational eigenstates $|\phi_i\rangle$ of \hat{H}_0 the Lindblad form of \mathcal{L}_D delivers the following equations of motion for the diagonal (population) matrix elements

$$\frac{d\rho_{nn}}{dt} = -\frac{i}{\hbar}F(t) \sum_{i=1}^N (\mu_{ni}\rho_{ni} - \rho_{ni}\mu_{in}) + \sum_{i=1}^N (\Gamma_{i\rightarrow n}\rho_{ii} - \Gamma_{n\rightarrow i}\rho_{nn}) \quad (2.15)$$

and off-diagonal (coherence) matrix elements

$$\frac{d\rho_{mn}}{dt} = -i\omega_{mn} - \frac{i}{\hbar}F(t) \sum_i^N (\mu_{mi}\rho_{in} - \rho_{mi}\mu_{in}) - \gamma_{mn}\rho_{mn} \quad . \quad (2.16)$$

N is the number of vibrational states and n, m are the numbering of these states. The μ_{mn} are the dipole transition moments between two states $|m\rangle$ and $|n\rangle$, that is $\mu_{mn} = \langle m|\hat{\mu}|n\rangle$. The vibrational frequencies $\omega_{mn} = \frac{E_m - E_n}{\hbar}$ follow from the vibrational eigenenergies E_m, E_n and the density matrix elements ρ_{mn} are set up from the vibrational eigenstates $|m\rangle$ and $|n\rangle$ as $\rho_{mn} = \langle m|\hat{\rho}|n\rangle$. According to Eq. (2.15), energy dissipates from state $|m\rangle$ to state $|n\rangle$ with a rate $\Gamma_{m\rightarrow n}$. This corresponds to the choice

$$\hat{C}_j \rightarrow \hat{C}_{mn} = \sqrt{\Gamma_{m\rightarrow n}}|n\rangle\langle m| \quad (2.17)$$

for the Lindblad operators in Eq. (2.15). Further, Eq. (2.16) includes dephasing, that is the decay of the off-diagonal density matrix elements which contain the information of coherence between two states, with a rate of $\gamma_{mn} = \gamma_{nm}$. For a N -level system, one has [65, 66]

$$\gamma_{mn} = \frac{1}{2} \sum_i^N (\Gamma_{m\rightarrow i} + \Gamma_{n\rightarrow i}) + \gamma_{mn}^* = \gamma'_{mn} + \gamma_{mn}^* \quad , \quad (2.18)$$

²Within the Redfield theory [63] and Markov approximation (neglect of “memory effects” in time-evolution of $\hat{\rho}$, see for example Ref. [54]), the individual diagonal elements of the density matrix are not necessarily positive, but the trace is automatically conserved, *i. e.* $\sum_i \rho_{ii} = 1$. In the Lindblad picture positivity is inherent (strictly only for the time-independent case), but trace-conservance has to be achieved by construction.

where the first term on the right-hand side is dephasing associated with inelastic processes (*i. e.*, energy relaxation), while the last term is due to pure dephasing, *i. e.* elastic scattering events.

The numerical solution of the coupled differential equations (2.15) and (2.16) with a given field $F(t)$, as employed here throughout, is summarized in Appendix C.

2.3 Dissipation model

2.3.1 Nonadiabatic molecular orbital theory for the calculation of vibrational lifetimes

The vibrational relaxation rates $\Gamma_{m \rightarrow n}$ are related to vibrational lifetimes. Finite lifetimes of adsorbates are due to the coupling of the adsorbate vibrations to either e/h pairs (for metal surfaces) or to phonons (all surfaces). For metal surfaces, the former dominates in most cases.

Experimental values of vibrational lifetimes are rare. For example, in case of the system CO/Cu(100) only that of the C-O stretch mode is known [20] to be (2 ± 1) ps at 120 K. Therefore we use a model suited to calculate the lifetime of the first excited state $|v = 1\rangle$ of a normal mode q with respect to the ground state $|v = 0\rangle$ obtained by quantum chemistry calculations on metal clusters.

The foundation of this model developed by Tully and co-workers [36, 37] with vibrational relaxation via an electronic mechanism as non-adiabatic process [67], is the Golden Rule of Time-Dependent Perturbation Theory [68]. Accordingly, the rate for relaxation from vibrational state $|v = 1\rangle$ to $|v = 0\rangle$ is

$$\tilde{\Gamma} = \frac{1}{\tau_{|v=1\rangle \rightarrow |v=0\rangle}} = \frac{1}{\tau} = \frac{2\pi}{\hbar} \sum_f |H_{fi}|^2 \delta(\epsilon_i - \epsilon_f) \quad . \quad (2.19)$$

Here, ϵ_i and ϵ_f are the energies corresponding to the initial state $|\psi_i\rangle \equiv |i\rangle$ and final states $|\psi_f\rangle \equiv |f\rangle$ of the system, the Dirac δ -function ensuring energy conservation, and H_{fi} is the matrix element connecting a pair of initial and final states. The states $|\psi_n\rangle$ are expanded as Born-Oppenheimer (B.O.) products [69] of the vibrational wavefunction $|v_n\rangle$ which depends on the normal mode coordinate q , and the electronic wavefunction $|e_n\rangle$, depending on the

electronic coordinates \underline{r} and parametrically on the vibrational coordinate q . Further, by inserting the nuclear kinetic energy operator $\hat{T}_q = -\frac{\hbar^2}{2\mu_q} \frac{d^2}{dq^2}$ as coupling operator, H_{fi} reads

$$\begin{aligned} H_{fi} &= \left\langle v_f \left| \langle e_f | \hat{T}_q | e_f \rangle_{\underline{r}} \right| v_i \right\rangle_q \quad (2.20) \\ &= -\frac{\hbar^2}{2\mu_q} \left\langle v_f \left| \langle e_f | e_i \rangle_{\underline{r}} \frac{d^2}{dq^2} \right| v_i \right\rangle_q - \frac{\hbar^2}{2\mu_q} \left\langle v_f \left| \langle e_f | \frac{d^2}{dq^2} | e_i \rangle_{\underline{r}} \right| v_i \right\rangle_q \\ &\quad - \frac{\hbar^2}{\mu_q} \left\langle v_f \left| \langle e_f | \frac{d}{dq} | e_i \rangle_{\underline{r}} \frac{d}{dq} \right| v_i \right\rangle_q, \end{aligned}$$

where the $\langle \dots \rangle_q$ and $\langle \dots \rangle_{\underline{r}}$ indicate an integration over nuclear coordinate q and electronic coordinates \underline{r} , respectively.

The first term of Eq. (2.20) vanishes due to the orthogonality of electronic states. The second term can be neglected if the $\langle e_f | \frac{d^2}{dq^2} | e_i \rangle$ are assumed to be vanishingly small. Expanding the inner bracket of the third term in (2.20) as Taylor series around ($q = 0$) and truncating this after the first term, one obtains

$$H_{fi} = -\frac{\hbar^2}{\mu_q} \left\langle e_f \left| \frac{d}{dq} \right| e_i \right\rangle_{q=0} \left\langle v_f \left| \frac{d}{dq} \right| v_i \right\rangle_q. \quad (2.21)$$

By approximating the vibrational wavefunctions as harmonic oscillator functions, using the harmonic selection rule ($v_f = v_i - 1$) – decay of one quantum in normal mode q – and specifying $|v_i = 1\rangle$ and $|v_f = 0\rangle$, Eq. (2.21) becomes

$$H_{fi} = -\hbar \sqrt{\frac{\Delta}{2\mu_q}} \left\langle e_f \left| \frac{d}{dq} \right| e_i \right\rangle_{q=0}. \quad (2.22)$$

Here, $\left\langle v_f = 0 \left| \frac{d}{dq} \right| v_i = 1 \right\rangle_q = \frac{1}{\hbar} \sqrt{\frac{\mu_q \Delta}{2}}$ has been used, where Δ is the vibrational quantum $\hbar\omega$ and μ_q the reduced mass. Further, the excited electronic states of the metal $|e_f\rangle$ are approximated as singly excited determinants $|\Psi_a^r\rangle$ (an electron has been promoted from orbital a to orbital r) relative to the Hartree-Fock ground state $|\Psi_0\rangle$ being the initial electronic state $|e_i\rangle$. The expression (2.19), now in canonical molecular orbital (MO) representation, resulting from the above restrictions resembles the Configuration Interaction Singles (CIS) theory [70] and reads

$$\tilde{\Gamma} = \frac{1}{\tau} = \frac{\pi\hbar}{\mu_q} \Delta \sum_{r,a} \left| \langle \chi_r | \frac{d}{dq} | \chi_a \rangle \right|^2 \delta(\varepsilon_a - \varepsilon_r + \Delta), \quad (2.23)$$

with $|\chi_n\rangle$ being the molecular orbitals and ε_n their corresponding energies.

The model set up and the approximations made so far are summarized in Fig.2.1, where on the left the fundamental vibrational decay in the adsorbate's harmonic potential is shown,

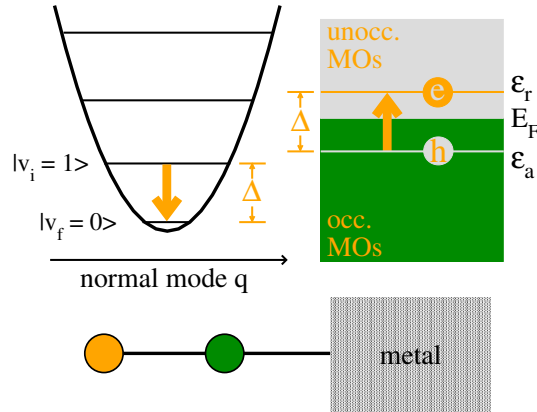


Figure 2.1: Nonadiabatic MO theory in schematic representation: The adsorbate modeled as harmonic oscillator, is decaying from the singly excited state $|v_i = 1\rangle$ to the vibrational ground state $|v_f = 0\rangle$, thereby emitting the vibrational quantum ($\Delta = \hbar\omega$). In the metal (represented here as MO “band” structure with occupied MOs forming the valence band, unoccupied MOs constituting the conduction band and the Fermi energy E_F separating the two) an electron is promoted from an orbital a in the valence band to an orbital r in the conduction band, creating an electron-hole pair, such as to fulfill the condition ($\varepsilon_r - \varepsilon_a = \Delta$) for energy conservation.

and on the right the excitation of a metal electron from a molecular orbital energetically below the Fermi level E_F to an unoccupied MO, and thereby creating an electron-hole (e/h) pair, is pictured.

Equation (2.23) can be expressed in a localized atomic orbital (AO) basis $|\mu\rangle$ ($|\chi_n\rangle = \sum_{\mu} C_{\mu n} |\mu\rangle$) to perform actual calculations. This results in the matrix equation $\underline{F}\underline{C}_n = \underline{S}\underline{C}_n\varepsilon_n$ from which Eq. (2.22) can be calculated and with \underline{F} being the Fock – or Kohn-Sham³ – matrix, \underline{S} the overlap matrix and $\underline{C}_n = (C_{1n}, C_{2n}, \dots)$. (For a brief review of Hartree-Fock and density functional theory and the Self Consistent Field (SCF) procedure by which quantum chemistry programmes solve HF and Kohn-Sham equations see Appendix E).

In AO basis and under the assumption that $\frac{d\varepsilon_a}{dq} = 0$ (no spatial dependence of MO energies) as well as using the already mentioned energy conservation condition, the vibrational

³Though the original algorithm was developed for Hartree-Fock orbitals it has been shown [71] that in CI calculations, it is possible to replace Hartree-Fock orbitals by Kohn-Sham orbitals.

relaxation rate is

$$\tilde{\Gamma} = \frac{1}{\tau} = \frac{\pi\hbar}{\mu_q\Delta} \sum_{a,r} \left(\underline{C}_a^\dagger \underline{W} \underline{C}_r \right) \left(\underline{C}_r^\dagger \underline{W} \underline{C}_a \right) \delta(\varepsilon_a - \varepsilon_r + \Delta) \quad , \quad (2.24)$$

with $\underline{W} = \frac{d}{dq} \underline{F} - E_F \frac{d}{dq} \underline{S}$. All derivatives with respect to q are performed at ($q = 0$) as these expressions originate from the Taylor expansion of the electronic part, see Eq. (2.21).

Introducing the density of states (DOS) at energy ϵ expressed in reduced one-particle density-matrix representation [70]

$$\underline{P}(\epsilon) = \underline{C}_n \underline{C}_n^\dagger \delta(\epsilon - \varepsilon_n) \quad (2.25)$$

and approximating a) that $\varepsilon_a \approx \varepsilon_r \approx E_F$, that is e/h pair creation occurs in a relatively small energy window around the Fermi level, and b) that the DOS can be considered smooth in an interval of width Δ , the final expression is a simple trace of a matrix product:

$$\tilde{\Gamma} = \frac{1}{\tau} = \frac{\pi\hbar}{\mu_q} \text{Tr} \left[\underline{P}(E_F^-) \underline{W} \underline{P}(E_F^+) \underline{W} \right] \quad . \quad (2.26)$$

For $\underline{P}(E_F^-)$ and $\underline{P}(E_F^+)$ – the DOS below and above the Fermi level, respectively – suitable occupied and unoccupied states have to be chosen within a certain energy window around E_F . These states have also to be broadened, for example by rectangular functions or Gaussians. Alternatively, Tully *et al.* [36] suggested the use of an “average density” $\underline{P}(E_F) = \frac{1}{2}(\underline{P}(E_F^-) + \underline{P}(E_F^+))$. Explicit examples of these procedures and their effect on the obtained rates are given in Section 3.3.2 for the system H₂/Ru(0001).

2.3.2 Harmonic and anharmonic approaches for higher rates

The model outlined in Sec. 2.3.1 delivers only the rate $\tilde{\Gamma}_j$ for the fundamental decay ($v = 1$) \rightarrow ($v = 0$) in a single, harmonic vibrational mode q_j . We also need rates for the decay of higher excited states ($v > 1$) as well as for the decay of a F -dimensional vibrational state $|m\rangle = |m_1, m_2, \dots, m_F\rangle$ to a state $|n\rangle = |n_1, n_2, \dots, n_F\rangle$ for the density matrix propagation (Sec. 2.2).

For a single harmonic vibration along coordinate q and at ($T = 0$ K), the electronic contribution to the relaxation rate $\tilde{\Gamma} = \Gamma_{1 \rightarrow 0}$ as calculated from Eq. (2.26) is [36]

$$\Gamma_{m \rightarrow n} = m \tilde{\Gamma} \delta_{m-1, n} \quad , \quad (2.27)$$

i. e. the harmonic selection rule ($m = n - 1$) is obeyed and the rate is proportional to the quantum number m of the decaying state. If additional phononic contributions enter, as here for CO/Cu(100) and ($T > 0$ K) [37], the same scaling law holds true if the rates arise from the Golden Rule (2.19), harmonicity is assumed and the vibration-phonon coupling is linear in q . This is the case in Ref. [37], from where the corresponding relaxation rates were taken.

For a multi-dimensional system of F normal modes j , neglecting inter-mode coupling, the scaling law of Eq. (2.27) for $\Gamma_{\underline{m} \rightarrow \underline{n}}$ can be generalized as

$$\Gamma_{\underline{m} \rightarrow \underline{n}} = \sum_{j=1}^F \tilde{\Gamma}_j m_j \delta_{(m_j-1, n_j)} \prod_{k \neq j}^F \delta_{m_k n_k} \quad . \quad (2.28)$$

Accordingly, only the decay ($m_j \rightarrow n_j = m_j - 1$) by a single quantum in a single mode j is possible at a time and the rate is proportional to the initial quantum number m_j of the decaying mode. To give an example, let's assume a two-mode system with modes A and B , a decaying state $|m_A = 1, m_B = 3\rangle$ and rates $\tilde{\Gamma}_A$ and $\tilde{\Gamma}_B$ as rates for the fundamental decay processes $|1, 0\rangle \rightarrow |0, 0\rangle$ and $|0, 1\rangle \rightarrow |0, 0\rangle$. There are only two non-zero relaxation rates of state $|1, 3\rangle$ according to Eq. (2.28)

$$\Gamma_{(1,3) \rightarrow (0,3)} = 1 \cdot \tilde{\Gamma}_A \quad (2.29)$$

$$\Gamma_{(1,3) \rightarrow (1,2)} = 3 \cdot \tilde{\Gamma}_B \quad , \quad (2.30)$$

so that the lifetime of state $|1, 3\rangle$ at ($T = 0$ K) is $[\Gamma_{(1,3) \rightarrow (0,3)} + \Gamma_{(1,3) \rightarrow (1,2)}]^{-1} = [\tilde{\Gamma}_A + 3\tilde{\Gamma}_B]^{-1}$.

This model is reasonable for the treatment of low-energetic IR-excitation, that is in a regime where the system can be considered harmonic and the coupling between system and bath is linear in the system modes. In higher energetic anharmonic regimes (for example ladder climbing in a desorptive mode up to the desorption limit), Eq. (2.28) overestimates the rates with increasing quantum numbers. Therefore an anharmonic correction as proposed in Ref. [72] can be used

$$\Gamma_{\underline{m} \rightarrow \underline{n}} = \sum_{j=1}^F \tilde{\Gamma}_j \frac{(E_{\underline{m}} - E_0)}{\hbar \omega_j} \delta_{(m_j-1, n_j)} \prod_{k \neq j}^F \delta_{m_k n_k} \quad , \quad (2.31)$$

with ω_j being the harmonic fundamental frequency of normal mode j . Considering again the example of above, the rates by which state $|1, 3\rangle$ decays to states $|0, 3\rangle$ and $|1, 2\rangle$, respectively,

are

$$\Gamma_{(1,3)\rightarrow(0,3)} = \frac{E_{1,3} - E_{0,3}}{\hbar\omega_A} \cdot \tilde{\Gamma}_A \quad (2.32)$$

$$\Gamma_{(1,3)\rightarrow(1,2)} = \frac{E_{1,3} - E_{1,0}}{\hbar\omega_B} \cdot \tilde{\Gamma}_B \quad . \quad (2.33)$$

If modes A and B are both (uncoupled) harmonic oscillators then $E_{1,3} - E_{0,3} = \hbar\omega_A$ and $E_{1,3} - E_{1,0} = 3\hbar\omega_B$ and one obtains the same result as in case of the harmonic model of Eq. (2.28). Alternatively, one can generalize Eq. (2.20) to anharmonic vibrational wavefunctions and a less restricted electronic coupling form.

Eqs. (2.28) and (2.31) yield only the “downward” rates $\Gamma_{m\rightarrow n}$ for ($E_m > E_n$), but at finite temperatures ($T > 0$ K) there are also rates transferring population “upwards”; these are calculated from detailed balance

$$\Gamma_{n\rightarrow m} = \Gamma_{m\rightarrow n} e^{-\frac{E_m - E_n}{k_B T}} \quad . \quad (2.34)$$

Finally, for being able to solve the differential equations (2.15) and (2.16), the dephasing rates γ_{mn} are needed. As mentioned above, dephasing arises both from inelastic scattering processes (T_1 -type dephasing) and elastic scattering (molecule remains in state v , T_2^* -type “pure” dephasing).

The total dephasing rate (T_2 dephasing) between states $|n\rangle$ and $|m\rangle$ is the sum of T_1 and T_2^* dephasing, as indicated in Eq. (2.18). For a two-level system, with states $|0\rangle$, $|1\rangle$ one has, at ($T = 0$ K):

$$\gamma_{10} = \frac{1}{2}\Gamma_{1\rightarrow 0} + \gamma_{10}^* \quad . \quad (2.35)$$

γ_{10}^* can be estimated from if experimental linewidths; see for example Levinos *et al.* [20, 73]. In a two-state system

$$\frac{1}{T_2} = \frac{1}{2T_1} + \frac{1}{T_2^*} \quad (2.36)$$

is valid, and at ($T = 0$ K) $T_1 = \tau = \frac{1}{\Gamma}$ and thus

$$\gamma_{10}^* = \frac{1}{T_2} - \frac{1}{2}\tilde{\Gamma} \quad . \quad (2.37)$$

Further, if one assumes a Gaussian pure dephasing model, then the γ_{mn}^* are proportional to ω_{mn}^2 [74], and can be calculated based on γ_{10}^* and eigenstate energy differences.

2.4 Optimal control theory (OCT)

A \sin^2 -shaped pulse (or a “pulse train” of successive/overlapping \sin^2 -shaped pulses)

$$F(t) = F_0 \sin^2 \left(\frac{\pi t}{t_f} \right) \cos(\omega t + \phi) \quad (2.38)$$

can be suitable for IR excitations [8,10–12,75]. In Eq. (2.38), F_0 is the maximal field strength, ω the frequency and ϕ the phase of the pulse (train) which, for a single pulse, starts at ($t = 0$) and ends at ($t = t_f$). Again, the vector character of the field is omitted for simplicity.

For a direct transition $|n\rangle \rightarrow |m\rangle$, a first simple guess for the electric field is a π pulse with $\omega = \omega_{mn}$ and a maximum field strength ($F_0 = F_0^\pi$), where

$$F_0^\pi = \frac{2\pi\hbar}{t_f |\mu_{nm}|} \quad (2.39)$$

and $\mu_{nm} = \langle n | \hat{\mu} | m \rangle$ is the transition dipole moment. Relation (2.39) derives from the condition

$$|\mu_{nm}| F_0^\pi \int_0^{t_f} s(t) dt = \hbar\pi \quad (2.40)$$

which assures that, within the rotating wave approximation (RWA) and with no dissipation involved, a complete population inversion is obtained in a two-state system. In Eq. (2.40) $s(t)$ is a general shape function, $\sin^2 \left(\frac{\pi t}{t_f} \right)$ in the present case.

For more delicate problems – *e.g.* strong dissipation, complicated/unknown “reaction pathways” in multi-level systems – the creation of pulses via optimal control theory [22–27] is helpful. Different to the Brumer-Shapiro coherent control scheme [76] which relies on the generation of suitable quantum interference of a number of energy levels, optimal control theory (OCT) is based on optimizing the shape of the control pulse via variational calculus as to meet the condition that the final outcome of dynamics approaches the predefined “target”. The OCT has been successfully applied for wavefunctions, see for example [26, 27, 31, 34, 77, 78, 78–83]. Progress has also been made in developing rapidly converging algorithms [84–87], formulating the formalism in Liouvillian space [28–30] and creating OCT pulses which allow for experimental reconstruction [34, 88].

2.4.1 Global and local optimal control for wavefunctions

In the global optimal control formalism as proposed by Rabitz *et al* [22–24], Kosloff *et al.* [26] and Manz *et al.* [25, 27] the control field $F(t)$ is generated variationally as to maximize the objective functional J

$$J = \langle \psi(t_f) | \hat{O} | \psi(t_f) \rangle - \alpha \int_0^{t_f} |F(t)|^2 dt - \int_0^{t_f} dt \left[\left\langle \chi(t) \left| \frac{\partial}{\partial t} + \frac{i}{\hbar} \hat{H} \right| \psi(t) \right\rangle + \text{c.c.} \right] . \quad (2.41)$$

Here, \hat{O} is the so-called target operator which can be generally expressed as

$$\hat{O} = \sum_{ij} o_{ij} |i\rangle \langle j| . \quad (2.42)$$

If a certain target state $|i\rangle$ is to be populated, the choice as a projection operator $\hat{O} = |i\rangle \langle i|$ is useful. The penalty factor α is a scalar factor here⁴ that restricts the pulse fluence in the second term of Eq. (2.41). α can also be chosen time-dependent as $\alpha(t)$ [80] as to obtain pulse shapes with $F(0) = F(t_f) = 0$ for experimental feasibility. In this case, $\alpha(t)$ appears in the integral as $-\int_0^{t_f} \alpha(t) |F(t)|^2 dt$. Further, the Lagrange multiplier $\chi(t)$ constrains the variational problem to obey the time-dependent Schrödinger equation (2.4) in the third term of Eq. (2.41). Providing both an initial condition $|\psi(0)\rangle = |\psi_0\rangle$ (normally chosen as the vibrational ground state) and final condition $|\chi(t_f)\rangle = \hat{O}|\psi(t_f)\rangle$, the optimal field at time t is

$$F(t) = -\frac{1}{\hbar\alpha} \text{Im} \langle \psi(t) | \hat{\mu} | \chi(t) \rangle . \quad (2.43)$$

Technically this global scheme requires an iterative algorithm where the wavefunction $\psi(t)$ is propagated forward in time and the Lagrange multiplier $\chi(t)$ backward in time (obeying Eq. (2.4) with χ instead of ψ and time being negative, *i. e.* $t \rightarrow -t$). The electric field is generated anew at each timestep from Eq. (2.43). Convergence is achieved if the field or the target state population do not change any more significantly from one backward/forward propagation to the next.

A different, but nonetheless often quite successful, approach is local control theory [34, 35, 78, 79]. Here, the initial state of the system is a fixed boundary condition like in global control

⁴The penalty term of Eq. (2.41) can also be chosen employing a further Lagrange multiplier; in this case the second term of Eq. (2.41) would take on the form $\alpha \int_0^{t_f} [|F(t)|^2 - \kappa] dt$, with the additional parameter κ being the Lagrange multiplier – a “target field intensity”.

(which is a two-point boundary value problem, but the outcome of dynamics is “open”, though triggered towards a specified goal by the target operator \hat{O}). The procedure is non-iterative and the pulse optimization occurs simultaneously to the *single* forward propagation. The target operator indirectly controls the path, as demonstrated in the examples of Appendix H.

As local control is a one-point boundary value problem ($|\psi(0)\rangle = |\psi_0\rangle$), Eq. (2.43) is reduced to

$$J = \langle \psi(t_f) | \hat{O} | \psi(t_f) \rangle - \frac{\alpha}{2} \int_0^{t_f} |F(t)|^2 dt \quad . \quad (2.44)$$

For small timesteps (within which the time-dependent Schrödinger equation is fulfilled) the optimal field can be approximated [35] as

$$F(t) = -\frac{2}{\hbar\alpha} \text{Im} \langle \psi(t) | \hat{O} \hat{\mu} | \psi(t) \rangle \quad , \quad (2.45)$$

an expression not unsimilar to (2.43) but containing \hat{O} which ensures the creation of a field driving the system towards the desired state. The continuity of the control pulse is guaranteed by assuming the commutator relation

$$[\hat{O}, \hat{H}_0] = 0 \quad (2.46)$$

between the target operator and the unperturbed Hamiltonian.

The above local control theory algorithm was implemented in such a way that the propagation of $|\psi(t)\rangle$ in accordance with the TDSE (2.4) is carried out by the split-operator propagator (SPO) method (see Appendix D for details) in contrast to the original implementation of Ohtsuki *et al.* [35], where the time-propagation is realized by the Runge-Kutta 4th order integrator [89, 90].

2.4.2 Global optimal control for density matrices

In order to include the possibility to treat open quantum systems, Ohtsuki *et al.* [30] developed a rapidly convergent algorithm extending the global OCT formalism as sketched in the first part of Sec. 2.4.1 into the Liouvillian space density matrix representation similar to Ref. [91]

but including dissipation. The objective functional, compare the analogy to Eq. (2.41), reads

$$J = \langle\langle \hat{O} | \hat{\rho}(t_f) \rangle\rangle - \int_0^{t_f} \alpha(t) |F(t)|^2 dt - \int_0^{t_f} dt \left\langle \left\langle \hat{\sigma}(t) \left| \frac{\partial}{\partial t} + \frac{i}{\hbar} [\mathcal{L}_H + \mathcal{L}_D] \right| \hat{\rho}(t) \right\rangle \right\rangle, \quad (2.47)$$

with the third term ensuring the Liouville-von Neumann equation (2.13) to be obeyed during the iterative forward and backward propagation-optimization within the interval $[0, t_f]$. Thereby the boundary condition for forward propagation of the density matrix according to (2.13) is

$$\hat{\rho}(0) = \hat{\rho}_0 = \frac{e^{-\frac{1}{k_B T} \hat{H}_0}}{\text{Tr} \left[e^{-\frac{1}{k_B T} \hat{H}_0} \right]} \quad (2.48)$$

i. e. a thermal ensemble of the N vibrational eigenstates $|i\rangle$. The Lagrange multiplier density $\hat{\sigma}(t)$ being propagated backward in time from $(t = t_f)$ to $(t = 0)$ has to obey

$$i\hbar \frac{\partial \hat{\sigma}(t)}{\partial t} = (\mathcal{L}_H + \mathcal{L}_D)^\dagger \hat{\sigma}(t) \quad (2.49)$$

and has as boundary condition at $(t = t_f)$ the target \hat{O} which is the desired density when the pulse is off. Formally expressed in the basis of vibrational eigenstates $\hat{O} = \hat{\sigma}(t_f)$ can be written as Eq. (2.42) with the o_{ij} , as already mentioned above, being the (real) target populations for $(i = j)$ and the target coherences for $(i \neq j)$. Often, again, the target is chosen as a single state $|i\rangle$, that is $\hat{O} = |i\rangle\langle i|$.

With the objective and boundary conditions given above the relation for the control field is

$$F(t) = -\frac{1}{\hbar\alpha(t)} \text{Im} \langle\langle \hat{\sigma}(t) | \hat{\mu} | \hat{\rho}(t) \rangle\rangle \quad (2.50)$$

In Eqs. (2.47) and (2.50) Hilbert-Schmidt scalar products $\langle\langle \hat{A} | \hat{B} \rangle\rangle = \text{Tr}\{\hat{A}^\dagger \hat{B}\}$ are used. As a result one obtains the following simple expression for the field:

$$\begin{aligned} F(t) &= -\frac{1}{\hbar\alpha(t)} \text{Im} \left[\text{Tr}\{\hat{\sigma}^\dagger(t) [\hat{\mu}\hat{\rho}(t)]\} \right] \\ &= -\frac{1}{\hbar\alpha(t)} \text{Im} \left[\sum_{i,j,k=0}^{N-1} \sigma_{ij}^*(t) \mu_{jk} \rho_{ki}(t) \right] \\ &= \frac{1}{\hbar\alpha(t)} \sum_{i,j,k=0}^{N-1} \mu_{jk} (\text{Im} [\sigma_{ji}(t)] \text{Re} [\rho_{ki}(t)] - \text{Re} [\sigma_{ji}(t)] \text{Im} [\rho_{ki}(t)]) \quad (2.51) \end{aligned}$$

This already hints at the “mechanism” of field creation in the optimal control scheme, but that becomes even more obvious when writing Eq. (2.51) for a two-state system ($N = 2$), where $\mu = \mu_{01} = \mu_{10}$ (and $\mu_{00} = \mu_{11} = 0$):

$$F(t) = -\frac{\mu \operatorname{Im}[\rho_{01}]}{\hbar\alpha(t)} (\operatorname{Re}[\sigma_{11}] - \operatorname{Re}[\sigma_{00}]) \quad . \quad (2.52)$$

The field at a given point in time is proportional to the product of the imaginary part of the coherence term ρ_{01} of the density matrix, which oscillates with resonance frequency ω_{10} , and the difference of populations σ_{11} and σ_{00} in the Lagrange multiplier density⁵. Similarly, though more complex, the magnitudes and oscillation frequencies of coherence terms and the differences of state populations determine the control field in systems with ($N > 2$). The “drive” towards the target enters only by the backward propagation of $\hat{\sigma}(t)$ starting from the target \hat{O} .

As for the computational realization of the global OCT, Ohtsuki *et al.* originally implemented a Runge-Kutta 4th order integrator [89,90] in order to solve the Liouvillian dynamics according to Eqs. (2.13) and (2.49). But due to numerical instabilities found for calculations already with a moderate number of vibrational states (say 10 or more), a new implementation was done, where the time-evolution is realized by spectral decomposition of the Liouvillian, Newton polynomial interpolation and Schwarz-Christoffel mapping [92,93] of the Liouvillian eigenvalue spectrum. See Appendix C for a summary of this technique.

2.4.3 Pulse analysis by Husimi quasiprobability distribution

Optimal electric fields obtained from optimal global or local control can have a complex structure. A Fourier transformation $I(\omega)$ of field $F(t)$

$$I(\omega) = \frac{1}{\sqrt{2\pi}} \int_{-\infty}^{\infty} F(t) e^{-i\omega t} dt \quad (2.53)$$

delivers only the relative intensities of occurring frequencies ω averaged over the whole pulse duration. One cannot draw any time-resolved information with respect to the frequencies from it.

⁵The backward propagated Lagrange multiplier density $\hat{\sigma}(t)$ behaves just like the forward propagated density $\hat{\rho}(t)$. In basis of the vibrational eigenstates $|i\rangle$, its diagonal matrix elements σ_{ii} can thus be physically interpreted as “populations”, as $\sigma_{ii} \in \mathbf{R}$ and $\sigma_{ii} \in [0, 1]$.

One possibility to resolve $F(t)$ in the time and energy ($E = \hbar\omega$) domain is the so-called Wigner quasiprobability distribution [94] $P_W(t, \omega)$

$$P_W(t, E) = \frac{N}{2\pi\hbar} \int_{-\infty}^{\infty} dq F^*(t + \frac{q}{2}) F(t - \frac{q}{2}) e^{\frac{iEq}{\hbar}} \quad , \quad (2.54)$$

with $N = \left(\frac{ea_0}{E\hbar}\right)^2$ being a normalization factor making $P_W(t, E)$ dimensionless. The Wigner distribution, however, can take negative values (“non-classic effects”), making the analysis somewhat difficult. Therefore, the Husimi distribution [95], being strictly positive, is preferred here. To obtain it the initially calculated Wigner distribution is smoothed by Gaussians in time and energy

$$P_H(t, E) = \frac{1}{\pi\hbar} \int dt' \int dE' e^{-\frac{\kappa(t'-t)^2}{\hbar}} e^{-\frac{\hbar(E'-E)^2}{\hbar\kappa}} P_W(t', E') \quad . \quad (2.55)$$

Here, $\kappa [(\text{energy} \times \text{time})^{-1}]$ is an arbitrary positive constant which is chosen as to obtain a suitable resolution. The product of uncertainties has to observe the Heisenberg criterion, that is $(t' - t)(E' - E) \geq \frac{\hbar}{2}$.

Chapter 3

Adsorbate/surface systems

The study of state- or mode-selective vibrational IR excitation is done here for a selection of adsorbate/surface systems. Three systems have been studied: CO/Cu(100), H/Si(100) and 2H/Ru(0001). These will be discussed in some detail in the following with respect to included vibrational degrees of freedom, potential energy surface, dipole function and the thereof obtained vibrational eigenstates, eigenenergies and dipole transition moments used in the quantum dynamics simulations.

3.1 CO/Cu(100)

CO adsorbed C-bound on-top of a Cu(100) surface serves as main system of interest in the present work. A full six-dimensional potential energy surface which has been fitted to semi-empirical data by Tully and co-workers [36, 37] exists and has proven in several theoretical studies [40–45] to deliver results close to experimental frequencies [39]. Further, the CO stretch mode has been studied in experiment. A vibrational lifetime of (2 ± 1) ps [20] was found and a linewidth, allowing to estimate the dephasing time T_2 as 1.6 ps [20, 73]. Although, these quantities are unknown for the other five modes, theoretical lifetimes have been calculated by Tully *et al.* based on the non-adiabatic molecular orbital model (Sec. 2.3.1). This was done for ($T = 0$ K) [36]; for finite surface temperatures ranging from 10 to 450 K they implemented an additional phononic decay channel by molecular dynamics simulation [37].

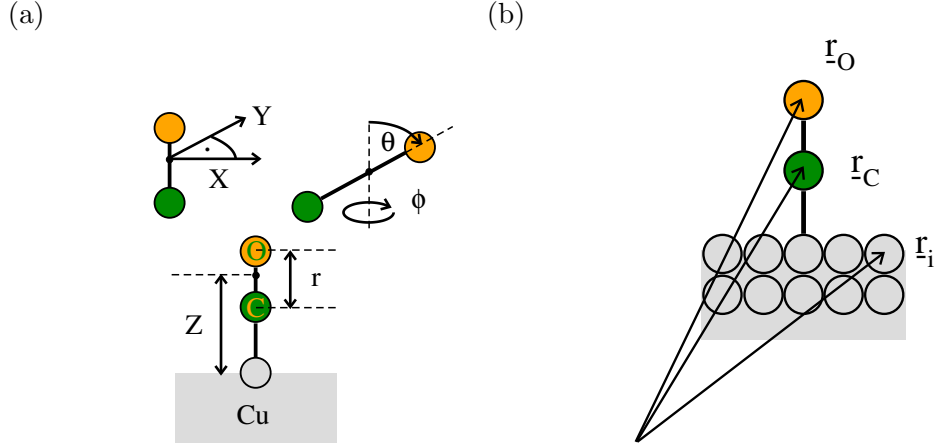


Figure 3.1: (a) The six degrees of freedom of CO adsorbed on-top on a Cu(100) surface: CO stretch mode r , CO-surface stretch mode Z , degenerate lateral motion along the $[1,1,0] \equiv X$ and $[-1,1,0] \equiv Y$ directions on the surface and angular degrees of freedom θ and ϕ ; (b) position vectors of C, O and i th Cu atom of the N atom metal slab modelling the surface.

Fig. 3.1 (a) displays a possible choice for the six vibrational modes of CO: The CO stretch mode r and the CO-surface stretch mode Z , the two degenerate lateral modes X and Y where the center of mass is displaced parallel to the surface in $[1,1,0]$ and $[-1,1,0]$ directions. Also shown are the two angular degrees of freedom θ and ϕ which describe the tilting of CO with respect to the vertical axis and the rotation around latter, respectively. The full 6D Hamiltonian \hat{H}_0 is

$$\hat{H}_0 = -\frac{\hbar^2}{2\mu} \frac{\partial^2}{\partial r^2} - \frac{\hbar^2}{2m} \frac{\partial^2}{\partial Z^2} - \frac{\hbar^2}{2m} \frac{\partial^2}{\partial X^2} - \frac{\hbar^2}{2m} \frac{\partial^2}{\partial Y^2} + \frac{\hbar^2}{2\mu r^2} \hat{J}(\theta, \phi) + V(r, Z, X, Y, \theta, \phi) \quad , \quad (3.1)$$

where $\mu = \frac{m_C m_O}{m_C + m_O}$ and $m = m_C + m_O$ are the reduced masses if surface atoms are fixed (rigid surface approximation). $\hat{J}(\theta, \phi)$ is the angular momentum operator

$$\hat{J}^2 = -\cot(\theta) \frac{\partial}{\partial \theta} - \frac{\partial^2}{\partial \theta^2} - \frac{1}{\sin^2(\theta)} \frac{\partial^2}{\partial \phi^2} \quad (3.2)$$

and $V(r, Z, X, Y, \theta, \phi)$, the 6D potential, introduced in the following.

Here, we have mainly restricted ourselves to two-dimensional (r, Z) and three-dimensional (r, Z, X) [96] models in order to gain insight whether a selective vibrational excitation is feasible at all. Further these three modes, as will be discussed later, are representative for strong, medium and weak IR active vibrational modes and cover a wide range of vibrational frequencies, from about 80 to 2150 cm^{-1} . In a recent collaboration [97], also four-dimensional (r, Z, θ, ϕ) dynamical simulations were carried out.

3.1.1 Potential energy surface and stationary solution

As potential energy surface, the empirical gas/surface interaction potential of Tully and co-workers [36, 37] is used:

$$V(r, Z, X, Y, \theta, \phi) = \sum_i^N V_i(\underline{r}_C, \underline{r}_O, \underline{r}_i) + V_{CO}(|\underline{r}_C - \underline{r}_O|) \quad . \quad (3.3)$$

This is composed of N terms $V_i(\underline{r}_C, \underline{r}_O, \underline{r}_i)$, describing the interaction between CO and the i th of the N copper atoms, and the term $V_{CO}(|\underline{r}_C - \underline{r}_O|)$ for the interaction between carbon and oxygen. Shown schematically in Fig. 3.1 (b) are the position vectors \underline{r}_C , \underline{r}_O and \underline{r}_i for the carbon, oxygen and i th copper atom in an N atom metal slab.

The adsorbate/surface interaction terms consist of a) a simple exponential repulsion between oxygen and copper atom and b) a modified Morse potential for the C/Cu interaction

$$V_i(\underline{r}_C, \underline{r}_O, \underline{r}_i) = A e^{-\alpha|\underline{r}_i - \underline{r}_O|} + B \left[e^{-2\beta(|\underline{r}_i - \underline{r}_C| - r_e)} - 2\cos^2(\eta_i) e^{-\beta(|\underline{r}_i - \underline{r}_C| - r_e)} \right] \quad , \quad (3.4)$$

where $r_e = 1.9 \text{ \AA}$ (or $3.6 a_0$) is the equilibrium distance between carbon and the copper atom on which CO is adsorbed. The Morse potential part contains an orientation factor $\cos(\eta_i) = \frac{(\underline{r}_C - \underline{r}_i)(\underline{r}_C - \underline{r}_O)}{|\underline{r}_C - \underline{r}_i||\underline{r}_C - \underline{r}_O|}$ in the attractive part, guaranteeing full attraction when the CO molecule's axis points directly at the copper atom Cu_i , as η_i is the angle between the C–O and C– Cu_i bonds. The interaction of the adsorbate atoms with each other is an unmodified Morse potential

$$V_{CO}(|\underline{r}_C - \underline{r}_O|) = F \left[e^{-2\gamma(|\underline{r}_C - \underline{r}_O| - r_0)} - 2e^{-\gamma(|\underline{r}_C - \underline{r}_O| - r_0)} \right] \quad , \quad (3.5)$$

with $r_0 = 1.125 \text{ \AA}$ (or $2.126 a_0$) being the equilibrium C–O bond length. The two equilibrium bond lengths as well as the other parameters are given in Table 3.1.

In the 2D and 3D cases considered here, the coordinates (X), Y , θ and ϕ , are held fixed in equilibrium positions, *i. e.* at 0. A 108 copper atom slab (formed by three layers of 6×6 atoms) serves to calculate the potential energy surfaces $V(r, Z)$ and $V(r, Z, X)$ from Eqs. (3.3), (3.4) and (3.5).

Two dimensions

A plot of the two-dimensional potential energy surface $V(r, Z)$ is shown in Fig. 3.2; displaying the narrow well in direction of the CO stretch mode r and the “flat” ascend of the potential

parameter	value
A	$32.1 E_h$
α	$1.78 a_0^{-1}$
B	$0.0213 E_h$
β	$1.59 a_0^{-1}$
F	$0.408 E_h$
γ	$1.22 a_0^{-1}$

Table 3.1: Parameters of Eqs. (3.4) and (3.5), taken from Refs. [36, 37].

in direction of the desorptive CO-adsorbate stretch mode Z , with the desorption limit around $Z = 8 a_0$ and the total desorption energy (including zero point energy) being $0.021 E_h$ ($\sim 4600 \text{ cm}^{-1}$)¹. The equilibrium distance² r_0^{2D} between C and O atoms is $2.13 a_0$ and the equilibrium distance between the carbon monoxides center of mass and the binding copper atom is $Z_0^{2D} = 4.81 a_0$.

The eigenenergies E_{n_r, n_Z} and eigenfunctions $|\phi_{n_r, n_Z}(r, Z)\rangle$ are calculated from Eq. (2.2) which is solved using the sinc-function discrete variable representation [98] summarized in Sec. A.1 and the following Hamiltonian

$$\hat{H}_0 = -\frac{\hbar^2}{2\mu} \frac{\partial^2}{\partial r^2} - \frac{\hbar^2}{2m} \frac{\partial^2}{\partial Z^2} + V(r, Z) \quad . \quad (3.6)$$

The grid used in the calculation consists of 40 points in r direction and 400 points in Z , with the grid in r encompassing the interval $[1.63, 2.63] a_0$ and in Z $[4.0, 9.0] a_0$. This choice is well suited to resolve the bound states as well as the (unbound) pre-dissociative states.

The energies of the lowest 21 eigenstates are given in Table 3.2 together with the quantum numbers (n_r, n_Z) . The zero point energy is 1237 cm^{-1} and the energy difference between the ground state $|0, 0\rangle$ and the desorption limit is 3174 cm^{-1} , their sum being 4411 cm^{-1} . A selection of the calculated eigenstates $|\phi_{n_r, n_Z}\rangle$ is given in Fig. (B.1) in Appendix B. The most interesting feature there being that also states slightly above the desorption limit,

¹Note, that the assignment of the unit $[\text{cm}^{-1}]$ to energies E or frequencies ω used here and in the following is rather “sloppy”.

²The equilibrium distances vary slightly from those of the potential surface. This is due to spacing of the grid on which the stationary problem is solved. These “equilibrium” distances, however, are only used to numerically evaluate $\mu_{mn} = \langle n | \mu_z | m \rangle$.

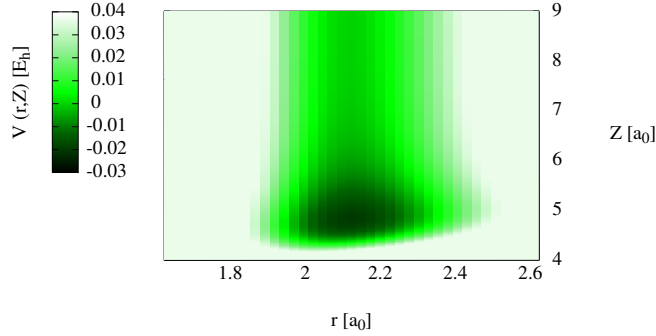


Figure 3.2: 2D potential energy surface $V(r, Z)$ as obtained from Eqs. (3.3), (3.4) and (3.5) by fixing the X , Y , θ and ϕ degrees of freedom, see Fig. 3.1 (a), to their equilibrium value.

i. e. ($E_{n_r, n_Z} > 0$), are still localized (unlike typical “vacuum states”) and well-resolved; these are so-called pre-dissociative states.

The fundamental frequencies $\omega_Z = \omega_{(0,1)(0,0)} = \frac{E_{0,1} - E_{0,0}}{\hbar}$ and $\omega_r = \omega_{(1,0)(0,0)}$ in Z and r being 294 and 2153 cm^{-1} , respectively, agree well with experiment [39] and the 6D calculations of Cattarius and Meyer [44] carried out within the framework of the multi-configurational time-dependent Hartree (MCTDH) approach [99]. A complete comparison of the energies of the present 2D (r, Z) and 3D (r, Z, X) results, known experimental values and the 6D results of Ref. [44] is given in Table 3.3 in Sec. 3.1.1. Further, they likewise compare well with higher-dimensional calculations recently carried out in our group [97], compare also Table 3.4 below. The lower “pure” modes in Z , that is $|0, 1\rangle$, $|0, 2\rangle$, $|0, 3\rangle$ and so on, feature a rather strong harmonicity with $\omega_{(0,2)(0,1)} - \omega_{(0,1)(0,0)} = -11 \text{ cm}^{-1}$. This allows one, at least for low energetic excitations, to use the harmonic rate model of Eq. (2.28) in Sec. 2.3.2. But in order to simulate a desorption by “ladder climbing” in the Z mode up to and above the unbound state $|0, 15\rangle$ anharmonic rates – retrieved from Eq. (2.31) and approximating ω_Z in Eq. (2.31) as $\omega_{(0,1)(0,0)}$.

state	$ n_r, n_z\rangle$	$(E_{n_r, n_z} - E_{0,0})$ [cm ⁻¹]
0	$ 0, 0\rangle$	0
1	$ 0, 1\rangle$	294
2	$ 0, 2\rangle$	577
3	$ 0, 3\rangle$	851
4	$ 0, 4\rangle$	1113
5	$ 0, 5\rangle$	1365
6	$ 0, 6\rangle$	1607
7	$ 0, 7\rangle$	1838
8	$ 0, 8\rangle$	2059
9	$ 1, 0\rangle$	2153
10	$ 0, 9\rangle$	2269
11	$ 1, 1\rangle$	2445
12	$ 0, 10\rangle$	2469
13	$ 0, 11\rangle$	2658
14	$ 1, 2\rangle$	2728
15	$ 0, 12\rangle$	2836
16	$ 1, 3\rangle$	3000
17	$ 0, 13\rangle$	3004
18	$ 0, 14\rangle$	3162
19	$ 1, 4\rangle$	3262
20	$ 0, 15\rangle$	3308

Table 3.2: The 21 lowest eigenenergies of the 2D model of CO/Cu(100) relative to the ground state $|0, 0\rangle$ which has a zero point energy of 1237 cm⁻¹ and lies 3174 cm⁻¹ beneath the desorption limit at 4411 cm⁻¹. States $|1, 4\rangle$ and $|0, 15\rangle$ are the first two states lying above latter for the presently used finite grid.

Three dimensions

The three-dimensional model, including as further degree of freedom one of the lateral modes, X , is treated in an analogous manner as the 2D model. Shown in Fig. B.2 in Appendix B are 2D cuts through the potential surface $V(r, Z, X)$, where $X = 0 a_0$ in (a), $Z = Z_0^{3D} = 4.81 a_0$ in (b) and $r = r_0^{3D} = 2.12 a_0$ in (c). In both (b) and (c) one can see the mirror symmetry of the potential with respect to the ($X = 0$) axis.

The 3D Hamiltonian reads

$$\hat{H}_0 = -\frac{\hbar^2}{2\mu} \frac{\partial^2}{\partial r^2} - \frac{\hbar^2}{2m} \frac{\partial^2}{\partial Z^2} - \frac{\hbar^2}{2m} \frac{\partial^2}{\partial X^2} + V(r, Z, X) \quad . \quad (3.7)$$

The grid on which the time-independent Schrödinger equation (2.2) is solved within the sinc-function DVR scheme, consists of 18 points in r , 33 points in Z and 55 points in the X coordinate, that is 32670 points in total. The coordinate ranges are $[1.8, 2.5] a_0$ for r , $[4.1, 6.0] a_0$ for Z and $[-2.75, 2.75] a_0$ for the X degree of freedom. Table 3.3 lists selected eigenenergies for the calculated states $|n_r, n_Z, n_X\rangle$ (see Fig. B.3 in Appendix B for exemplary 2D cuts). These are compared with the corresponding values of the 2D model, the values found in experiment [39] and those Cattarius and Meyer [44] calculated for six dimensions via MCTDH. In Ref. [44] also the Tully potential was used, though with a smaller copper slab ($3 \times 3 \times 2$) and utilizing for the actual frequency analysis a potential approximated in product form by the so-called POTFIT routine included in the the MCTDH programme package [100]. Frequencies for r and Z modes vary scarcely when compared to the 2D model, and thus agree well with experiment. The agreement with the 6D result of Ref. [44] is good. With a fundamental frequency of 77 cm^{-1} the lateral X mode compares reasonably well with the value of Ref. [44], but not with the experimentally [39] found value of 32 cm^{-1} . For alternative 6D calculations see Refs. [40, 43].

For the wavefunctions having nodes in the X coordinate and lying above state $|1, 0, 0\rangle$ it is no longer possible to assign quantum numbers, and thus it is also impossible to calculate individual transition rates according to Eq. (2.28) or Eq. (2.31). Further, optimal control calculations with the global algorithm described in Sec. (2.4.2) become difficult due to memory needs during forward / backward propagation. The “full” 3D system used in the calculations is chosen up to a cut-off energy of 2152 cm^{-1} above the ground state (155 states including the ground state), being suitable for the low energetic excitations studied here mainly. Further, for global optimal control calculations a reasonable selection of a subset of states is made

state	$ n_r, n_Z, n_X\rangle$	$(E_{n_r, n_Z, n_X} - E_{0,0,0})$ [cm ⁻¹]	2D model [cm ⁻¹]	exp. [39] [cm ⁻¹]	6D calc. [44] [cm ⁻¹]
0	$ 0, 0, 0\rangle$	0			
1	$ 0, 0, 1\rangle$	77		32	70.9
2	$ 0, 0, 2\rangle$	153			167.6
3	$ 0, 0, 3\rangle$	228			199.4
4	$ 0, 1, 0\rangle$	293	294	287	294.0
8	$ 0, 1, 2\rangle$	442			
12	$ 0, 2, 0\rangle$	576	577.4		577.5
154	$ 1, 0, 0\rangle$	2152	2153	2079	2152.6
870	$ 2, 0, 0\rangle$	4279	4279		

Table 3.3: Selected eigenenergies as obtained for the 3D model of CO/Cu(100) relative to the ground state $|0, 0, 0\rangle$ which has a zero point energy of 1273 cm⁻¹ (2D: 1237 cm⁻¹) and lies 3136 cm⁻¹ (2D: 3174 cm⁻¹) beneath the desorption limit. Given for comparison are also the values of the 2D model, experimental values [39] and the 6D calculations of Cattarius and Meyer [44], where the same potential and “rigid surface” model had been used.

in accordance to memory and aim of the particular IR excitation to be simulated. The second excited state in r $|2, 0, 0\rangle$, although lying more than 1000 cm⁻¹ above the desorption limit, is well resolved within the chosen grid boundaries, and so is suitable to study hot-band excitation $|0, 0, 0\rangle \rightarrow |1, 0, 0\rangle \rightarrow |2, 0, 0\rangle$, as shown in Appendix H and Sec. 4.1.3. Again, $|2, 0, 0\rangle$ is a “pre-desorptive” state.

Four and six dimensions

Recently, also in our group, the full six-dimensional eigenproblem and the 4D (r, Z, θ, ϕ) model was solved, using the potential $V(r, Z, X, Y, \theta, \phi)$ of Tully *et al.* [36, 37] with a 108 copper cluster [97]. In contrast to the above discussed model, the binding Cu atom was now positioned 0.352 Å (or 0.665 a₀) below the first surface layer as suggested in Refs. [40, 43] in order to minimize the energy. The equilibrium distances of the adsorbate on the “reconstructed” surface are $r'_0 = 1.126$ Å and $Z'_0 = 2.2$ Å. The eigenproblem was solved by an iterative two-term Lanczos eigensolver, see Appendix A.3. Table 3.4 displays the

	3D	4D	6D
ω_r [cm^{-1}]	2153	2150	2150
ω_Z [cm^{-1}]	294	347	345
$\omega_{X/Y}$ [cm^{-1}]	77		26.9
$\omega_{\theta/\phi}$ [cm^{-1}]		329	335
E_{ZPE} [cm^{-1}]	1273	1645	1638
D [cm^{-1}]	3136	3100	3108

Table 3.4: Fundamental frequencies ω_q for modes q , zero-point energies E_{ZPE} and desorption energies D with respect to the groundstate for the 3D model of Sec. 3.1.1 and the 4D and 6D models considered in Ref. [97].

fundamental frequencies ω_r , ω_Z , $\omega_{X/Y}$ (degenerate modes) and $\omega_{\theta/\phi}$, the zero-point energies (E_{ZPE}), desorption energies (D , zero-point energy subtracted) of the 4D and 6D models of Ref. [97]. The respective values of the 3D model of Sec. 3.1.1, where the “unreconstructed” Cu surface was employed, are shown for comparison.

The main difference here between unreconstructed (3D) and reconstructed (6D) models is the resonance frequency in X/Y (“frustrated translation”) for the reconstructed case. The frequencies found for the “frustrated rotation” (θ/ϕ) agree very well with the 287 cm^{-1} [39] from experiment.

3.1.2 Dipole function

Two- and three-dimensional models

For IR-excitation, the dipole function along the various degrees of freedom is needed. In the two-dimensional (r, Z) model, the dipole function $\mu_z(r, Z)$ (μ_z is the z -component of the

dipole function) used to simulate the field-dipole interaction has the following form

$$\begin{aligned}
 \mu_z(r, Z) &= \mu_z(r_0, Z_0) + \left(\frac{\partial \mu_z}{\partial r} \right)_{r=r_0} (r - r_0) \\
 &\quad + \left(\frac{\partial \mu_z}{\partial Z} \right)_{Z=Z_0} (Z - Z_0) + \left(\frac{\partial^2 \mu_z}{\partial Z^2} \right)_{Z=Z_0} (Z - Z_0)^2 \\
 &= \mu_0 + A(r - r_0) + B(Z - Z_0) + C(Z - Z_0)^2 \quad .
 \end{aligned} \tag{3.8}$$

This is a Taylor expansion around $r = r_0^{2D/3D}$ and $Z = Z_0^{2D/3D}$, respectively, truncated after the first term in r (linear term only) and the second term in Z (linear and quadratic terms), with the parameters $\mu_0 = -0.408 e a_0$, $A = -2.25 e$, $B = 0.566 e$ and $C = -0.361 e/a_0$. The parameters were derived from *ab initio* calculations [101, 102], according to which the factor A is enhanced, relative to free CO, by a factor of 2.18 [101].

Comparable derivative factors for the lateral modes X and Y are not available from literature, and attempts to find them by cluster calculations proved difficult. It is expected, however, that the variation of μ with X is weak; the dependence of μ on X was thus neglected in the following, making the X mode a “dark” mode.

Table 3.5 shows the absolute values of selected dipole transition moments $|\mu_{nm}|$ between states $|n\rangle = |n_r, n_Z, n_X\rangle$ and $|m\rangle = |m_r, m_Z, m_X\rangle$ as obtained from Eq. (3.8) for the 3D and 2D systems. Due to the lacking X -dependence of the dipole function transitions $|n\rangle \rightarrow |m\rangle$ where $(m_X = n_X \pm 1)$ are forbidden. But the even symmetry of the X mode (see the wavefunctions in Fig. B.3 in Appendix B), causes overtone transitions to be “weakly allowed” which obey the selection rules $(m_X = n_X \pm 2, n_X \pm 4, \dots)$. Transitions in Z are of a “medium” IR activity, with dipole transition moments in the order of magnitude of $10^{-2} e a_0$ for transitions of type $(m_Z = n_Z \pm 1)$. Overtone transitions $(m_Z = n_Z \pm 2, n_Z \pm 3, \dots)$ are weakly allowed and their dipole transition moments increase steadily with n_Z , just like those for the one-photon processes, until they reach a maximum, compare Fig. F.3 (a) in Appendix F. The CO stretch mode, finally, is strongly IR active, the overtone for $(n_r = 0)$ to $(m_r = 2)$ being still of some activity.

The dipole moments in both r and Z mode are further almost identical for the 2D and 3D models; those for Z transitions being slightly smaller in 2D, due to the larger grid used in this case and the “broader” quality of states having nodes in Z direction. And the matrix elements for the fundamental transitions in both modes take on the values they are expected to have according to the double-harmonic approximation, *e. g.* $\frac{|\mu_{10}|}{|\mu_{12}|} \approx \frac{1}{\sqrt{2}}$.

mode	states		$ \mu_{nm}^{3D} $	$ \mu_{nm}^{2D} $
	$ n\rangle$	$ m\rangle$	$[10^{-3} \text{ ea}_0]$	$[10^{-3} \text{ ea}_0]$
X	$ 0, 0, 0\rangle$	$ 0, 0, 1\rangle$	0.	
	$ 0, 0, 0\rangle$	$ 0, 0, 2\rangle$	1.9	
	$ 0, 0, 1\rangle$	$ 0, 0, 2\rangle$	0.	
	$ 0, 0, 1\rangle$	$ 0, 0, 3\rangle$	3.4	
	$ 0, 0, 0\rangle$	$ 0, 0, 4\rangle$	0.0053	
Z	$ 0, 0(, 0)\rangle$	$ 0, 1(, 0)\rangle$	38	36
	$ 0, 0(, 0)\rangle$	$ 0, 2(, 0)\rangle$	4.8	4.7
	$ 0, 1(, 0)\rangle$	$ 0, 2(, 0)\rangle$	53	50
	$ 0, 2(, 0)\rangle$	$ 0, 3(, 0)\rangle$	63	60
	$ 0, 7(, 0)\rangle$	$ 0, 8(, 0)\rangle$	83	79
r	$ 0, 0(, 0)\rangle$	$ 1, 0(, 0)\rangle$	140	140
	$ 0, 0(, 0)\rangle$	$ 2, 0(, 0)\rangle$	7.4	7.4
	$ 1, 0(, 0)\rangle$	$ 2, 0(, 0)\rangle$	200	200

Table 3.5: Selected absolute values of dipole transition moments $|\mu_{nm}|$ for CO/Cu(100), retrieved from calculating $\langle n_r, n_Z, n_X | \mu_z | m_r, m_Z, m_X \rangle$ and $\langle n_r, n_Z | \mu_z | m_r, m_Z \rangle$ for the 3D and 2D models, respectively, with the quantum number notation being $|n\rangle = |n_r, n_Z(, n_X)\rangle$ and $|m\rangle = |m_r, m_Z(, m_X)\rangle$.

Asymptotically corrected and higher-dimensional dipole functions

The above form of the dipole function (3.8), originally used in the present work and also by Cattarius and Meyer [44], has the wrong asymptotic behaviour for ($Z \rightarrow \infty$). Due to the quadratic term in Z , $\mu_z(r, Z)$ grows dramatically, whereas a physically correct function should approach the dipole moment of free carbon monoxide being 0.0441 ea_0 . Thus, when aiming for example at a simulation of desorption via “ladder climbing” in Z , Eq. (3.8) is expected to overestimate transition dipole moments for higher quantum numbers n_Z .

A functional form which would guarantee $\mu(r_0, Z) \rightarrow 0$ for ($Z \rightarrow \infty$), implying the approximation $\mu_z(CO_{free}) \approx 0$, is

$$\mu_z(r, Z) = a(r - r_0) + [\mu_0 - b(Z - Z_0)] e^{-\frac{Z-Z_0}{c}} \quad . \quad (3.9)$$

Fitting the results of quantum chemistry (B3LYP/LANL2DZ) calculations on a suited cluster model CO@Cu₃₄ of CO/Cu(100) – see Appendix F for details – the following parameters are obtained: $a = -1.810 \text{ ea}_0$, $b = -0.510 \text{ e}$ and $c = 1.808 \text{ a}_0$. Since the parameters a and A for the linear term of the dipole moment agree rather well, the choice of cluster and method appears to be justified. The dipole function of Eq. (3.9) is used in Sec. 4.1.2.

For the four-dimensional model with coordinates (r, Z, θ, ϕ) in Ref. [97] the following expression

$$\mu_z(r, Z, \theta, \phi) = \left[\mu_1 + A'(r - r_0) + B'e^{-C'(Z-Z_0)} \right] f(\theta, \phi) \quad (3.10)$$

was fitted to data obtained from the CO@Cu₃₄ cluster. The resulting parameters are $\mu_1 = 0.0357 \text{ ea}_0$, $A' = -2.25$, $B' = -0.4437 \text{ ea}_0$ and $C' = 1.2756 \text{ a}_0$. The angular function was chosen as

$$f(\theta, \phi) = \cos(\theta) + \sin^2(\theta) [d_1 + d_2 \cos(4\phi)] \quad , \quad (3.11)$$

respecting the four-fold symmetry in ϕ . From the fitted parameters $d_1 = 1.1558$ and $d_2 = -0.0004$ one sees that the θ dependence of $\mu_z(r, Z, \theta, \phi)$ dominates strongly over the ϕ dependence. The dipole transition moment μ_{nm} for the fundamental transitions are $3.3 \cdot 10^{-3} \text{ ea}_0$ for $|n\rangle = |n_r = 0, n_Z = 0, n_\theta = 0, n_\phi = 0\rangle \rightarrow |m\rangle = |0, 0, 1, 0\rangle$ and $1.4 \cdot 10^{-12} \text{ ea}_0$ for $|n\rangle = |0, 0, 0, 0\rangle \rightarrow |m\rangle = |0, 0, 0, 1\rangle$, respectively. The dipole function (3.10) was used in Sec. 4.1.4 below.

3.1.3 Dissipation and dephasing rates

Rates for the two- and three-dimensional models

For the present calculations on CO/Cu(100), the lifetimes as calculated in Refs. [36, 37] were used. For ($T = 0 \text{ K}$) a pure electronic decay mechanism (Sec. 2.3.1) and for ($T = 10, 300 \text{ K}$) an additional phononic decay channel was considered. The according rates $\Gamma_{m \rightarrow n}$ for the fundamental transitions in each mode are given in Table 3.6 for the three-dimensional model, *i. e.* $|m\rangle = |m_r, m_Z, m_X\rangle$ and $|n\rangle = |n_r, n_Z, n_X\rangle$. Those for the r and Z modes in the 2D model are analogous, only then $|m\rangle = |m_r, m_Z\rangle$ and $|n\rangle = |n_r, n_Z\rangle$ and the equations (2.28) and (2.31) to obtain the other rates in harmonic and anharmonic consideration, respectively, contain two instead of three terms in sum and product. The “upward” rates $\Gamma_{m \rightarrow n}$ for

mode	transition		$\Gamma_{m \rightarrow n}(0 \text{ K})$	$\Gamma_{m \rightarrow n}(10 \text{ K})$	$\Gamma_{m \rightarrow n}(300 \text{ K})$	
	$ m\rangle$	\rightarrow	$ n\rangle$	$[\text{ps}^{-1}]$	$[\text{ps}^{-1}]$	
r	$ 1, 0, 0\rangle$	\rightarrow	$ 0, 0, 0\rangle$	$\frac{1}{3.3}$	$\frac{1}{1.7}$	$\frac{1}{1.6}$
	$ 0, 0, 0\rangle$	\rightarrow	$ 1, 0, 0\rangle$	0	≈ 0	$\frac{1}{48\,700}$
Z	$ 0, 1, 0\rangle$	\rightarrow	$ 0, 0, 0\rangle$	$\frac{1}{82.0}$	$\frac{1}{22.0}$	$\frac{1}{2.8}$
	$ 0, 0, 0\rangle$	\rightarrow	$ 0, 1, 0\rangle$	0	≈ 0	$\frac{1}{11.4}$
X	$ 0, 0, 1\rangle$	\rightarrow	$ 0, 0, 0\rangle$	$\frac{1}{108}$	$\frac{1}{14.0}$	$\frac{1}{2.3}$
	$ 0, 0, 0\rangle$	\rightarrow	$ 0, 0, 1\rangle$	0	$\frac{1}{85\,300}$	$\frac{1}{3.3}$

Table 3.6: Rates $\Gamma_{m \rightarrow n}$ for the fundamental transitions in r , X and Z modes for temperatures of 0, 10 and 300 K as taken from Ref. [37] ($E_n < E_m$; “downward” rates), and obtained from detailed balance ($E_n > E_m$; “upward” rates), see Eq. (2.34).

($E_n > E_m$), being non-zero for ($T > 0 \text{ K}$), are calculated from detailed balance (2.34).

When looking at the rates one sees that the CO stretch mode r decays within few ps, is temperature-insensitive and, due to the large vibrational quantum of 2152 cm^{-1} , the “upward” rate is very small even at 300 K. This is different for Z and X modes, which are long-lived, couple more strongly to the metal phonons and thus have a significant temperature dependence. For example, the lifetime of state $|0, 0, n_X = 1\rangle$ drops from well over 100 ps to a value around 2 ps when going from ($T = 0 \text{ K}$) to ($T = 300 \text{ K}$).

By choosing these particular three modes – r , Z and X – not only a broad spectrum of vibrational lifetimes is covered, but also quite varying IR activities (compare Table 3.5 in Sec. 3.1.2) enter the model, making this a suitable reference model of vibrational adsorbate excitation in many dimensions.

In addition to the two- and three-dimensional models, a “one-dimensional” model consisting of states $|0, 0, 0\rangle \equiv |0_r\rangle$, $|1, 0, 0\rangle \equiv |1_r\rangle$ and $|2, 0, 0\rangle \equiv |2_r\rangle$ is taken into account. Only for this 1D study of the CO stretch mode r , see Sec. 4.1.1, pure dephasing is considered, as a T_2 time of 1.6 ps is available based on estimation from experimental linewidth measurements [20, 73]. From there, pure dephasing rates ($\gamma_{mn}^* = \gamma_{nm}^*$) can be obtained from Eqs. (2.37) and (2.35) and the Gaussian pure dephasing model mentioned in Sec. (2.3.2). Table 3.7 lists relaxation rates $\Gamma_{m \rightarrow n}$, T_1 (inelastic scattering) and T_2^* (elastic scattering)

$ m\rangle$	$ n\rangle$	$\Gamma_{m\rightarrow n}$ [ps ⁻¹]	γ'_{mn} [ps ⁻¹]	γ^*_{mn} [ps ⁻¹]	γ_{mn} [ps ⁻¹]
$ 0_r\rangle$	$ 1_r\rangle$	0	$\frac{1}{6.6}$	$\frac{1}{2.1}$	$\frac{1}{1.6}$
$ 0_r\rangle$	$ 2_r\rangle$	0	0	$\frac{1}{8.4}$	$\frac{1}{8.4}$
$ 1_r\rangle$	$ 0_r\rangle$	$\frac{1}{3.3}$	$\frac{1}{6.6}$	$\frac{1}{2.1}$	$\frac{1}{1.6}$
$ 1_r\rangle$	$ 2_r\rangle$	0	$\frac{1}{3.3}$	$\frac{1}{2.1}$	$\frac{1}{1.3}$
$ 2_r\rangle$	$ 0_r\rangle$	0	0	$\frac{1}{8.4}$	$\frac{1}{8.4}$
$ 2_r\rangle$	$ 1_r\rangle$	$\frac{1}{1.7}$	$\frac{1}{3.3}$	$\frac{1}{2.1}$	$\frac{1}{1.3}$

Table 3.7: Relaxation rates $\Gamma_{m\rightarrow n}$, energy related dephasing rates γ'_{mn} , pure dephasing rates γ_{mn} and total dephasing rates γ_{mn} for the three-state model of the r mode of CO/Cu(100), where $|0, 0, 0\rangle \equiv |0_r\rangle$, $|1, 0, 0\rangle \equiv |1_r\rangle$ and $|2, 0, 0\rangle \equiv |2_r\rangle$.

dephasing rates, γ'_{mn} and γ^*_{mn} , as well as the total (T_2) dephasing rates $\gamma_{mn} = \gamma'_{mn} + \gamma^*_{mn}$ (see Eq. (2.18) for the three-state system at ($T = 0$ K)). For the calculations done within the 2D and 3D models only dephasing due to energy relaxation is taken into account, *i. e.* the last term of Eq. (2.18) is omitted.

Rates for the four-dimensional model

For the four-dimensional model, similarly to Sec. 2.3.1 Tremblay *et al.* [97] started, following Tully *et al.* [36, 37], with Fermi's Golden Rule expression for the transition rate. For the coupling operator the total 6D kinetic energy operator, see Eq. (3.1), has been used. When neglecting³ all cross terms one obtains a tractable 5-term polynomial, each term representing the dissipation mechanism along a particular mode. The first four terms can be evaluated similarly, say, for a generic stretching coordinate $q(= r, Z, X, Y)$. The corresponding matrix elements are proportional to $\langle v_f | \langle e_f | \frac{\partial^2}{\partial q^2} | e_i \rangle | v_i \rangle$. They can be simplified after application of the product rule by the observation that the electronic wavefunctions are orthogonal and by neglecting the term which contains second derivatives of the electronic wave functions with respect to nuclear coordinates. Furthermore the first-order coupling is represented as a

³In the following the procedure used in Ref. [97] is briefly outlined.

Taylor series truncated at the zeroth order. One thus gets [36, 37]

$$\langle v_f | \langle e_f | \frac{\partial^2}{\partial q^2} | e_i \rangle | v_i \rangle \simeq 2 \langle v_f | \frac{\partial v_i}{\partial q} \rangle \langle e_f | \frac{\partial e_i}{\partial q} \rangle \simeq d_{fi}^{(q)} \langle v_f | \frac{\partial v_i}{\partial q} \rangle \quad , \quad (3.12)$$

where $d_{fi}^{(q)}$ is the proportionality constant for the q^{th} degree of freedom. In analogy to the model discussed in Sec. 2.3.2 the initial state is considered to be harmonic along coordinate q resulting in the simple selection rule of $(\Delta v = -1)$. As in the case of Sec. 2.3.2 the transition rate grows linearly with the quantum number associated with the normal mode of interest, *i.e.* $\Gamma_{v_i \rightarrow v_f} = v_i \Gamma_{1 \rightarrow 0} \delta_{(v_i-1, v_f)}$. For the fundamental transition rates in modes r , Z and X/Y , the values as given in Table 3.6 for $(T = 0)$ K were used in Ref. [97].

The situation is more difficult for the angular modes, which are kinetically coupled. By observing that $\langle e_f | e_i \rangle = 0$, neglecting higher order derivatives of electronic states and evaluating the electronic integrals as zeroth-order Taylor expansions, one obtains a relatively simple expression for the angular dissipation mechanism

$$\langle v_f | \langle e_f | r^{-2} \hat{J}^2 | e_i \rangle | v_i \rangle \simeq -d_{fi}^{(\phi)} \langle v_f | \frac{1}{r^2 \sin^2(\theta)} \frac{\partial}{\partial \phi} | v_i \rangle - d_{fi}^{(\theta)} \langle v_f | \frac{1}{r^2} \left(\cot(\theta) + 2 \frac{\partial}{\partial \theta} \right) | v_i \rangle \quad . \quad (3.13)$$

This expression is somewhat more complicated than Eq. (3.12) and care must be taken deriving a selection rule for the transition rates between angular normal modes. Using point group symmetry it is known that integrals in Eq. (3.13) will vanish unless the product of their symmetry is totally symmetric. That is, in C_{4v} point group symmetry which is relevant for CO/Cu(100), we are looking for

$$S_{v_f} \otimes S_{oper} \otimes S_{v_i} \supset A_1 \quad , \quad (3.14)$$

where S_{v_f} (S_{v_i}) is the symmetry label of the v_f th (v_i th) state and S_{oper} is the symmetry label of the connecting operator. The symmetry of the derivative is the same as the coordinate, for instance A_1 for the θ motion and E for the ϕ motion. It appears that $\sin^2(\theta)$ and $\cot(\theta)$ have the symmetry of θ , A_1 . The coordinate r also transforms like A_1 . For odd numbers of quanta in the degenerate angular normal coordinate the states transform like E . For even numbers of quanta in the same normal coordinate three symmetry labels are accessible: A_1 for the θ -modes, B_1 and B_2 for the ϕ -modes. Focusing on one-quantum transitions one thus has to evaluate the symmetry of integrals from E states to $\{A_1, B_1, B_2\}$ states or the opposite. The terms in Eq. (3.13) then are

$$\begin{aligned} \langle v_f | \frac{1}{r^2 \sin^2(\theta)} \frac{\partial}{\partial \phi} | v_i \rangle &\equiv E \otimes E \otimes \{A_1, B_1, B_2\} \supset A_1 \\ \langle v_f | \frac{1}{r^2} \left(\cot(\theta) + 2 \frac{\partial}{\partial \theta} \right) | v_i \rangle &\equiv E \otimes A_1 \otimes \{A_1, B_1, B_2\} \equiv E \quad . \end{aligned} \quad (3.15)$$

For two-quanta transitions integrals from states with the same symmetry have to be evaluated, that is

$$\begin{aligned} \langle v_f | \frac{1}{r^2 \sin^2(\theta)} \frac{\partial}{\partial \phi} | v_i \rangle &\equiv E \otimes E \otimes E \equiv E \\ \langle v_f | \frac{1}{r^2} \left(\cot(\theta) + 2 \frac{\partial}{\partial \theta} \right) | v_i \rangle &\equiv \{A_1, B_1, B_2\} \otimes A_1 \otimes \{A_1, B_1, B_2\} \supset A_1 \end{aligned} \quad (3.16)$$

From Eq. (3.15) it can be seen that one-quantum transitions are allowed and that the coupling mechanism is along the ϕ degree of freedom. Eq. (3.16) reveals that two-quanta transitions are allowed and that the coupling mechanism is along the θ degree of freedom. There are therefore two coupling mechanisms involved in the relaxation of an excited degenerate state E.

$ n\rangle$	$ 0, 0, 0, 0\rangle$	$ 0, 0, 0, 1\rangle$	$ 0, 1, 0, 0\rangle$	$ 0, 0, 1, 0\rangle$	$ 0, 0, 0, 2\rangle$	$ 1, 0, 0, 0\rangle$
$ m\rangle$						
$ 0, 0, 0, 0\rangle$		$1.38 \cdot 10^{-9}$	42.2	3.27	$6.48 \cdot 10^{-11}$	145
$ 0, 0, 0, 1\rangle$	$\frac{1}{2.30}$		$3.88 \cdot 10^{-10}$	$1.39 \cdot 10^{-9}$	$9.61 \cdot 10^{-11}$	$1.92 \cdot 10^{-1}$
$ 0, 1, 0, 0\rangle$	$\frac{1}{82.0}$	0		4.30	$1.24 \cdot 10^{-10}$	11.7
$ 0, 0, 1, 0\rangle$	0	$\frac{1}{1.15}$	0		$1.60 \cdot 10^{-10}$	$9.91 \cdot 10^{-1}$
$ 0, 0, 0, 2\rangle$	0	$\frac{1}{1.15}$	0	0		$3.23 \cdot 10^{-14}$
$ 1, 0, 0, 0\rangle$	$\frac{1}{3.30}$	0	0	0	0	

Table 3.8: 4D model of CO/Cu(100): Selected absolute dipole transition moments $|\mu_{mn}|$ [10^{-3} ea_0] (upper right half) and vibrational relaxation rates $\Gamma_{m \rightarrow n}$ [ps^{-1}] (lower left half) for states $|m\rangle = |m_r, m_Z, m_\theta, m_\phi\rangle$, $|n\rangle = |n_r, n_Z, n_\theta, n_\phi\rangle$.

Table 3.8 lists rates $\Gamma_{(m_r, m_Z, m_\theta, m_\phi) \rightarrow (n_r, n_Z, n_\theta, n_\phi)}$ as well as absolute dipole transition moments $|\mu_{(m_r, m_Z, m_\theta, m_\phi)(n_r, n_Z, n_\theta, n_\phi)}|$ according to Eq. (3.10) for selected eigenstates $|m\rangle = |m_r, m_Z, m_\theta, m_\phi\rangle$, $|n\rangle = |n_r, n_Z, n_\theta, n_\phi\rangle$. The relaxation rate of the first excited state in ϕ is available [20, 36, 37], the according fundamental lifetime is $\tau_{vib} = 2.3 \text{ ps}$ at ($T = 0 \text{ K}$). This means that the (degenerate) state $|0, 0, 0, 1\rangle$ decays with a rate $(2.3 \text{ ps})^{-1}$ to the ground state $|0, 0, 0, 0\rangle$. Since the relaxation mechanism from the first excited state to the ground state is due to coupling via $\frac{\partial}{\partial \phi}$ it thus appears possible to extract one-quantum, $\frac{\partial}{\partial \phi}$ -mediated transition rates for every higher excited state. For example, the states which are doubly excited along the E mode, *i.e.* states $|0, 0, 1, 0\rangle$ (energetically degenerate) and $|0, 0, 0, 2\rangle$ (not energetically degenerate) decay, assuming a linear scaling of rates with initial angular quanta, with

twice the rate, $(1.15 \text{ ps})^{-1}$ to the first excited angular state $|0, 0, 0, 1\rangle$. Possible differences between the decay rates of states $|0, 0, 1, 0\rangle$ and $|0, 0, 0, 2\rangle$ are neglected here. Unfortunately there is no information on the two-quanta transitions mediated by $\frac{\partial}{\partial \theta}$. In Eq. (3.13) these contributions were neglected and the one-quantum transition in the relaxation rate expression was kept.

3.2 H/Si(100)

3.2.1 Potential energy surface and vibrational states

The system H/Si(100) was treated in collaboration with Guennadij Paramonov (National Academy of Sciences, Minsk, Belarus), and Ivan Andrianov (formerly Universität Potsdam) [104]. Two vibrational degrees of freedom are considered: r , the H–Si stretch mode and ϕ , the Si–Si–H bending motion as sketched in Fig. 3.3.

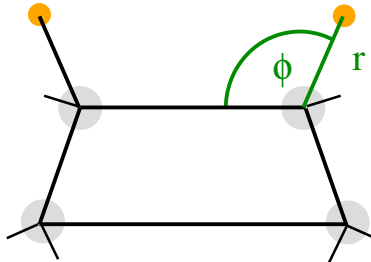


Figure 3.3: The two system coordinates used in the present model of H (orange) adsorbed on the Si(100)- 2×1 surface (Si atoms in grey): H–Si stretch mode r and Si–Si–H bending mode ϕ .

The potential energy function used for the calculation of lattice vibrations (see below) is the same as the as in the previous publication of Andrianov and Saalfrank [52], namely a semi-empirical bond-order potential [105–107] including three-body interactions. For the sub-system potential $V(r, \phi)$, a semi-empirical form was used instead with

$$V(r, \phi) = D \left(1 - e^{-\alpha(r-r_0)} \right)^2 + \frac{k}{2} e^{-\beta(r-r_0)^2} (\phi - \phi_0)^2 \quad , \quad (3.17)$$

with parameters $D = 3.4 \text{ eV}$ (or $0.125 E_h$, H binding energy), $\alpha = 0.83 a_0^{-1}$, $\beta = 0.2 a_0^{-2}$, $k = 3.951 \cdot 10^{-6} E_h / (1^\circ)^2$, and the equilibrium coordinates $r_0 = 2.84 a_0$ and $\phi_0 = 112.6^\circ$.

The system potential enters the system Hamiltonian $\hat{H}_S(r, \phi)$

$$\hat{H}_S(r, \phi) = -\frac{\hbar^2}{2m} \frac{\partial^2}{\partial r^2} - \frac{\hbar^2}{2mr^2} \frac{\partial^2}{\partial \phi^2} + V(r, \phi) \quad , \quad (3.18)$$

with m being the mass of the hydrogen atom⁴. Using Eqs. (3.18) and (2.2) as well as diagonalization utilizing the sinc-function DVR method [98] (see also Sec. A.1 in Appendix A), the 2D eigenstates (n_r, n_ϕ) and eigenenergies E_{n_r, n_ϕ} were calculated in Ref. [52]. The fundamental frequencies ω_r and ω_ϕ calculated in this way [52, 104] are 2037 cm^{-1} and 637 cm^{-1} , in good agreement with experiment [53], where 2100 cm^{-1} and 630 cm^{-1} were determined. The calculated zero point energy within the 2D model is 1370 cm^{-1} .

3.2.2 Dipole function

In order to estimate a dipole function $\mu_z(r, \phi)$ in Ref. [52] quantum chemical calculations (B3LYP/6-31G(d,p)) using GAUSSIAN 03 [108] were carried out. A cluster H_2Si_6 mimicking a fully covered Si_2 dimer within a 2×1 reconstructed Si(100) surface was chosen for this, where only r and ϕ for a single H atom were varied while all other atoms kept their fixed positions as obtained from the bond-order forcefield calculation for a cluster with 180 atoms [52]. The dipole moment was fitted to the form

$$\mu_z(r, \phi) = A_0 + A_1(r - r_0)e^{-A_2(r - r_0)} + A_3(\phi - \phi_0)^2 \quad , \quad (3.19)$$

with parameters $A_0 = 0.4001 \text{ ea}_0$, $A_1 = -1.2587 \text{ e}$, $A_2 = 0.3175 \text{ a}_0^{-1}$ and $A_3 = -0.4735 \text{ ea}_0/\text{rad}$ ($1 \text{ rad} = 57.3^\circ$).

Table 3.9 shows absolute dipole transition moments $|\mu_{(m_r, m_\phi)(n_r, n_\phi)}|$ (upper right half) and transition energies $\omega_{(m_r, m_\phi)(n_r, n_\phi)}$ (lower left half) between the lowest seven eigenstates. One can see that the ϕ mode is moderately IR active and very harmonic. Overtone transitions of type $(n_\phi = m_\phi \pm 2)$ are less IR active than $(n_\phi = m_\phi \pm 1)$ transitions but still possible. Further the H–Si stretch mode is strongly IR active and intermode coupling between the r and ϕ modes is weak, see for example the small dipole transition moment $|\mu_{(1,0)(0,4)}|$.

⁴A small additional potential-like term has been omitted in Eq. (3.18.) – see Ref. [109]

$ n_r, n_\phi\rangle$	$ 0, 0\rangle$	$ 0, 1\rangle$	$ 0, 2\rangle$	$ 0, 3\rangle$	$ 1, 0\rangle$	$ 0, 4\rangle$	$ 1, 1\rangle$
$ m_r, m_\phi\rangle$							
$ 0, 0\rangle$		51	8.5	0.16	210	0.076	1.5
$ 0, 1\rangle$	637		71	15	3.3	0.32	210
$ 0, 2\rangle$	1271	634		87	1.2	21	4.7
$ 0, 3\rangle$	1903	1266	632		0.046	100	2.1
$ 1, 0\rangle$	2037	1400	766	134		0.0052	50
$ 0, 4\rangle$	2532	1896	1261	629	495		0.093
$ 1, 1\rangle$	2661	2024	1390	758	624	129	

Table 3.9: 2D model of H/Si(100): Absolute dipole transition moments $|\mu_{(m_r, m_\phi)(n_r, n_\phi)}|$ [10^{-3} ea₀] (upper right half) and transition energies $\omega_{(m_r, m_\phi)(n_r, n_\phi)}$ [cm^{-1}] (lower left half) between the lowest seven eigenstates.

For high-energetic excitations in r also a 1D model with potential $V(r, \phi_0)$ is used, for which the necessary quantities for the density matrix dynamics are calculated by analogous methods (sinc-function DVR) as in the 2D case. In the 1D model, the Hamiltonian in Eq. (3.18) becomes $\hat{H}_S(r)$ with a single term and the dipole function $\mu_z(r)$, where the last term drops out as ($\phi = \phi_0$). The zero point energy obtained in 1D is 1056 cm^{-1} (2D: 1370 cm^{-1}); the fundamental frequency is 2050 cm^{-1} (2D: 2037 cm^{-1}) and the transition dipole moment $|\mu_{n_r=0, m_r=1}| = 0.21 \text{ ea}_0$, differing from the 2D model only minimal. Overtone transitions are of medium to weak IR activity, *e. g.* $|\mu_{n_r=0, m_r=2}| = 0.036 \text{ ea}_0 < |\mu_{n_r=0, m_r=3}| = 0.0080 \text{ ea}_0 < |\mu_{n_r=0, m_r=4}| = 0.0021 \text{ ea}_0$.

3.2.3 Dissipation and dephasing rates

Dissipation rates $\Gamma_{(m_r, m_\phi) \rightarrow (n_r, n_\phi)}$ were calculated in Ref. [52] via Fermi's Golden Rule (compare also Eq. (2.19)), expressed here for initial state $|i\rangle$ and final state $|f\rangle$ coupled by the system-bath Hamiltonian \hat{H}_{SB}

$$\Gamma_{i \rightarrow f} = \frac{2\pi}{\hbar} \left| \langle i | \hat{H}_{SB} | f \rangle \right|^2 \delta(E_f - E_i) \quad . \quad (3.20)$$

The total Hamiltonian \hat{H} used in Ref. [52] to calculate rates and other quantities of inter-

est from cluster models of H/Si(100) consists of system, bath and system-bath contributions

$$\hat{H} = \hat{H}_S + \hat{H}_{SF} + \hat{H}_{SB} + \hat{H}_B \quad , \quad (3.21)$$

where the Hamiltonian \hat{H}_S including two modes of the adsorbate (system) is given by Eq. (3.18). $\hat{H}_{SF} = -\hat{\mu}_z F_z(t)$ is the semi-classical system-field interaction term and \hat{H}_B describes the bath modes

$$\hat{H}_B = \sum_i \left(-\frac{\hbar^2}{2M_i} \frac{\partial^2}{\partial q_i^2} + \frac{1}{2} M_i \omega_i^2 q_i^2 \right) \quad (3.22)$$

whose frequencies, masses and coordinates are ω_i , M_i and q_i . These were calculated from the bond-order forcefield by normal-mode analysis from a cluster consisting of 180 atoms, giving 534 normal modes. See Ref. [52] for more details.

The coupling term \hat{H}_{SB} entering Eq. (3.20) for the rates, accounting for one- and two-photon relaxation, reads

$$\hat{H}_{SB} = \sum_i \lambda_i(r, \phi) q_i + \frac{1}{2} \sum_{ij} \Lambda_{ij}(r, \phi) q_i q_j \quad , \quad (3.23)$$

and is motivated by a Taylor expansion of the potential of second order around the equilibrium bath coordinates q_i^0 [110]. Thus the coupling functions were retrieved from derivatives of the total potential energy surface

$$\lambda_i(r, \phi) = \left(\frac{\partial V(\{x_k\})}{\partial q_i} \right)_{q_i^0} \quad (3.24)$$

$$\Lambda_{ij}(r, \phi) = \left(\frac{\partial^2 V(\{x_k\})}{\partial q_i \partial q_j} \right)_{q_i^0, q_j^0} \quad , \quad (3.25)$$

where $\{x_k\}$ are the Cartesian coordinates of the cluster atoms.

Eq. (3.20) was evaluated with initial and final states $|n\rangle = |\chi_n\rangle \cdot |\phi_n\rangle$, where $|\chi_n\rangle = \prod_{i=1}^N |\Psi_{i,n}(q_i)\rangle$ is a ‘‘phonon function’’ (with $|\Psi_{i,n}(q_i)\rangle$ being the n th eigenstate of the i th environment oscillator), and $|\phi_n\rangle = |\phi_n(r, Z)\rangle = |\phi_{n_r, n_z}(r, Z)\rangle$ denotes a 2D eigenfunction of \hat{H}_S . Further, \hat{H}_{SB} is given by Eq. (3.23). Finally, the δ -functions in (3.20) are represented by broadening Lorentzians with

$$\delta(x) \approx \frac{1}{\pi} \frac{\gamma}{x^2 + \gamma^2} \quad , \quad (3.26)$$

where γ was chosen as 8 cm^{-1} . For a bath temperature of 0 Kelvin, the rates $\Gamma_{(m_r, m_\phi) \rightarrow (n_r, n_\phi)}$, as listed in Table 3.10 for the lowest seven states, were obtained. Additionally given are the

$ n_r, n_\phi\rangle$	$ 0, 0\rangle$	$ 0, 1\rangle$	$ 0, 2\rangle$	$ 0, 3\rangle$	$ 1, 0\rangle$	$ 0, 4\rangle$	$ 1, 1\rangle$
$\tau_{ n_r, n_\phi\rangle}$		1.35	0.69	0.48	2130	0.37	1.45
$ m_r, m_\phi\rangle$							
$ 0, 0\rangle$							
$ 0, 1\rangle$	0.74						
$ 0, 2\rangle$	0.	1.4					
$ 0, 3\rangle$	0.	0.	2.1				
$ 1, 0\rangle$	0.	0.	$4.7 \cdot 10^{-4}$	$9.8 \cdot 10^{-8}$			
$ 0, 4\rangle$	0.	0.	0.	2.7	$4.7 \cdot 10^{-6}$		
$ 1, 1\rangle$	0.	0.	0.	$1.2 \cdot 10^{-3}$	0.69	$3.7 \cdot 10^{-7}$	

Table 3.10: H/Si(100): Lifetimes $\tau_{(n_r, n_\phi)}$ [ps] (first row) of the lowest seven eigenstates and vibrational relaxation rates $\Gamma_{(m_r, m_\phi) \rightarrow (n_r, n_\phi)}$ [ps^{-1}] between them for $T = 0\text{ K}$ as calculated in Ref. [52] from Eqs. (3.20), (3.22), (3.23) and (3.24).

lifetimes $\tau_{(n_r, n_\phi)}$ of these states resulting from a summation over all contributing transition rates as

$$\tau_{(n_r, n_\phi)}^{-1} = \sum_{p_r \neq n_r, p_\phi \neq n_\phi} -\Gamma_{(p_r, p_\phi) \rightarrow (n_r, n_\phi)} + \sum_{q_r \neq n_r, q_\phi \neq n_\phi} \Gamma_{(n_r, n_\phi) \rightarrow (q_r, q_\phi)} \quad (3.27)$$

The r mode is long-lived, in the range of nanoseconds and in good agreement with experiment [53]. Here, the main interest will be the ϕ mode. Latter is short-lived with lifetimes in the picosecond range and although these rates were calculated using explicitly the Golden Rule, the rates for the lowest three one-quantum decay processes fulfill the harmonic relation of Eq. (2.28) with the selection rule ($m_r = n_r + 1$) and a proportionality of rate and initial quantum number m_r . But already for state $|0, 4\rangle$ the decay rate with respect to $|0, 3\rangle$ is smaller than expected in the harmonic case and an additional inter-mode decay channel to state $|1, 0\rangle$, though with a small rate, is open. This inter-mode decay is the only possibility by which the long-lived r mode can decay, as a direct decay to the ground state is not possible, the according transition rates being zero.

Not only the lifetime but also their temperature dependence presented in Ref. [52] agree reasonably well with the experimental finding for the H–Si stretch mode r [53]. The much shorter lifetime for ϕ is a prediction and can be understood within the framework of a two-

phonon relaxation process [52].

In the following, only T_1 dephasing is considered here, taking only the first term on the right-hand side of Eq. (2.18) into account to retrieve the γ_{mn} .

3.3 2H/Ru(0001)

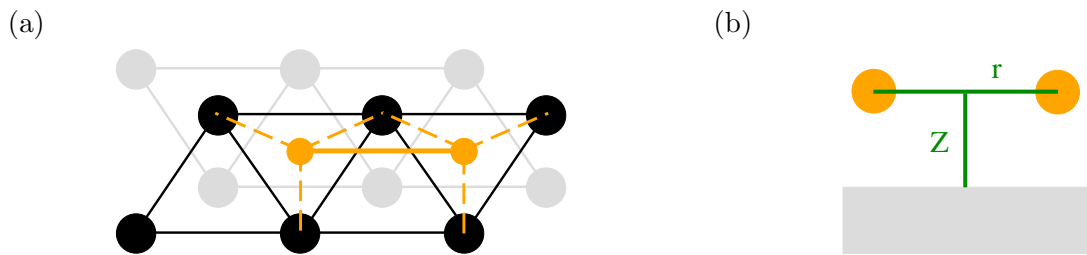


Figure 3.4: (a) On-top view of two H atoms (orange) adsorbed on the threefold hollow sites of Ru(0001); first metal layer depicted in black, second layer in grey. (b) Sideview schematically showing the H–H stretch mode r and the adsorbate-surface mode Z .

The vibrational model for the system 2H/Ru(0001) was developed in Ref. [111]. Like CO on copper the two hydrogen atoms adsorbed on ruthenium have six vibrational degrees of freedom, but in the present model a two-dimensional model is employed which is sketched in Fig. 3.4: The H atoms occupy neighbouring threefold hollow sites of the hcp (hexagonal closed-packed) metal (a), coordinate r describes the H–H stretch vibration and Z the motion of the “H₂”’s center of mass⁵ with respect to the binding position on level with the upper ruthenium layer (b).

3.3.1 Potential energy surface, stationary solution and dipole function

In Ref. [111], a 2D cut $V(r, Z)$ through the 6D potential surface of Luppi *et al.* [46, 47] was used. The latter was generated from periodic DFT calculations for a (2×2) coverage

⁵The H–H distance of $\sim 3 \text{ \AA}$ of the two ad-atoms is indicative of dissociative adsorption.

$ n_r, n_Z\rangle$	$ 0, 0\rangle$	$ 1, 0\rangle$	$ 0, 1\rangle$	$ 2, 0\rangle$	$ 1, 1\rangle$	$ 0, 2\rangle$	$ 3, 0\rangle$	$ 2, 1\rangle$	$ 1, 2\rangle$	$ 4, 0\rangle$
$ m_r, m_Z\rangle$										
$ 0, 0\rangle$		760	1095	1518	1823	2184	2272	2542	2884	3016
$ 1, 0\rangle$	6.9		335	758	1064	1424	1513	1782	2125	2256
$ 0, 1\rangle$	61	2.6		423	729	1089	1177	1447	1789	1921
$ 2, 0\rangle$	14	10	7.7		305	666	754	1023	1366	1498
$ 1, 1\rangle$	1.1	59	7.0	4.3		361	449	718	1061	1193
$ 0, 2\rangle$	3.1	0.34	86	0.98	4.1		88	357	700	832
$ 3, 0\rangle$	0.12	23	0.97	16	13	1.1		269	612	744
$ 2, 1\rangle$	0.089	2.7	14	56	10	11	6.7		343	475
$ 1, 2\rangle$	0.094	4.1	1.4	1.3	82	7.4	8.1	1.8		132
$ 4, 0\rangle$	0.16	0.022	0.47	32	8.6	0.94	24	18	4.8	

Table 3.11: 2D model of H₂/Ru(0001): Transition energies $\omega_{(n_r, n_Z)(m_r, m_Z)}$ [cm⁻¹] (upper right half) and absolute dipole momenta $|\mu_{(n_r, n_Z)(m_r, m_Z)}|$ [10^{-3} ea₀] (lower left half). See text for details.

of H on a three-layer relaxed slab model of Ru(0001) [47]. The 2D potential energy surface predicts the “H₂” to be bound with equilibrium distances of $r_0 = 2.75$ Å (or 5.20 ea₀) and $Z_0 = 1.06$ Å (2.00 ea₀); the binding energy is 0.85 eV, *i. e.* 0.425 eV per H atom. This is consistent with experiment [112] and earlier theoretical findings [113]. Of the two different gradient-corrected exchange-correlation potentials tested by Luppi *et al.*, the one arising from the RPBE (revised Perdew-Burke-Ernzerhof) functional [114] is employed.

The Hamiltonian is analogous to the one of Eq. (3.6) for the 2D CO/Cu(100) model and the time-independent Schrödinger equation (2.2) was solved in Ref. [111] by a Fourier Grid Hamiltonian diagonalization, see Sec. A.2. The zero point energy is 956 cm⁻¹. Table 3.11 gives the quantum numbers of the lowest ten states (n_r, n_Z) and in the upper right half the transition energies $\omega_{(n_r, n_Z)(m_r, m_Z)}$ between them. The fundamental frequencies ω_r and ω_Z are 760 and 1095 cm⁻¹, respectively, agreeing well with experiment [115], where 690 and 1130 cm⁻¹ was found. Both the r and Z modes are rather harmonic within the energy range of ca. 3000 cm⁻¹ above the ground state (0,0) covered in Table 3.11.

In order to determine a dipole function $\mu_z(r, Z)$, in Ref. [111] a H₂@Ru₁₂ cluster model

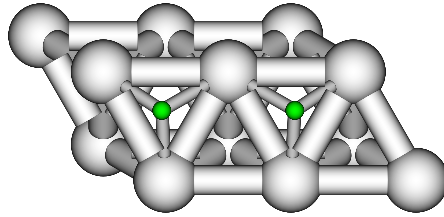


Figure 3.5: 2H@Ru₁₂ cluster used in Ref. [111] to calculate the data for $\mu_z(r, Z)$ of Eq. (3.28) employing B3LYP/LANL2DZ. The H–H distance (r_0) is 5.44 ea_0 (the potential of Luppi *et al.* [46, 47] predicts 5.20 ea_0) and the distance of the H–H axis to the first ruthenium layer (Z_0) is 2.01 ea_0 , both obtained by a previous geometry optimization. The lattice constant $d(\text{Ru–Ru}) = 5.11 \text{ ea}_0$ is held fixed.

was used as shown in Fig. 3.3.1. B3LYP [116] and the quasi-relativistic LANL2DZ [117] basis set and effective core potential (for Ru) were employed. The calculated data was fitted to the form

$$\mu_z(r, Z) = aZ^2 \tanh[b(r - c) + 1] \quad , \quad (3.28)$$

with parameters $a = -0.0473 \text{ ea}_0$, $b = 0.7 \text{ a}_0^{-1}$ and $c = 1.195 \text{ a}_0$ (as only z -polarised IR fields are employed only the z -component μ_z of the dipole moment is needed). As can be seen in the lower left half of Table 3.11 the r mode is only weakly dipole allowed (H_2 being an unpolar molecule), whereas Z is medium to strongly allowed. Inter-mode coupling is rather strong, with, for example $|\mu_{(1,0)(0,1)}| = 2.6 \cdot 10^{-3} \text{ ea}_0$ and $|\mu_{(2,1)(1,2)}| = 1.8 \cdot 10^{-3} \text{ ea}_0$ being of the same order of magnitude as the dipole moment of the fundamental transition in r ($2.6 \cdot 10^{-3} \text{ ea}_0$). Another interesting feature is, that overtone transitions in r are more strongly dipole active than single transitions, this is due to symmetry reasons as in case of the formally “forbidden” lateral X mode of CO/Cu(100).

3.3.2 Calculation of vibrational lifetimes

There is no theoretical data available for vibrational lifetimes of 2H on Ru(0001) as obtained, for example, from perturbation-theory calculations as in case of CO/Cu(100) [36, 37] and H/Si(100) [52]. Luntz *et al.* [48], however, used perturbation-theory in connection with a periodic DFT model in order to calculate two-dimensional (r, Z) electronic friction coefficients $\eta_{ij}(r, Z)$ ($i, j = r, Z$) from which one is able to estimate vibrational lifetimes for the two modes

as

$$\tau_{vib}^r \approx \frac{\mu_r}{\eta_{rr}(r_0, Z_0)} \approx 190 \text{ fs} \quad (3.29)$$

$$\tau_{vib}^Z \approx \frac{\mu_Z}{\eta_{ZZ}(r_0, Z_0)} \approx 500 \text{ fs} \quad , \quad (3.30)$$

where μ_r and μ_Z are the respective reduced masses. Estimations from experiment [21] similarly suggest lifetimes of some hundred femtoseconds for the vibrational modes. More explicitly, by fitting a one-dimensional, Arrhenius-type mode based on a truncated harmonic oscillator and electronic friction, Denzler *et al.* determined an effective vibrational lifetime of 180 fs along a “reaction coordinate” [21]. In the present work, the nonadiabatic MO theory of vibrational relaxation by Tully *et al.* [36,37] (see also Sec. 2.3.1) is used to gain more direct insight into lifetimes.

Cluster models for H₂/Ru(0001)

For this purpose both HF and B3LYP are chosen as methods. The basis (and effective core potential for the metal atoms) employed throughout is LANL2 [117], using LANL2 in double- ζ basis (LANL2DZ) for the H atoms and the five Ru atoms directly bonding it and in minimal basis (LANL2MB) for the other metal atoms.

In a first attempt the 2H@Ru₁₂ cluster (Fig. 3.3.1) was taken, but to study possible effects of cluster size and geometry a further cluster model 2H@Ru₁₃ containing one more ruthenium atom in the first layer is additionally taken into consideration. Given in Table 3.12 are the two cluster models and their respective HOMO (highest occupied MO) and LUMO (lowest unoccupied MO) energies ε_H and ε_L . For both cases the H coordinates with respect to the cluster as optimized for the 2H@Ru₁₂ cluster are used. The calculations were carried out by the programme package GAMESS [118] and a tight SCF energy convergence criterion of $10^{-10} E_h$.

Calculated vibrational lifetimes

Tully *et al.* suggest [36] several possibilities to choose the Fermi energy E_F at which the DOS $\underline{P}(E_F)$ is calculated according to Eq. (2.25), here we make the choice ($E_F = \varepsilon_H$), the energy of the highest occupied molecular orbital (see Table 3.12).

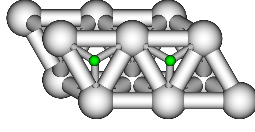
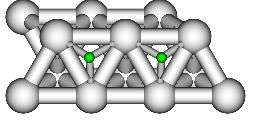
			
		2H@Ru ₁₂	2H@Ru ₁₃
HF	ε_H	-0.6309	-0.6246
	ε_L	-0.5041	-0.4837
B3LYP	ε_H	-0.6038	-0.5857
	ε_L	-0.5733	-0.5557

Table 3.12: Clusters used in the relaxation rate calculations for r and Z modes of $\text{H}_2/\text{Ru}(0001)$ according to Ref. [36] and their respective HOMO and LUMO energies [E_h] as obtained from HF/LANL2DZ(MB) and B3LYP/LANL2DZ(MB) calculations.

Further, different approaches for the calculation of the DOS matrices entering Eq. (2.26) have been made in Ref. [36], two of which are used here:

- In the first approach, we use two different matrices $\underline{\underline{P}}(E_F^-)$ and $\underline{\underline{P}}(E_F^+)$, a DOS below and above E_F , respectively. These are calculated by choosing a certain energy window, say 1 eV ($0.037 E_h$) as done here, and taking into account the HOMO and all orbitals lying 1 eV below it for $\underline{\underline{P}}(E_F^-)$ and likewise considering the HOMO and all orbitals lying 1 eV above it for the calculation of $\underline{\underline{P}}(E_F^+)$. Further, the δ -functions in Eq. (2.25) are approximated by rectangular functions, of uniform width

$$\Delta E = (\varepsilon_L - \varepsilon_H) + \frac{1}{2}(\varepsilon_H - \varepsilon_{H-1}) + \frac{1}{2}(\varepsilon_L - \varepsilon_{L+1}) \quad (3.31)$$

and height $\frac{1}{\Delta E}$, leading to

$$\underline{\underline{P}}(E_F^\mp) = \frac{2}{\Delta E} \sum_{p \in \text{occ./unocc.}} C_p C_p^\dagger \quad . \quad (3.32)$$

- In the second approach, we replace $\underline{\underline{P}}(E_F^-)$ and $\underline{\underline{P}}(E_F^+)$ in Eq. (2.26) by an averaged DOS

$$\underline{\underline{P}}(E_F^{\text{ave}}) = \frac{1}{2} (\underline{\underline{P}}(E_F^-) + \underline{\underline{P}}(E_F^+)) \quad ; \quad (3.33)$$

and thus

$$\underline{\underline{P}}(E_F^{\text{ave}}) = \frac{1}{\Delta E} \sum_p C_p C_p^\dagger \quad . \quad (3.34)$$

		2H@Ru ₁₂	2H@Ru ₁₃
HF	$\underline{\underline{P}}(E_F^\mp)$	0.133	0.136
	$\underline{\underline{P}}(E_F^{ave})$	0.254	0.239
B3LYP	$\underline{\underline{P}}(E_F^\mp)$	0.0721	0.108
	$\underline{\underline{P}}(E_F^{ave})$	0.124	0.110

Table 3.13: Vibrational lifetimes $\tau_{v=1 \rightarrow v=0}$ [ps] obtained for the H–H stretch mode r (T=0 K) from the two different clusters, quantum chemistry methods, and approximations for the density of states at the Fermi level ($E_F = \varepsilon_H$).

- An alternative Gaussian broadening model [103] was unsuccessful.

The derivatives of Fock and overlap matrix elements $F_{\mu\nu}$ and $S_{\mu\nu}$ with respect to the normal mode q (here: r and Z as shown in Fig. 3.4(b)) needed to calculate matrix \underline{W} in Eq.(2.26), are determined numerically for a small displacement χ_q from the equilibrium position

$$\frac{dM_{\mu\nu}}{dq} \approx \frac{M_{\mu\nu}(q_0 + \chi_q) - M_{\mu\nu}(q_0 - \chi_q)}{2\chi_q} \quad ; \quad (M_{\mu\nu} = F_{\mu\nu}, S_{\mu\nu}) \quad . \quad (3.35)$$

Thus only three quantum chemistry calculations are needed for the calculation of a single rate, one for the equilibrium position q_0 to obtain Fermi energy and DOS and two calculations for the matrix derivatives. The displacement χ_q was chosen to be reasonably [103] small as 0.001 Å (0.00189 a_0) for both modes.

Tables 3.13 and 3.14 list the obtained vibrational lifetimes of the first excited state in r (3.13) and Z (3.14) with respect to the vibrational groundstate. All lifetimes obtained are within a rather reasonable order of magnitude (ranging from roughly 100 fs to 1 ps) and the r mode relaxes in general faster than the Z mode, an observation also made in other estimates [48]. The following observations can be made: For the cases where the δ -functions occurring in the density of states are approximated as “double stepfunctions”, there is weak dependence of $\tau_{v=1 \rightarrow v=0}$ upon the used cluster model for the r mode and rather strong dependence in case of Z . This is understandable, as latter motion couples more strongly to the metal surface, so that the different MO energies, MO coefficients, Fock and overlap matrices are of more significance, particularly as only few cluster orbitals (~ 4 to 6) are taken into account. Another effect can be seen when comparing the results for the two methods,

		2H@Ru ₁₂	2H@Ru ₁₃
HF	$\underline{\underline{P}}(E_F^\mp)$	0.909	0.309
	$\underline{\underline{P}}(E_F^{ave})$	0.749	0.563
B3LYP	$\underline{\underline{P}}(E_F^\mp)$	0.272	0.671
	$\underline{\underline{P}}(E_F^{ave})$	0.380	0.601

Table 3.14: Vibrational lifetimes $\tau_{v=1 \rightarrow v=0}$ [ps] obtained for the H₂-surface stretch mode Z (T=0 K) from the two different clusters, quantum chemistry methods, and approximations for the density of states at the Fermi level ($E_F = \varepsilon_H$).

HF and B3LYP. The differences due to the usage of $\underline{\underline{P}}(E_F^\mp)$ or $\underline{\underline{P}}(E_F^{ave})$ are larger for HF where there is a larger energy spacing between HOMO and LUMO (and fewer orbitals within the energy window). In summary, the computed vibrational lifetimes $\tau_{v=1 \rightarrow v=0}$ estimated here are about 150 fs for the r mode and 560 fs for the Z mode, if an average is taken. The error bars are large, however, so that for the 2D dynamics calculations below a uniform rate

$$\Gamma_{(0,1) \rightarrow (0,0)} = \Gamma_{(1,0) \rightarrow (0,0)} = \frac{1}{500 \text{ fs}} \quad (3.36)$$

is chosen. For transitions $(m_r, m_Z) \rightarrow (n_r, n_Z)$ between states of higher quantum numbers the harmonic approximation (2.28) and detailed balance (2.34) are employed. As in case of H/Si(100), only T_1 dephasing is considered.

Chapter 4

Control of vibrational excitation in dissipative systems

The system CO/Cu(100) (Sec. 4.1) is treated in the present work, considering one- (4.1.1), two- (4.1.2), three- (4.1.3) and four-dimensional (4.1.4) models in order to study vibrational adsorbate excitation via simple \sin^2 -shaped control pulses as well as pulses obtained from optimal control theory. Various effects (“pure” dephasing, temperature, pulse duration) are examined and state-selective excitations in each vibrational mode are carried out. Special processes such as hot-band excitation, vibrational desorption via “ladder climbing” and “dark mode” excitation are simulated. Local control calculations on the non-dissipative 2D model which are presented in Appendix H for brevity do serve as pre-study for the global optimal control calculations below. The principle of local control further inspired a new “hybrid” algorithm presented in Chapter 5 which allows for time-dependent targets.

Further, calculations on the system H/Si(100) (Sec. 4.2) and H₂/Ru(0001) (Sec. 4.3) are presented, where the main aspects of interest are non-Markovian (“memory”) effects in vibrational decay and IR excitation and the mode-selective excitation of very harmonic and weakly dipole active modes.

4.1 CO/Cu(100) [96, 97]

4.1.1 One-dimensional model (r) [96]

Analogous to the local control calculations in Appendix H, 1D models for the C–O stretch mode r consisting of two and three states, respectively, are set up. The eigenenergies and dipole matrix elements are extracted from the 3D model in Sec. 3.1.

For the simple case of the two-state $|0\rangle \rightarrow |1\rangle$ population transfer induced by a \sin^2 -shaped pulse of duration t_f and frequency $\omega = \omega_{10} = \omega_r$ in resonance, the questions of interest are:

- What are the effects of the different kinds of relaxation processes, *e. g.* energy relaxation and dephasing?
- What are the effects of pulse length t_f , and the pulse fluence

$$f = \frac{1}{2}\epsilon_0 c \int_0^{t_f} F_0^2 \sin^4\left(\frac{\pi t}{t_f}\right) dt = \frac{3}{16}\epsilon_0 c F_0^2 t_f \quad ? \quad (4.1)$$

Accordingly, density matrix propagations at ($T = 0$ K) are carried out for $t_f = 4250$, 425 and 42.5 fs, covering the range of pico- and femtosecond scales typical for pulsed IR excitations. $P_1(t_f)$, the populations of state $|1\rangle$ at ($t = t_f$) are shown in Fig. 4.1 for the different dissipation scenarios (sketched in the left bottom corner), namely

- no dissipation at all (solid lines);
- energy relaxation and T_1 dephasing only (dashed lines);
- full dissipation including T_2^* dephasing (dotted lines).

The according energy and phase relaxation rates are given in Table 3.7. For the non-dissipative case, as expected, complete population inversion is accomplished for π pulses (more precisely $(2n+1)\pi$ pulses with $n = 0, 1, \dots$), *i. e.* at fluences of 3.5, 35 and 350 mJ/cm² for long, medium and short pulses. The oscillations observed here are the so-called Rabi oscillations, due to the absorption and re-emission of photons. In the dissipation-free case, both processes are complete (complete population and depopulation, respectively) if the frequency

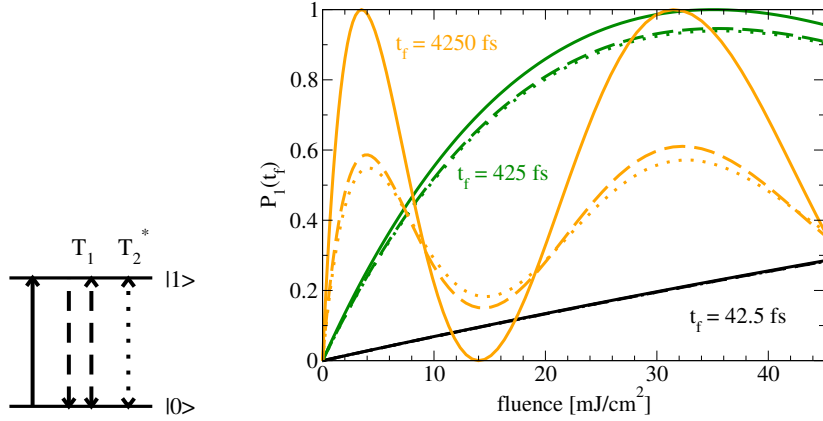


Figure 4.1: Population transfer from state $|0\rangle = |0_r\rangle$ to state $|1\rangle = |1_r\rangle$ in a two-state model of CO/Cu(100) by \sin^2 -shaped pulses of frequency $\omega_{10} = \omega_r$ for different pulse durations t_f and dissipation models at ($T = 0$ K): No dissipation (solid lines), energy relaxation and T_1 dephasing (dashed lines) and full dissipation with pure dephasing (dotted lines). The respective processes are schematically shown on the left: Excitation (solid arrow), energy relaxation (dashed arrow) and related T_1 dephasing (dashed double arrow) and pure, T_2^* dephasing (dotted double arrow). For dissipation and dephasing parameters see Table 3.7.

ω is resonant. Dissipation damps these oscillations, so that both absorption and stimulated emission processes are incomplete. As the vibrational lifetime of state $|1\rangle$ (3.3 ps), as well as the dephasing times are of the same order of magnitude as the duration of the longest pulse, dissipation has the biggest influence there and the maximal $P_1(t_f)$ is smaller than 0.6. In contrast, the dissipative loss is negligible in case of the 42.5 fs pulse. However, this pulse would afford rather high fluences. Thus, in dissipative systems, a compromise has to be made between dissipative loss and pulse fluence. Pure dephasing due to elastic scattering has a considerably smaller effect than inelastic scattering, the effect of the former being negligible already for the 425 fs pulse.

This medium pulse duration, as well as full dissipation, is chosen for the examination of hot-band excitation $|0\rangle \rightarrow |1\rangle \rightarrow |2\rangle$ in a three-state system. Fig. 4.2 compares the fluence dependence of the final population of state $|2\rangle$, $P_2(t_f)$, for

- \sin^2 -shaped pulses with $\omega = \omega_{10} = \omega_r$;
- OCT pulses obtained from the global control algorithm (Sec. 2.4.2) and taking as target

operator $\hat{O} = 0.42 |1\rangle\langle 1| + 0.58 |2\rangle\langle 2|$. The time-dependent shape-functions inspired by Ref. [88] are

$$\alpha(t) = \begin{cases} \alpha \cdot \sin^2\left(\frac{10\pi t}{2t_f}\right), & \text{if } t \leq \frac{t_f}{10} \\ \alpha & \text{if } \frac{t_f}{10} < t < t_f - \frac{t_f}{10} \\ \alpha \cdot \sin^2\left(\frac{10\pi t}{2t_f}\right) & \text{if } t \geq t_f - \frac{t_f}{10} \end{cases}, \quad (4.2)$$

enforcing $F_z(0) = F_z(t_f) = 0$.

At a given fluence, optimal pulses always yield higher target populations than the simple \sin^2 pulse. For small fluences the differences are minimal though, mainly due to the small anharmonicity in r (compare Table 3.3) with ($\omega_{10} \neq \omega_{21}$). The OCT pulses have a small downward “chirp” with respect to the carrier frequency $\omega \approx \omega_{10} = \omega_r = 2153 \text{ cm}^{-1}$ in this case, see Fig. 4.3 (a) where the Husimi transformation of the OCT pulse of fluence $f = 19 \text{ mJ/cm}^2$ is plotted. The \sin^2 pulse, however, can populate state $|2\rangle$ by 0.7 at most at $f \approx 50 \text{ mJ/cm}^2$. For higher fluences $P_2(t_f)$ decreases, due to stimulated emission setting in. In contrast, the OCT pulses are of advantage here, transferring up to 85 % of total population to the target state $|2\rangle$. Examining such a pulse ($f = 68 \text{ mJ/cm}^2$) more closely by Husimi transformation, see Fig. 4.2 (b), one sees that the “chirp” in this case is non-monotonic and intuitively not as easily to understand as the low-energetic pulse of (a). The main feature of pulse (b) is its off-resonance, particularly towards the end of the pulse, where an upward “chirp” is observable. By this, stimulated emission from the target state $|2\rangle$ back to the intermediate state $|1\rangle$ is suppressed. Plotted in Fig. 4.2 as inset is the ratio $\frac{P_2(t_f)}{P_1(t_f)}$ for both

t_f [fs]	106	213	425	850	1275	1700
$P_1(t_f)$	0.217	0.300	0.285	0.413	0.549	0.543
$P_2(t_f)$	0.037	0.121	0.305	0.403	0.228	0.087
$\frac{P_2(t_f)}{P_1(t_f)}$	0.171	0.403	1.070	0.975	0.415	0.160

Table 4.1: Three-level model of the r mode with states $|0\rangle$, $|1\rangle$, $|2\rangle$: Final populations and ratios of states $|1\rangle$ and $|2\rangle$ as obtained for \sin^2 -shaped pulses of fluence $f = 17 \text{ mJ/cm}^2$ for different pulse durations t_f at ($T = 0 \text{ K}$).

\sin^2 -shaped (dashed) and OCT pulses (solid with symbols) for fluences up to 25 mJ/cm^2 , as a measure for the “hot-band intensity”. As in Ref. [119], where Bonn *et al.* studied the C–O stretch hot-band excitation for CO/Ru(0001) within a three-state model similar to here, a

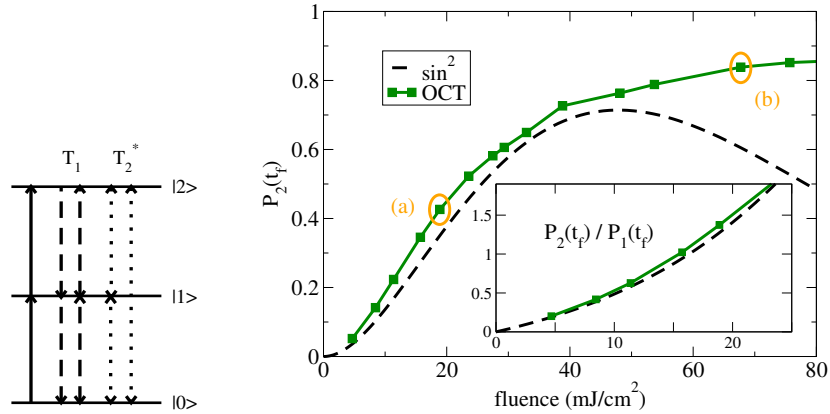


Figure 4.2: Hot-band excitation $|0\rangle \rightarrow |1\rangle \rightarrow |2\rangle$ at ($T = 0$ K) in a three-level model of CO/Cu(100): Populations of state $|2\rangle$ at $t = t_f$ as obtained for \sin^2 pulses of carrier frequency $\omega = \omega_{10} = \omega_r = 2153 \text{ cm}^{-1}$ (dashed) and global OCT pulses with $\hat{O} = 0.42 |1\rangle\langle 1| + 0.58 |2\rangle\langle 2|$ (solid line with symbols), as function of fluences. The inset depicts a measure for “hot-band intensity” $\frac{P_2(t_f)}{P_1(t_f)}$ [119] for smaller fluences. For the marked OCT pulses (a) and (b), Husimi plots are shown in Fig. 4.3 (a) and (b), respectively. The respective processes involved are schematically shown on the left: Excitation (solid arrow), energy relaxation (dashed arrow) and related T_1 dephasing (dashed double arrow) and pure, T_2^* dephasing (dotted double arrow). For dissipation and dephasing parameters see Table 3.7.

superlinear growth with f is found. In Ref. [119], too, a “chirped” pulse was suggested to enhance hot-band excitation. A further parameter which can be optimized is pulse length; so in the present case and for \sin^2 pulses and a fixed fluence of 17 mJ/cm^2 a pulse length of about 1 ps was found to be suited best to achieve a high absolute value for $P_2(t_f)$, whereas pulses of about half that duration deliver larger relative “hot-band intensities” $\frac{P_2(t_f)}{P_1(t_f)}$, see Table 4.1.

4.1.2 Two-dimensional model (r, Z)

Within the 2D system with modes r and Z (compare Sec. 3.1.1) IR induced desorption of CO from CO/Cu(100) can be studied. Hereby, population is excited to states above the desorption limit. The pre-dissociative character of the “continuum” states with r -excitation would lead to delayed desorption.

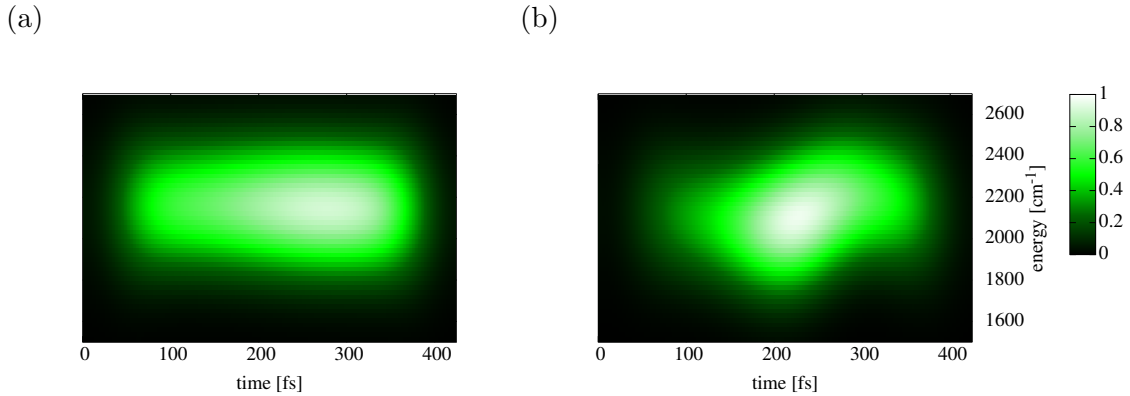


Figure 4.3: Husimi plots of OCT pulses (a) and (b) with fluences $f = 19$ and 68 mJ/cm^2 as marked in Fig. 4.2.

In the present model, all the population having reached the 21 states above the desorption limit at ($t = t_f$) will be considered as “desorbed”. Due to the fact that the “continuum” here is treated discretized, the energy relaxation rates of the respective states are chosen, alike those for the bound states, according to the anharmonic model of Eq. (2.31). Further, the asymptotically corrected dipole function of Eq. (3.9) is employed to ensure physically correct dipole interaction for larger Z amplitudes.

For the optimal control calculations, a smaller, 21-state model is chosen containing all 19 bound states and only two of the “continuum” states, namely $|n_r = 1, n_Z = 4\rangle$ and $|n_r = 0, n_Z = 15\rangle$, situated 88 and 134 cm^{-1} , respectively, above the desorption limit. Compare also Table 3.2 for quantum numbers and eigenenergies of the 21-state model. 21 vibrational states are still numerically tractable by the global OCT algorithm. The two kinds of “continuum” states to be distinguished are (compare also Fig. B.1):

- The “pure” states in Z $|n_r = 0, n_Z\rangle$, which although being localized have more of a “desorptive” character with the maximal spatial probabilities approaching $Z_{des} \approx 8.2 e a_0$ with increasing n_Z .
- The r/Z combination mode states $(n_r = 1, n_Z)$, localized closer to the potential minimum ($Z = Z_0$) and thus having a pronounced “pre-dissociative” character.

The optimal field obtained from the truncated, 21-level model is then applied to the “full”

(19+21 = 40)-state system, containing 19 further “continuum” states, up to 1136 cm⁻¹ above the desorption limit.

Two control pathways are set up to climb from the ground state to states above the desorption limit within the 21-state model. In one case (A), one quantum in r and four quanta in the Z mode are to be excited to populate state $|1, 4\rangle$. In the other case (B), successive “ladder climbing” in Z without r -excitation, *i. e.* $|0, 0\rangle \rightarrow |0, 1\rangle \rightarrow |0, 2\rangle \rightarrow \dots \rightarrow |0, 14\rangle \rightarrow |0, 15\rangle$, is the goal. The target operators used are

$$\hat{O}^{(A)} = 0.50 |1, 4\rangle\langle 1, 4| + \frac{0.25}{\sum_{i=1}^4 a_i} \sum_{i=1}^4 a_i |0, i\rangle\langle 0, i| \quad (4.3)$$

$$+ \frac{0.25}{\sum_{i=1}^4 a_i} \sum_{i=1}^4 a_i |1, i-1\rangle\langle 1, i-1|$$

$$\hat{O}^{(B)} = 0.5 |0, 15\rangle\langle 0, 15| + \frac{0.5}{\sum_{i=1}^{14} b_i} \sum_{i=1}^{14} b_i |0, i\rangle\langle 0, i| \quad , \quad (4.4)$$

where $a_1 < a_2 < a_3 < a_4$ and $b_1 < b_2 < \dots < b_{13} < b_{14}$. For the present calculations we chose: $a_1 = 1.0$, $a_2 = 1.1$, $a_3 = 1.2$, $a_4 = 1.3$ and $b_1 = 1.0$, $b_2 = 1.1$, $b_3 = 1.2$, $b_4 = 1.3 \dots$, $b_{13} = 2.2$, $b_{14} = 2.3$. The control time $t_f = 2000$ fs was chosen long enough to keep fluence and intensities small, but short enough to keep dissipation in check.

Shown in Fig. 4.4 are the population dynamics for three cases:

- In the top panels for a π pulse adjusted to the transition $|0, 0\rangle \rightarrow |0, 1\rangle$ which was also used as guess field for optimization;
- in the middle for the OCT pulse obtained for target (A), a shape function of type (4.2), and $\alpha = 0.793$;
- in the bottom panels for the OCT pulse obtained for target (B), the same shape function, and $\alpha = 0.222$.

The left panels thereby show the bound state populations with the ground state in black, the sum of “pure” Z states in green and the sum of all states of type $|1, n_Z\rangle$ with ($n_Z = 0, 1, 2, 3$) in orange. The right panels show the “continuum” state populations, in orange $|1, 4\rangle$ and in green $|0, 15\rangle$. Given additionally in dashed lines are the dynamics of the OCT pulses as applied to the larger, 40-state system. The green lines indicate here the sum of populations

of all states $|0, n_Z\rangle$ with $(n_Z = 15, 16, \dots, 29)$ and the orange lines the population sum of all states $|1, n_Z\rangle$ with $(n_Z = 4, 5, \dots, 8)$ as well as state $|2, 0\rangle$.

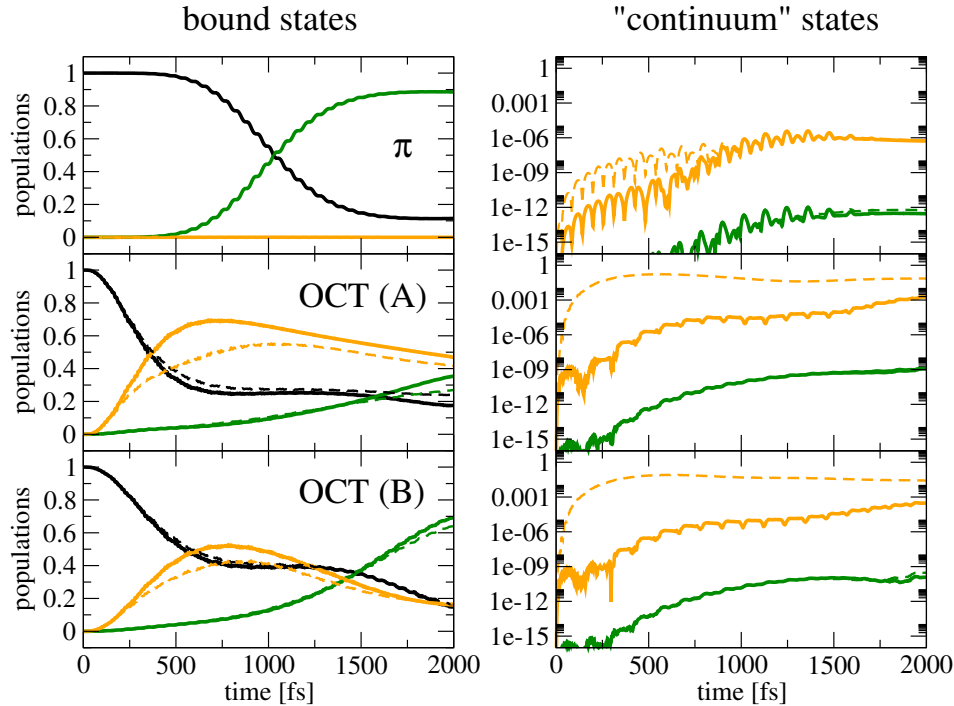


Figure 4.4: Vibrationally induced desorption in a 2D (r, Z) model: On the left bound state populations, on the right “continuum” state populations. Populations of the groundstate $|0, 0\rangle$ in black, sums of populations of “pure” states in Z $|0, n_Z\rangle$ in green and “pure” r states $|n_r, 0\rangle$ as well as “mixed” states $|n_r, n_Z\rangle$ in orange. Top panels: π pulse (adjusted to the fundamental transition in Z) dynamics for the 21-level system (solid lines) and the 40-level model (dashed lines); middle panels: OCT dynamics as obtained for target (A) and 21 levels (solid lines); lower panels: OCT dynamics as obtained for target (B) and 21 levels (solid lines); shown in dashed lines again is the dynamics of the OCT pulse applied on the 40-level system.

Although the π pulse for the Z excitation transfers about 90% of the population to bound $|0, n_Z\rangle$ states and almost none to bound $|1, n_Z\rangle$ states, the “continuum” state $|1, 4\rangle$ receives ca. a factor of 10^6 more population than state $|0, 15\rangle$. This ratio does not change for the two OCT pulses (each tuned to have a fluence of about 50 mJ/cm^2 to be comparable to the π pulse). Nevertheless, the OCT pulses improve the desorption yields by a factor of ca. 1000 in both cases. It is remarkable that although the bound state dynamics of the two OCT pulses

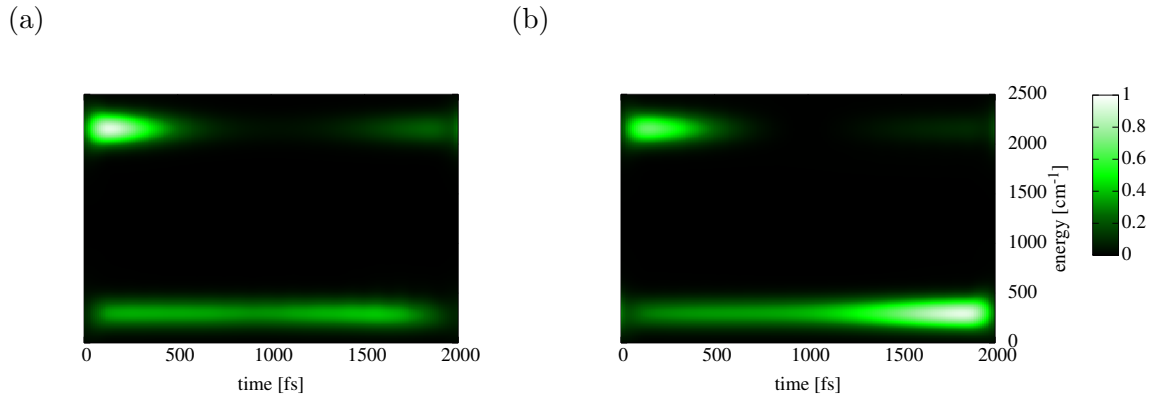


Figure 4.5: Vibrationally induced desorption in a 2D (r, Z) model: Husimi transformations of control pulses obtained by target operator (A) in (a) and by (B) in (b).

differ, the “continuum” state dynamics are rather similar. One can conclude that the Z mode alone is no good candidate for vibrational desorption and that whenever its “continuum” states are excited by the according frequency/-ies 1000 times more population reaches the (r, Z) combination mode. When one applies the above pulses to the 40-level system the total desorption yields increase from 0.002 to 0.07 (middle panel, target $\hat{O}^{(A)}$) and from 0.0003 to 0.03 (lower panel, target $\hat{O}^{(B)}$). In both cases this is due to the possibility of transitions to state $|2, 0\rangle$ which is favoured by a large dipole transition moment of $0.16 ea_0$ connecting it with state $|1, 0\rangle$. The latter becomes transiently ($t \approx 500 - 1500$ fs) populated by up to 0.35–0.40, so that the hot-band-excitation in r $|0, 0\rangle \rightarrow |1, 0\rangle \rightarrow |2, 0\rangle$ is possible if suitable frequencies ($\sim 2150 - 2130 \text{ cm}^{-1}$) are contained in the pulse. The additional “continuum” states of type $|1, n_Z\rangle$ and particularly of type $|0, n_Z\rangle$ can only “hold” marginally more population. The unfavoured population of pure Z states $|0, n_Z \geq 15\rangle$ is not due to faster vibrational relaxation. To give an example: Continuum state $|0, 15\rangle$ decays with a rate of $(1.5 \text{ ps})^{-1}$ back to the bound state $|0, 14\rangle$. The pre-dissociative “mixed” state $|1, 4\rangle$, lying only 46 cm^{-1} lower in energy than $|0, 15\rangle$, has a lifetime of $[(1.7 \text{ ps})^{-1} + (5.5 \text{ ps})^{-1}]^{-1} = 1.3 \text{ ps}$, where the first contribution stems from the decay process in the r mode $|1, 4\rangle \rightarrow |0, 4\rangle$ and the second contribution from decay in Z $|1, 4\rangle \rightarrow |1, 3\rangle$. Both $|0, 4\rangle$ and $|1, 3\rangle$ are bound states. The reason for the favoured population of “mixed” states in the “continuum”, as well as the r overtone $|2, 0\rangle$, is that (1) fewer one-photon transitions are needed to overcome the desorption barrier (5 vs. 15 for the lowest “continuum” states) and (2) the excitation of the (energy-rich) r mode is dipole favoured over Z mode excitation by a factor of 10.

The Husimi plots of pulse (A) and pulse (B) in Fig. 4.5 (a) and (b) each display both frequencies ($\sim 2200 \text{ cm}^{-1}$ and $\sim 300 \text{ cm}^{-1}$) related to r and Z transitions, respectively. In the first case (A), an early excitation in r overweighs, while Z transitions occur throughout on a smaller scale. In the latter case (B), although a late excitation in Z dominates, this pulse is even by a factor ~ 2 less successful in populating states ($0, n_Z \geq 15$) than pulse (A).

4.1.3 Three-dimensional model (r, Z, X) [96]

For the selective excitation by OCT pulses within the 3D model, containing 155 states up to the first excited state in r , a smaller sub-set of states was chosen to keep the problem numerically tractable¹. The easiest way to determine a suitable sub-set is to excite the “whole” system by π pulses adjusted to the fundamentals of the modes of interest (r , X , or Z) and the shortest pulse lengths which one will use. Then states getting only minimally populated by these pulses are “sorted out”. For the present system, the choice shown in Fig. 4.6 is reasonable: A 17-level system comprising the lowest 16 states plus state $|n_r = 1, n_Z = 0, n_X = 0\rangle$.

Excitation of the r mode

The r mode has a considerably larger fundamental frequency ($\omega_r = 2152 \text{ cm}^{-1}$) than Z mode ($\omega_Z = 293 \text{ cm}^{-1}$) and the lateral degree of freedom X ($\omega_X = 77 \text{ cm}^{-1}$). So, for the IR excitation of state $|1, 0, 0\rangle$ one expects to obtain no large difference between the OCT pulses obtained for a two-state minimal model as in Sec. 4.1.1 and the 17-state model. Further, for pulse durations short enough to keep dissipative effects small, a π pulse-like shape of the control field can be expected. Indeed, as shown in Fig. 4.7, with the choice $\hat{O} = |1, 0, 0\rangle\langle 1, 0, 0|$ for the target operator, global OCT calculations deliver very similar results for the electric field (top panel) and target population $P_{(1,0,0)}$ (lower panel) for 1D and 3D models. In the calculation, T was taken to be 10 K (state $|1, 0, 0\rangle$ relaxes within 1.7 ps), $t_f = 425 \text{ fs}$ and the penalty function in Eq. (4.2) with $\alpha = 5.0$ is used. Only during the first 100 fs, the OCT field for the 3D system displays a small additional substructure, but both pulses are in frequency ($\approx \omega_{(1,0,0)(0,0,0)}$) as well as shape (orange line in upper panel) very similar to the according

¹In the the global dissipative OCT algorithm the whole previous density / Lagrange multiplier matrix has to be kept in memory during each backward / forward propagation to evaluate Eq. (2.50).

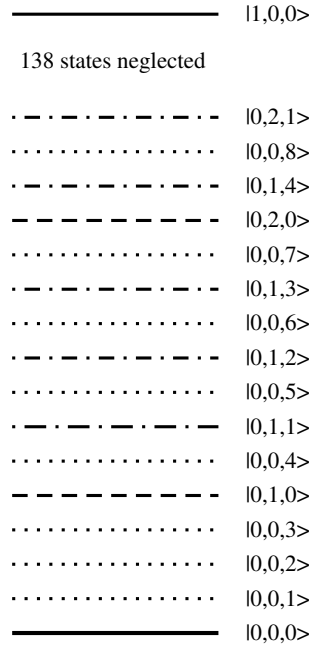


Figure 4.6: 3D sub-set, 17-level model used for the OCT calculations; the nomenclature for the quantum numbers is (n_r, n_Z, n_X) here and in the following.

π pulse and are able to transfer ca. 90 % from ground to first excited state.

The situation is different at ($T = 300$ K): State $|1, 0, 0\rangle$ decays only marginally faster to the ground state at this temperature with a rate of $(1.6 \text{ ps})^{-1}$, but the initial state no longer is practically identical with the ground state. It is a thermal ensemble populated according to Eq. (2.5) instead. As can be seen in the lower panel of Fig. 4.8, the ground state is only populated by about a quarter of the total population, and particularly the low-energetic “pure” states in X bear considerable amounts of population. The target operator is chosen as before, so the control scheme is that of a single pulse and the controllability is limited. In a previous work [120] it has been shown that the maximal population of a target state $|f\rangle$ obtainable by an optimal control scheme is

$$P_f^{max} = \rho_{00}(T, t = 0) \quad . \quad (4.5)$$

Here, $\rho_{00}(T, t = 0)$ is the Boltzmann population of the ground state, $\rho_{(0,0,0)(0,0,0)}(300 \text{ K}, t = 0) = 0.253$ in our case. In the present case, $P_{(1,0,0)} = 0.235$ as the final target population is reached, which is 93 % of the theoretical limit. The other states behave as “spectators”,

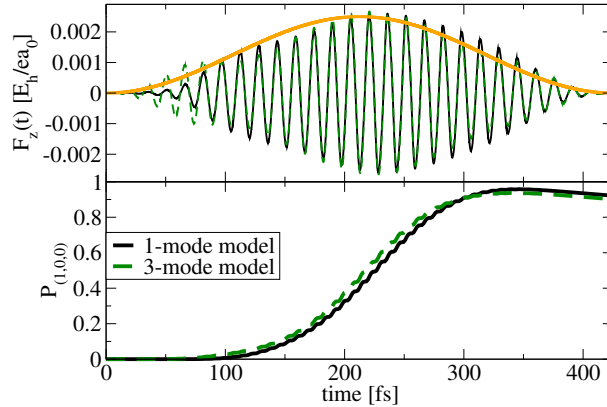


Figure 4.7: A comparison of optimal field (upper panel) and population dynamics (lower panel) of the target state $(1,0,0)$ for $(T = 10 \text{ K})$, control time $t_f = 425 \text{ fs}$, a target operator $\hat{O} = |1, 0, 0\rangle\langle 1, 0, 0|$, as obtained for the “1D” two-level model (dashed lines) and the “3D” 17-level model. Given for comparison in orange is $s(t)$, the (\sin^2) shape function of a π pulse obeying $|\mu_{(0,0,0)(1,0,0)}|F_0 = \int_0^{t_f} s(t)dt = \hbar\pi$ for $t_f = 425 \text{ ps}$.

their populations being almost constant throughout the control time². The control field is typical [30, 121] for medium to strongly dissipative scenarios with late intensity maximum – the pulse “waits” to lose not too much target population through an early population transfer into the objective state which decays before the pulse is off.

Excitation of the Z mode

In contrast to the r mode which is strongly IR active (see Table 3.5), the Z mode is of medium IR activity. Nevertheless, it is possible to excite state $(0,1,0)$ to about 90% at $(T = 10 \text{ K})$, see below. At this temperature state $|0, 1, 0\rangle$ decays only slowly, with a rate of $(22 \text{ ps})^{-1}$, back to the ground state $|0, 0, 0\rangle$ and the system is initially almost exclusively in the ground state. The questions addressed here are:

²This behaviour is due to the artificial character of the 17-state model, if states $|1, 0, 1\rangle$, $|1, 0, 2\rangle$, $|1, 0, 3\rangle$, $|1, 1, 0\rangle$, ... were included, they would be excited starting from states $|0, 0, 1\rangle$, $|0, 0, 2\rangle$, $|0, 0, 3\rangle$, $|0, 1, 0\rangle$, ..., respectively. Latter states would be depopulated, and the total amount of excitation in the r mode could exceed $P_{(1,0,0)}$, however, this would be no longer a state-selective process, only a mode-selective one.

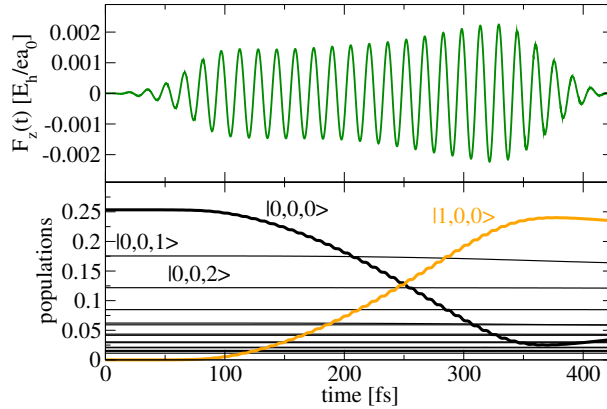


Figure 4.8: OCT field (upper panel) and populations (lower panel) of all 17 states as obtained at ($T = 300$ K) for the same parameters as in the low-temperature case above in Fig. 4.7.

- What is the effect of pulse duration on pulse shape/structure and population dynamics?
- Do higher “pure” states in Z $|0, 2, 0\rangle$, $|0, 3, 0\rangle$... become populated due to the harmonicity of Z ?
- Does the potential coupling to the two other modes influence the dynamics? (This was not the case for the r mode under the conditions studied here.)

Shown in Fig. 4.9 are fields (upper panels) and state populations (lower panels) as obtained at ($T = 10$ K) for (a) $t_f = 1250$ fs and (b) $t_f = 7250$ fs, a simple target operator $\hat{O} = |0, 1, 0\rangle\langle 0, 1, 0|$ and a penalty function $\alpha(t)$ of form (4.2) with $\alpha = 20.0$ in both cases.

As can be seen, unlike the longer pulse in (b), the short pulse (a) displays no late intensity maximum. Outside the regions in the first and last part of pulse duration where the penalty function enforces \sin^2 shape, it is almost cw-like instead. Noticeable is the high-frequency superimposition between $t \approx 500$ and $t \approx 1100$ fs. Within this time-interval, state $|1, 0, 0\rangle$ is transiently populated with a probability of up to 0.1. The Husimi analysis (not shown here) confirms a contribution at an energy around the fundamental frequency (2153 cm^{-1}) of the r mode. But state $|1, 0, 0\rangle$ gets almost completely depopulated again before the pulse is off. The same is true for the second excited state in Z ($0, 2, 0$), which is transiently populated strongly / weakly by the short / long pulse. As only frequencies fitting to single quantum transitions in Z (around 290 cm^{-1}) are found in the Husimi analysis, an overtone transition $|0, 0, 0\rangle \rightarrow |0, 2, 0\rangle$

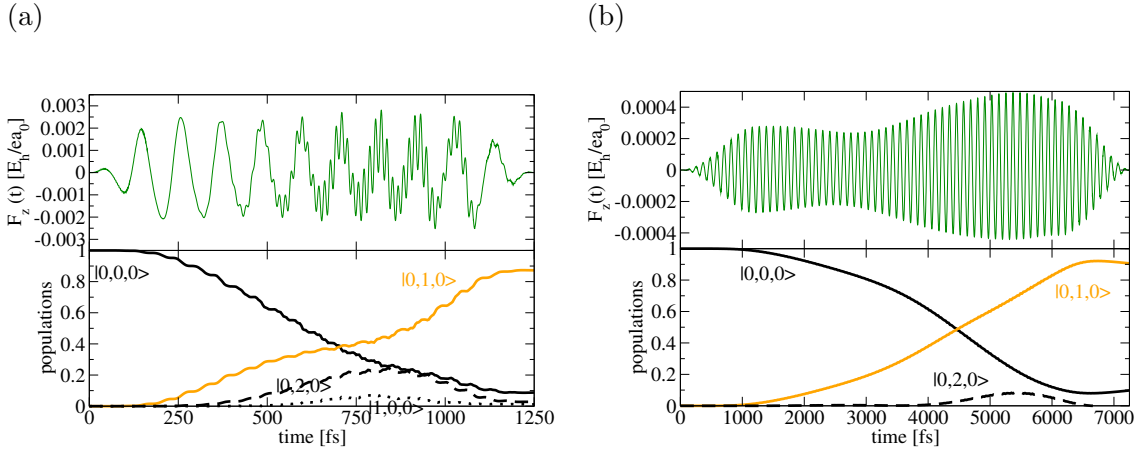


Figure 4.9: Short 1250 fs (a) and long 7250 fs (b) OCT pulses to selectively excite state $|0, 1, 0\rangle$ at ($T = 10$ K) in the 3D 17-level system of Fig. 4.6.

does not take place, the overtone is excited via $|0, 0, 0\rangle \rightarrow |0, 1, 0\rangle \rightarrow |0, 2, 0\rangle$. Thus, one can conclude the following.

- There is a coupling to the r mode if one excites Z , but only for short pulses, that is high intensities / fluences which broaden the spectral width of the pulse (compare Fig. H.3).
- The overtone $|0, 2, 0\rangle$ gets excited, even considerably by the short OCT pulse being broader in frequency and thus being able to cover $\omega_{(0,2,0),(0,1,0)} = 283 \text{ cm}^{-1}$ which is slightly smaller than $\omega_{(0,1,0),(0,0,0)} = 293 \text{ cm}^{-1}$. The OCT algorithm achieves its depopulation via $|0, 2, 0 \rightarrow |0, 1, 0\rangle$ towards the end of the pulse; dissipation is not thought to play a big role in this process as $\Gamma_{(0,2,0)\rightarrow(0,1,0)} = (11 \text{ ps})^{-1}$, while the depopulation occurs on a scale of few 100 fs.

Excitation of the X mode and a combination of Z and X modes

Due to the dipole function $\mu_z(r, Z, X) = \mu_z(r, Z)$ according to Eq. (3.8) used for the present calculations, the fundamental transition in X $|0, 0, 0\rangle \rightarrow |0, 0, 1\rangle$ is dipole-forbidden, but overtone excitations of type $|0, 0, n_X\rangle \rightarrow |0, 0, n_X \pm 2\rangle$ are weakly allowed (see Table 3.5). Shown in Fig. 4.10 is the attempt to excite state $|0, 0, 2\rangle$ at ($T = 10$ K) with a 4900 fs OCT

pulse. High intensities ($I^{max} \approx 1 \cdot 10^{12} \text{ W/cm}^2$) and fluences (here: 5200 mJ/cm^2) are needed to transfer slightly more than 50% of the population from the ground to the target state. Due the high field strength, there is strong field coupling to the Z mode. Thus, $|0, 1, 0\rangle$ as well as $|0, 1, 2\rangle$ – not shown for lucidity – get populated and the populations of these states oscillate with the field (the dominant frequency being that of the $|0, 0, 0\rangle \rightarrow |0, 0, 2\rangle$ transition: 153 cm^{-1}). Coupling to states $|0, 1, 0\rangle$ and $|0, 1, 2\rangle$ are states $|0, 0, 0\rangle$ and $|0, 0, 2\rangle$, respectively. State $|0, 0, 1\rangle$ is also populated slightly, through vibrational decay from the target $|0, 0, 2\rangle$ with a rate of $(7 \text{ ps})^{-1}$. The translational modes X and Y might be important

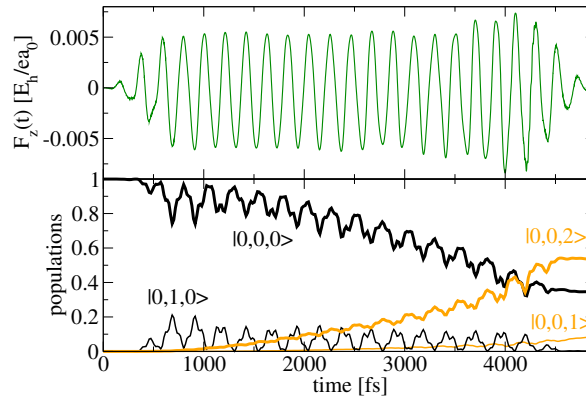


Figure 4.10: Optimal field (upper panel) and population dynamics (lower panel) for the excitation of state $|0, 0, 2\rangle$ at ($T = 10 \text{ K}$) within the 17-level model, $\hat{O} = |0, 0, 2\rangle\langle 0, 0, 2|$ and a shape function according to Eq. (4.2) with $\alpha = 10.0$.

to access for diffusion.

Finally, also the excitation of a combination of X and Z modes, namely state $|0, 1, 2\rangle$ is attempted. Starting from the ground state $|0, 0, 0\rangle$, two intermediate states are possible (a direct excitation is not favoured, as the dipole transition moment is very small):

- The state state $|0, 1, 0\rangle$ which relaxes within 22 ps before decay to the ground state. State $(0,1,0)$ has a medium dipole activity.
- The weakly dipole active state $|0, 0, 2\rangle$, with a lifetime of 7 ps with respect to the ground state.

It turns out that irrespective of how the target operator is chosen, the first variant $|0, 0, 0\rangle \rightarrow |0, 1, 0\rangle \rightarrow |0, 1, 2\rangle$ is favoured, where the weakly allowed transition to the shorter-lived state

takes place in a second step. Shown in Fig.4.11 is an example for such an OCT pulse generated for $t_f = 4900$ fs and ($T = 10$ K). Maximal intensity and fluence are high (similar to the above case where the “pure” X state is excited), but the selectivity is rather small with scarcely 40% population transfer to the target. Nevertheless, $|0,1,2\rangle$ is the highest populated state at $t = t_f$ and most of the “loss” remains / decays back to the intermediate state $|0,1,0\rangle$ and could, in principle, be excited from there again to the target state. Such an approach is known as “laser distillation” [122,123].

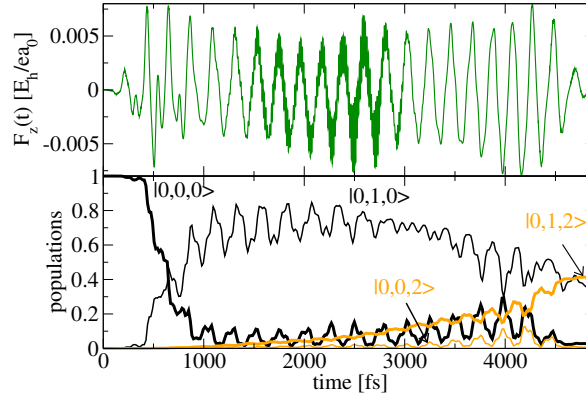


Figure 4.11: Optimal field (upper panel) and population dynamics (lower panel) for the excitation of state $|0,1,2\rangle$ at ($T = 10$ K) within the 17-level model, $\hat{O} = |0,1,2\rangle\langle 0,1,2|$ and a shape function according to Eq. (4.2) with $\alpha = 10.0$.

4.1.4 Four-dimensional model (r, Z, θ, ϕ) [97]

In Ref. [97], Tremblay *et al.* used the present implementation of global OCT, for a 4D model (r, Z, θ, ϕ) including the angular degrees of freedom. The needed eigenenergies and eigenfunctions were calculated in Ref. [97] using a coupled two-term Lanczos eigensolver, see Appendix A.3. The dipole function $\mu_z(r, Z, \theta, \phi)$ of Eq. (3.10) was used for dipole moments μ_{mn} , and the Golden Rule approach as sketched in Sec. 3.1.3 for the relaxation rates. The energies and dipole moments for the fundamental transitions in r , Z , θ and ϕ within the 4D model are 2150 , 347 and 329 cm^{-1} (latter value being degenerate for θ and ϕ) and 0.145 , 0.0422 , 0.00327 and $1.38 \cdot 10^{-12}$ ea_0 . For further dipole transition moments and vibrational relaxation rates see Table 3.8 in Sec. 3.1.3. The vibrational states are labeled as $|n_r, n_Z, n_\theta, n_\phi\rangle$ in the following. Note, that both states $|0,0,0,2\rangle$ and $|0,0,1,0\rangle$ decay to state $|0,0,0,1\rangle$ with

a rate of $(1.15 \text{ ps})^{-1}$. For the OCT calculation presented below, a 23-level sub-system of the full 121-level system up to and including state $|1, 0, 0, 0\rangle$ was used, chosen via the same procedure as above in the 3D case: Applying π pulses adjusted to the fundamental transitions in each mode and sorting out “inactive” *i. e.* negligibly populated, states. Within their 4D model, Tremblay *et al.* were able to excite r and Z modes by OCT, similar to what was described in the previous sections. Due to the much smaller transition moments, however, excitation of the θ and ϕ modes is much less straightforward. In the following, we shall restrict ourselves to the angular modes only.

Excitation of θ and ϕ modes

The transition dipole moments for “pure”, single quantum transitions in θ , *i. e.* $(n_\theta \rightarrow n_\theta + 1)$, are of the same order of magnitude than that for the overtone excitation of the dark mode X in the above Sec. 4.1.3. Thus, similarly strong fields are needed to excite $|0, 0, 1, 0\rangle$. In fact, the control field one obtains for the example in Fig. 4.12 (a) ($t_f = 1000 \text{ fs}$, $\hat{O} = |0, 0, 1, 0\rangle\langle 0, 0, 1, 0|$, penalty function $\alpha(t)$ of type (4.2) and $\alpha = 0.1$), has intensities $I^{max} = 1.7 \cdot 10^{13} \text{ W/cm}^2$ and a fluence ($f = 6300 \text{ mJ/cm}^2$) which are both high. The target state is populated with a probability of 0.43 at $t = t_f$ within the 23-level sub-system the pulse was optimized for (not shown). This value drops to 0.27 for the complete 4D model with all 121 states up to state $|1, 0, 0, 0\rangle$, see the lower panel of Fig. 4.12 (a). The main loss is due to population of “pure” Z modes $(0, n_Z, 0, 0)$, most prominently states $|0, 1, 0, 0\rangle$, $|0, 2, 0, 0\rangle$ and $|0, 4, 0, 0\rangle$. Note, that the resonance frequencies of both modes Z and θ are similar with about $330\text{-}350 \text{ cm}^{-1}$, but the transition dipoles of the Z mode are one magnitude larger than those in θ . There is also transient excitation of combination modes $(0, n_Z, n_\theta, 0)$. In both cases, populations oscillate approximately in parallel with the field oscillations, which are quite complex. Therefore, the plot of the field’s Husimi analysis is shown in Fig. 4.12 (b). There are contributions between $300\text{-}400 \text{ cm}^{-1}$ which can be assigned to both single quantum transitions in Z and θ . Further, weaker signals around twice that frequency domain are observed, indicating two-quantum transitions $(n_Z/n_\phi \rightarrow n_Z/n_\phi + 2)$. An interesting feature is the very low-energetic “static field” contribution (frequency ca. 20 times smaller than the resonance frequencies in Z and θ), dominating for $t \approx 250 - 800 \text{ fs}$: It is thought that, similar to the STIRAP (successive stimulated Raman adiabatic passage) mechanism [124, 125], the laser here couples to states $|0, 2, 0, 0\rangle$ and $|0, 3, 0, 0\rangle$ to form a so-called “dressed state”, which is then depopulated by the third short pulse towards the end of the control time, centered at the resonance frequency.

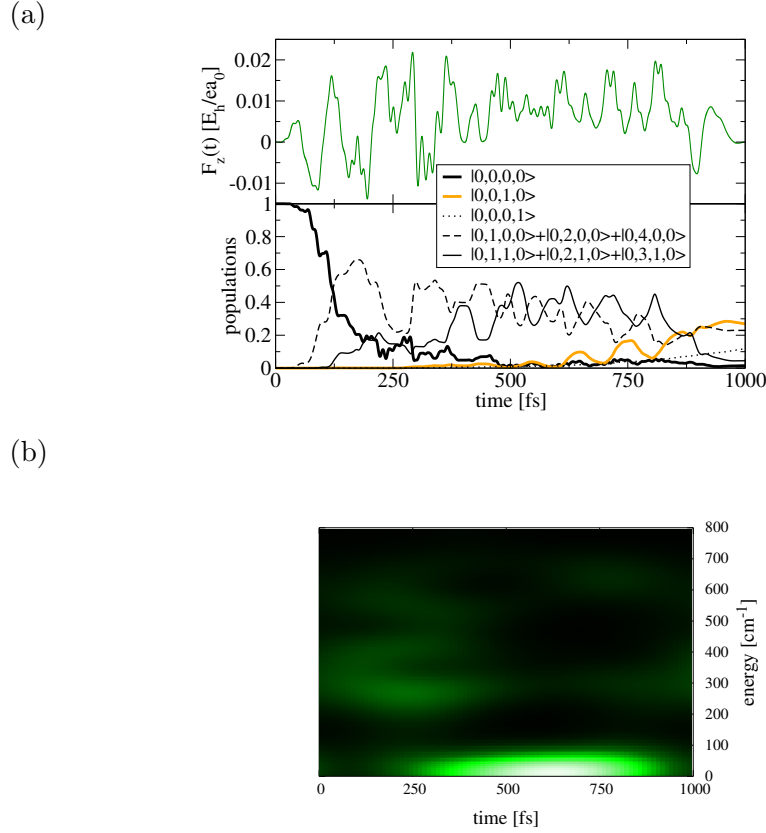


Figure 4.12: Excitation of the fundamental transition in θ $|0,0,0,0\rangle \rightarrow |0,0,1,0\rangle$ at ($T = 0$ K) by global OCT: (a) Control field (upper panel), obtained for a truncated 23-level system and the dynamics of selected states $|n_r, n_Z, n_\theta, n_\phi\rangle$ it triggers in the complete 121-level system; (b) Husimi transformation of the OCT field of (a).

The first excited state in ϕ receives a population of 0.12 at the end of the pulse. This is not achieved by direct excitation from either $|0,0,0,0\rangle$ or $|0,0,1,0\rangle$ but through vibrational decay from states excited in a combination of Z and θ mode.

So, in order to access state $|0,0,0,1\rangle$ Tremblay *et al.* started with the above 1 ps OCT pulse obtained for the θ mode and a successive free decay ($F_z(t) = 0$ for $1.0 \text{ ps} < t \leq 2.0 \text{ ps}$ as initial field) and optimized this using shape function $\alpha(t)$ of type (4.2) with $\alpha = 0.03$, target operator $\hat{O} = |0,0,0,1\rangle\langle 0,0,0,1|$ and again the 23-level sub-system. Within this model the target can be populated with a probability of 0.53. Applying the such obtained pulse ($I^{max} = 4.0 \cdot 10^{13} \text{ W/cm}^2$, $f = 11100 \text{ mJ/cm}^2$, upper panel of Fig. 4.13 (a)) to the full 4D

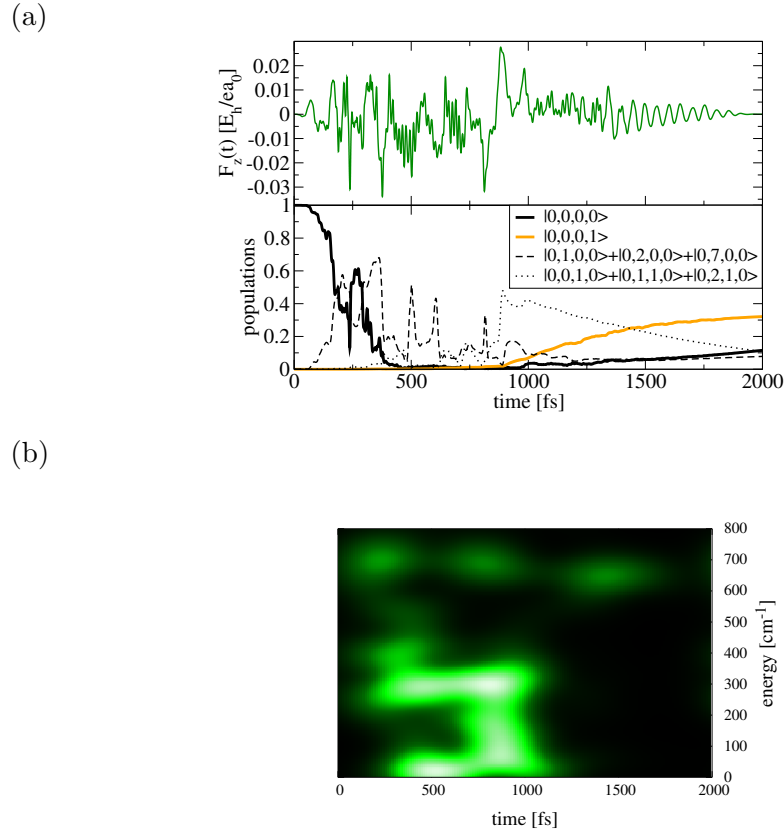


Figure 4.13: Excitation of the fundamental transition in ϕ $|0,0,0,0\rangle \rightarrow |0,0,0,1\rangle$ at ($T = 0$ K) by global OCT: (a) Control field (upper panel), obtained for a truncated 23-level system and the dynamics of selected states $|n_r, n_Z, n_\theta, n_\phi\rangle$ it triggers in the complete 121-level system; (b) Husimi transformation of the OCT field of (a).

model with 121 levels, this value is reduced to 0.32 (see Fig. 4.13 (a), lower panel). Main losses are to states $|0,0,1,0\rangle$ and $|0,1,0,0\rangle$, and significant population of other Z/θ combination and “pure” Z mode states was also observed.

The Husimi analysis of the pulse in Fig. 4.13 (b) reveals, just like the population dynamics, the two stages of the reaction mechanism:

- For ($t < 1000$ fs) one has slightly “chirped” contributions, centered around 350 and 700 cm^{-1} , which can be assigned to one- and (weaker) two-photon transitions in Z/θ . These occur along with the no longer dominating low-energetic “static field”. Regarding

the population dynamics, it is difficult to draw a definite mechanism here.

- For ($t > 1000$ fs), where the initial field was chosen to be zero, to allow for (among other processes) a free decay $|0, 0, 1, 0\rangle \rightarrow |0, 0, 0, 1\rangle$ with a rate of $(1.15 \text{ ps})^{-1}$, the OCT algorithm creates an exponentially decaying field. The main frequency of this decaying field is about 650 cm^{-1} . A possible explanation is that the field hinders the decay of $|0, 0, 0, 1\rangle$ to the ground state $|0, 0, 0, 0\rangle$, which happens at a rate of $(2.3 \text{ ps})^{-1}$.

In Ref. [97] also the stationary 6D problem (r, Z, X, Y, θ, ϕ) was solved. However, due to the many vibrational states involved even for low-energetic “cuts” in the eigenspectrum the IR-dynamics and particularly the application of global OCT, is too complex to handle at the moment³. But as the X/Y modes are well decoupled, due to their low frequency, from the other four modes, and the lateral dipole dependence is expected to be very small, the 4D model is probably already a sufficient description of CO/Cu(100).

In summary, it was found that selective IR-excitation is feasible within the multi-dimensional models of CO/Cu(100) although both a coupling to the bath (dissipation and dephasing) and inter-mode coupling takes place. Choosing pulse lengths suitably with respect to vibrational lifetimes, the dissipative loss can be kept small at about 10 %. For the stretch modes r and Z even state-selectivity is possible. The “dark” lateral mode X was accessed via overtone excitation. The the weakly dipole active angular mode ϕ was excited utilizing energy relaxation of the previously excited θ mode. Intermode coupling was observed only at very high field strengths and between modes of similar resonance energies (Z and θ).

³In cooperation with Scott Greenwald (Freie Universität Berlin), so-called *balancing* [126–128] is fused with OCT, in order to reduce the dimension of matrices in an automated way.

4.2 H/Si(100) [104]

In this section, simulations of the system dynamics in one- (r) and two-dimensional (r, Z) models of H/Si(100) (Sec. 3.2) are presented.

4.2.1 One-dimensional model (r)

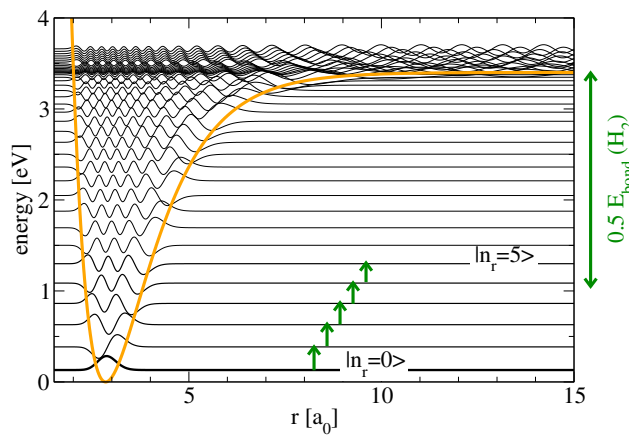


Figure 4.14: 1D potential energy curve $V(r)$ as obtained from Eq. (3.17) by setting ($\phi = \phi_0$) with the 40 vibrational eigenstates $|\psi_{n_r}\rangle \equiv |n_r\rangle$ calculated by sinc-DVR (Sec. A.1) using a grid of 40 points with $r \in [1.5, 15.0]$ ea $_0$. Shown on the right is half energy gained by the bond formation of H_2 .

In the recent, experimental success to isotope selectively break a bond by vibrational excitation [14] – namely the desorption of H_2 from a Si(111) surface on which hydrogen and deuterium atoms were co-adsorbed – it was shown that the H–Si stretch mode is excited thereby. Using the related system H/Si(100), already previously studied [51,52], and a simple 1D model for the H–Si stretch mode r (compare Fig. 3.3 and Sec. 3.2), a similar scenario is studied in the following. Shown in Fig. 4.14 are the potential curve $V(r)$ and the vibrational eigenstates $|n_r\rangle$. Through the bond formation $\text{H} + \text{H} \rightarrow \text{H}_2$ about 4.6 eV are set free. For a single H atom, as considered in the present model, this would mean an energy “gain” of 2.3 eV (see double arrow on the right of Fig. 4.14) from desorption. On the other hand, breaking a single Si–H bond “costs” about 3.4 eV according to Fig. 4.14. Thus, by promoting the system by roughly $(3.4 - 2.3)$ eV = 1.1 eV in vibrational energy per Si–H bond a vibrationally

mediated desorption should energetically be possible. Since the Si–H stretch mode has a vibrational frequency of about 0.25 eV, this requires – if anharmonicities are accounted for – about 5 vibrational quanta (see the arrows in Fig. 4.14).

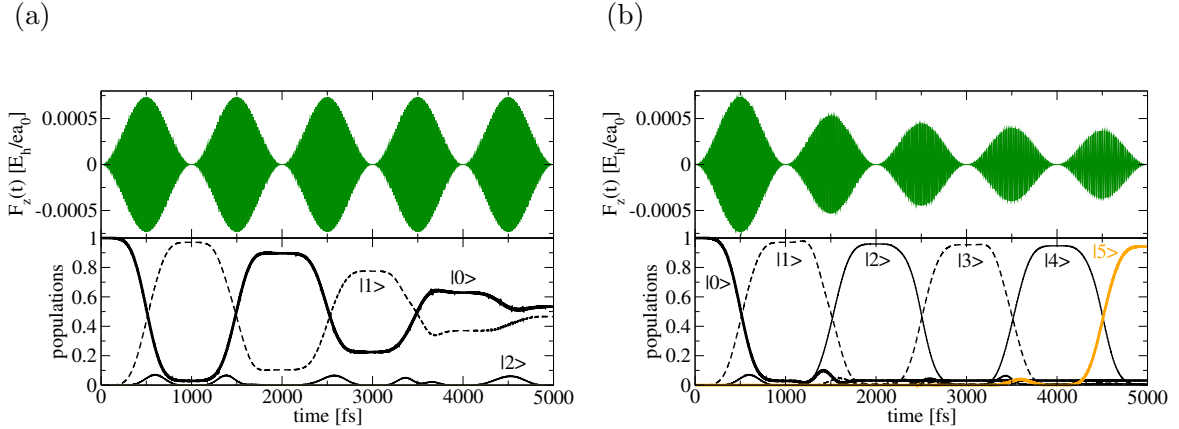


Figure 4.15: Excitation of state $|5\rangle$ at ($T = 0$ K) via vibrational “ladder climbing” from the ground state $|0\rangle$: (a) Five successive, \sin^2 -shaped 1 ps π pulses adjusted to the transition $|0\rangle \rightarrow |1\rangle$ and (b) Five successive, \sin^2 -shaped 1 ps π pulses adjusted to transitions $|0\rangle \rightarrow |1\rangle$, $|1\rangle \rightarrow |2\rangle$, $|2\rangle \rightarrow |3\rangle$, $|3\rangle \rightarrow |4\rangle$, and $|4\rangle \rightarrow |5\rangle$ from left to right. The total fluences of fields (a) and (b) are 36 and 17 mJ/cm², respectively; the maximum intensity is $1.9 \cdot 10^{10}$ W/cm² in both cases (the sub-pulse intensity for the fundamental transition).

The r mode is long-lived, with the first excited state $|1\rangle$ surviving for nanoseconds according to experiment [53]; here the theoretical lifetime for ($T = 0$ K) of 2.13 ns, in accordance with Table 3.10, is chosen. The rates for higher excited states are calculated according to Eq. (2.31) for ($T = 0$ K).

The 40 states shown in Fig. 4.14, some of them above the desorption energy, were then taken as a basis for the solution of the Liouville-von Neumann equation according to Eq. (2.13). The goal was to excite vibrational state $|5\rangle$ by IR pulses. Fig. 4.15 shows electric fields (upper panels) and populations (lower panels) of states $|i\rangle$ for two different excitation scenarios of the 40-level model: In (a) five successive, \sin^2 -shaped 1 ps π pulses adjusted to the transition $|0\rangle \rightarrow |1\rangle$ are used, while in (b) again five 1 ps π pulses are used, but adjusted in frequency and fluence to transitions $|0\rangle \rightarrow |1\rangle$, $|1\rangle \rightarrow |2\rangle$, $|2\rangle \rightarrow |3\rangle$, $|3\rangle \rightarrow |4\rangle$, and $|4\rangle \rightarrow |5\rangle$ from left to right. In the first case, one mainly observes a damped Rabi oscillation between states $|0\rangle$ and $|1\rangle$, $|2\rangle$, the next state up the ladder, is scarcely populated at all. The r mode is too anharmonic for “mode selective” excitation (as observed, for example, in Sec. 4.2.2 below

for the ϕ mode). In contrast, one gets 94.2% state selective population of $|5\rangle$ in case (b), with each π pulse succeeding almost in complete population inversions and an almost perfect successive “ladder climbing”. In experiment, either a down-“chirped” cw-like-field with decreasing intensity or a sequence of pulses with fine-tuned frequency and intensity/fluence, as simulated in the above, should be successful in this case. Note, that in Ref. [14] a train of unchirped 1 ps pulses has been used. The excitation of higher vibrational states may then still be due to so-called energy pooling [129], where dipole-dipole interactions mediate vibrational quantum exchanges; a process which was neglected here.

4.2.2 Two-dimensional model (r, ϕ) [104]

In the 2D model, in addition to r also the bending mode ϕ is included – see Fig. 3.3. The topics of interest in the 2D model of H/Si(100) are selective vibrational excitation, but also how the often used Markov approximation (Sec. 2.2) of density matrix dynamics differs from the more general non-Markovian model (Appendix G). All non-Markov calculations were carried out by Guennadij Paramonov (Academy of Sciences, Minsk, Belarus and Freie Universität Berlin). For the field-free time evolution as well as the density matrix propagations with \sin^2 -shaped IR pulses the lowest 50 eigenstates in the 2D (n_r, n_ϕ) are used. In order to retrieve optimal control fields via global OCT calculations choosing the lowest 22 states has been found to be sufficient, for the targets to be defined below.

Field-free decay

In a first step the field-free ($F_z(t) = 0$) decay of exemplary vibrationally excited states – namely $|n_r = 0, n_\phi = 4\rangle$ and $|n_r = 1, n_\phi\rangle$ – is examined. The bath temperature is chosen finite, but very low, as 4 K (*i. e.* “upward” rates are vanishingly small), also for the simulations of IR excitations below. The relaxation rates are those of Ref. [52] for ($T = 0$ K) – compare Table 3.10. The coupling parameters needed in the non-Markovian model (see Appendix G) were chosen such [104] that the decay times states of $|0, 1\rangle$ and $|1, 0\rangle$ in the Markovian approximation were reproduced. This approach assures that the overall vibrational lifetimes in both models agree with each other, however, only for small quantum numbers. Also, the detailed time-behaviour will be different.

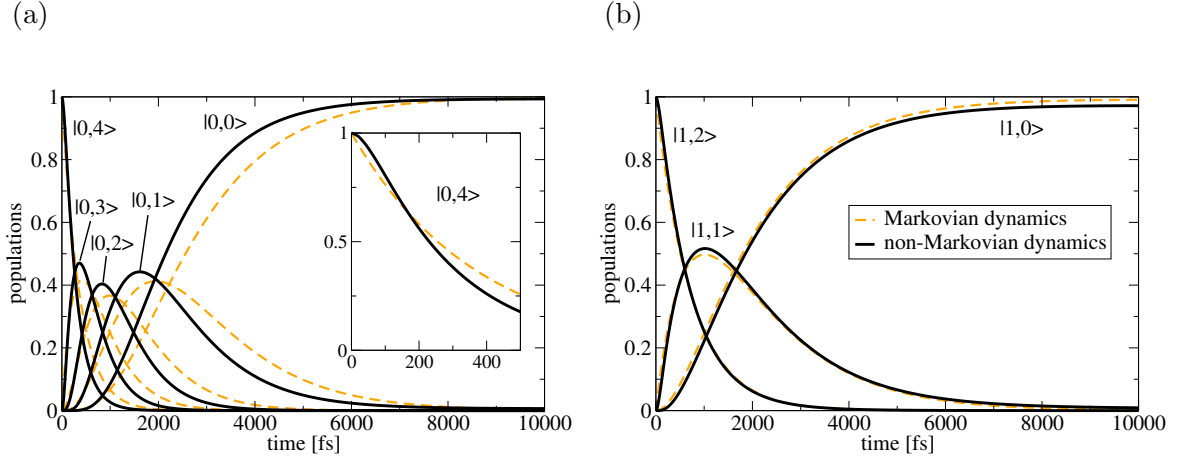


Figure 4.16: Free evolution over 10 ps of initially pure states $|n_r = 0, n_\phi = 4\rangle$ (a) and $|n_r = 1, n_\phi = 2\rangle$ (b) at ($T = 4$ K). Shown in solid lines is the non-Markovian dynamics, given for comparison in dashed lines are the results obtained from Markovian approximation.

Shown in Fig. 4.16 are the population dynamics for a free decay over a period of 10 ps starting at ($t = 0$) with the pure states $|0, 4\rangle$ in (a) and $|1, 2\rangle$ in (b), respectively. The populations obtained by the non-Markovian model are plotted in solid black lines, those from the Markovian approximation in dashed orange lines. As for the decay mechanism, one observes for the four-fold excited “pure” ϕ mode state (a) a rapid (lifetimes ranging from some hundreds of fs to a bit more than one ps) “reverse ladder climbing” back into the ground state: $|0, 4\rangle \rightarrow |0, 3\rangle \rightarrow |0, 2\rangle \rightarrow |0, 1\rangle \rightarrow |0, 0\rangle$. In accordance with energy relaxation rates being roughly proportional to the quantum number n_ϕ of the initial state in each ($n_\phi \rightarrow n_\phi - 1$) sub-process, $|0, 4\rangle \rightarrow |0, 3\rangle$ occurs on a faster time-scale than $|0, 3\rangle \rightarrow |0, 2\rangle$ and so on. After 10 ps, the four excited states are quasi depopulated. Although for ($t \rightarrow \infty$)⁴ Markovian and non-Markovian populations approach each other – both running asymptotically towards the Boltzmann distribution at ($T = 4$ K) – there are two main differences:

- The decay of the initial state is exponential in the Markovian case (see inlay of Fig. 4.16(a)), whereas the non-Markovian decay is initially non-exponential (Gaussian-like) with $\lim_{t \rightarrow 0} \frac{dP_n}{dt} = 0$.
- The heights as well as positions of the population maxima for the intermediate states differ for both models. It appears as if the Markovian decay is delayed with the tails

⁴“ ∞ ” here means $t \gg \tau_{(0, n_\phi)}$.

of the intermediate “ladder” states being longer. This could be due to (1) a different functional behaviour of the $P_n(t)$ for ($t \rightarrow \infty$) and not only for ($t \rightarrow 0$) – though with the same value in the limit – and/or (2) small differences in the vibrational lifetimes for quantum numbers ($n_r, n_\phi > 1$).

Except for small times t where again an exponential (Markov) vs. Gaussian (non-Markov) behaviour of the initial state population $P_{(1,2)}(t)$ is observed, the differences in the intermediate dynamics are less pronounced in (b). The reason for this is that only two one-photon decay (instead of four as in above case) processes take place within $t_f = 10$ ps: Two fast transitions $|1, 2\rangle \rightarrow |1, 1\rangle \rightarrow |1, 0\rangle$. Thus, the different functional behaviour in the state populations’ tails does not accumulate so much as in case (a).

Excitation of the r mode

The strongly IR active and long-lived r mode is well and state-selectively excitable as can be seen in the above 1D calculations of Sec. 4.2.1. Due to the weak (r, ϕ) coupling, the same is true within the 2D model, so that the successful, almost complete population inversion $|0, 0\rangle \rightarrow |1, 0\rangle$ is possible when \sin^2 pulses similar to those above are employed (not shown). The only important results to draw from these calculations, where the sub-ps and ps \sin^2 pulses were “hand-optimized”, are:

- Similar to the example in Sec. 4.1.3 it is found that too short pulses ($t_f < 1$ ps) lead to a loss in final population of state $|1, 0\rangle$ as the overtone $|2, 0\rangle$ becomes considerably excited even after the pulse is off. This is because state $|2, 0\rangle$ has also a ns lifetime. To avoid this loss of state-selectivity longer pulses have to be used.
- The difference between Markovian and non-Markovian models is small and mainly transient; this is due to the small relaxation rates (which “represent” the bath modes) for this long-lived mode – “memory effects” are less important in case of weaker system-bath coupling.

Excitation of the ϕ mode

More interesting here is the question as to whether and how selective excited states in ϕ can be accessed. This mode has lifetimes in the order of ps, *i. e.* on the same timescale of IR pulses used here. Further, this mode has a rather harmonic eigenspectrum due to the functional form (quadratic) chosen for $V(r, \phi)$, see Eq. (3.17) and Table 3.9. Finally, it shows only medium IR activity, because μ changes less with ϕ than with r .

In Ref. [104] “hand-optimized” \sin^2 pulses (duration t_f , maximal field strength F_0 and constant carrier frequency ω being the parameters) were constructed to selectively excite state $|0, 1\rangle$ within the non-Markovian model. Shown in Fig. 4.17 in solid black lines is one of the best

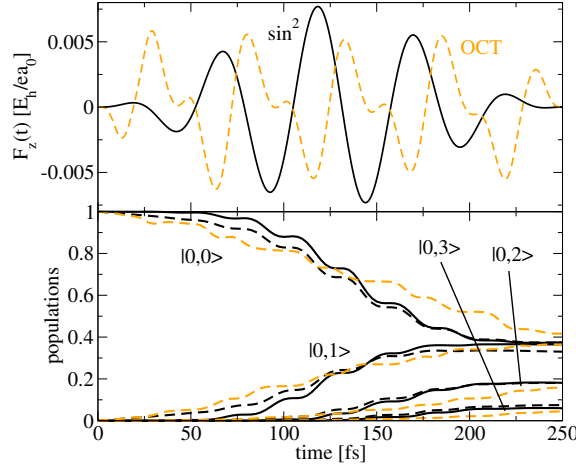


Figure 4.17: Excitation of state $|n_r = 0, n_\phi = 1\rangle$ at ($T = 4$ K) by a “hand-optimized” \sin^2 -shaped pulse (black lines) of duration 0.25 ps, maximum field strength $F_0 = 0.007755 E_h/ea_0$ and carrier frequency $\omega = 635.2 \text{ cm}^{-1}$. Shown in solid lines is the field (upper panel) and the population dynamics (lower panel) for the non-Markovian case for which the pulse was optimized; plotted in dashed lines is the non-Markovian dynamics as obtained for the same pulse. Shown in orange dashed lines is the OCT field and population dynamics obtained within the non-Markovian approximation with $\hat{O} = |0, 1\rangle\langle 0, 1|$, a penalty function of type 4.2 and $\alpha = 0.1$.

results that was obtained in Ref. [104] with parameters $t_f = 250$ fs, $F_0 = 0.007755 E_h/ea_0$ ⁵

⁵For a π pulse the according maximal field strength would be larger with $0.01203 E_h/ea_0$ – the idealization as dissipation-free two-level system does not hold true here.

and $\omega = 635.2 \text{ cm}^{-1}$ ($\omega_\phi = 637.0 \text{ cm}^{-1}$). State $|0, 1\rangle$ is populated by only 0.3646 at ($t = t_f$), while overtones $|0, 2\rangle$ and $|0, 3\rangle$ are rather strongly populated with 0.1812 and 0.05989, besides even higher states carrying populations of 1 % or more. The population in the ground state remains high (0.3756). This is a typical behaviour for a harmonic system: Not the first excited state is selectively populated by irradiation with light of the fundamental resonance frequency, but *all* states of this mode get populated, the population normally decreasing for increasing quantum numbers. Since no other modes are excited, this is so-called “mode selectivity” instead of “state selectivity” as in most examples above. Further improvement of state-selectivity was not possible with a single pulse. Plotted in dashed black lines in the lower panel of Fig. 4.17 is the Markovian dynamics obtained for the same pulse. Similar to the field-free evolution above, some small differences between both models are observed. As the pulse is optimized for the non-Markovian case, the population of state $|0, 1\rangle$ at ($t = t_f$) is even smaller with 0.3301. The “lacking” population does not remain in the ground state (which is populated with 0.3738 at final time, similarly to the non-Markovian case), but is mainly transferred to the overtone states. Obviously, a “hand-optimized” pulse for the Markovian case will improve the target yield somewhat.

Instead of a “hand-optimization”, an OCT calculation (in the Markov picture) was carried out. The pulse (upper panel, orange) has an interesting structure: Except for beginning and end, where a penalty function analogous to Eq. (4.2) constrains the field to a \sin^2 -shape, its dominant component is cw-like and thus allows for somewhat smaller intensities. A second component with weaker intensity is observed which at the first look might constitute a higher frequency, possibly to (de)excite the first overtone $|0, 2\rangle$ directly from (to) the ground state. But the Husimi analysis reveals only a single frequency of about $\omega_\phi = 637 \text{ cm}^{-1}$. This can only mean that a small fraction of the resonant field is *phase-shifted* with respect to the dominant fraction. It is believed that this special mechanism can, to some extent, counteract the excitation of overtone states. And indeed, states $|0, 2\rangle$, $|0, 3\rangle$ etc. are less populated than in case of the \sin^2 pulse, not only for the Markov model, but also when compared to the non-Markovian case. Although, the target population (0.3636) does not exceed the value of the latter, more population remains in the ground state with the present OCT pulse and is not lost into higher excited ϕ states.

The pronounced harmonicity of a mode, as here the case of ϕ , is not necessary an obstacle for vibrational excitation in general. It is possible to excite a single mode if not state-selective, but by transferring population into high-energetic states of latter with still moderate

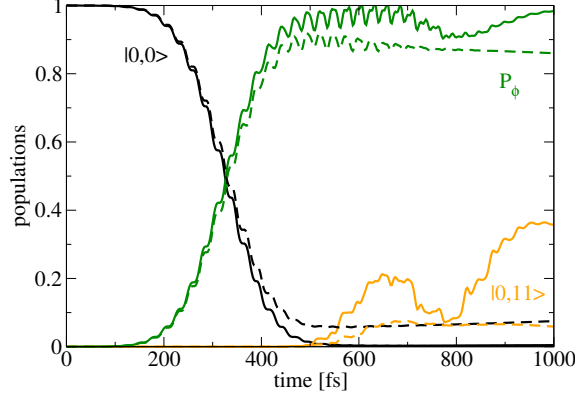


Figure 4.18: Excitation of state $|n_r = 0, n_\phi = 11\rangle$ by a single, “hand-optimized” \sin^2 -shaped pulse of duration 1.0 ps and parameters $F_0 = 0.008707 E_h/ea_0$ and $\omega = 642.3 \text{ cm}^{-1}$: Dynamics for the system in non-Markovian description, for which the pulse was optimized, in solid lines and in dashed lines the dynamics it induces when applied within the Markov approximation. P_ϕ is $P_\phi = \sum_{n_\phi > 1} P_{(0, n_\phi)}$.

fluences/intensities. In case of the ϕ mode of the system H/Si(100) this might be of interest in order to induce lateral motion of the adsorbate (that is H-diffusion). In the example for such a high-energy excitation given in Fig. 4.18 the goal is to populate state $|0, 11\rangle$. Again, in Ref. [104] a pulse was “hand-optimized” for this purpose for the non-Markovian case (solid lines) and $t_f = 1.0$ ps. The other optimized parameters are $F_0 = 0.008707 E_h/ea_0$ and $\omega = 642.3 \text{ cm}^{-1}$. One thus achieves a population of 0.3576 for state $|0, 11\rangle$ at $(t = t_f)$. Further, after the pulse is off, ϕ -excited states $|0, n_\phi\rangle$ with $(n_\phi = 1, 2, \dots)$ are in total populated by $P_\phi(t_f) = 0.9844$. ϕ -selectivity $S_\phi(t_f)$, defined as

$$S_\phi(t_f) = \frac{P_\phi(t_f)}{P_{ex}(t_f)} \quad \text{with } P_{ex}(t_f) = 1 - P_{(0,0)}(t_f) \quad , \quad (4.6)$$

with P_{ex} being the excitation probability, reaches a large value of 0.989. A different picture is obtained if the same pulse is applied within the Markovian approximation (dashed lines): For the first 200–300 fs when only the lower-lying ϕ states are populated, the differences are still small, but later on both the amount of population transferred to the desired state $|0, 11\rangle$ as well as to other higher-excited ϕ states is considerably smaller. Also the course of population of state $|0, 11\rangle$ (and other states not shown) differs: Instead of the “two-step population” in the non-Markov picture, a “single-step population” followed by a “plateau” is observed in the Markov picture. The selectivity $S_\phi(t_f)$ is still rather large with 0.930 – the “lost” population mainly remains in /decays back to the ground state. Again as discussed for the

cases shown in Fig. 4.16, a slightly different functional behaviour of populations accumulates. One can conclude, that the Markov approximation is good for low-energetic excitations, few-step processes and weak dissipation.

Excitation of a “mixed” state in r and ϕ

Finally, also the excitation of a combination mode in (r, ϕ) is attempted, using a two-pulse strategy, that is

$$F_z(t) = \begin{cases} F_{0,1} \sin^2\left(\frac{\pi t}{t_{f,1}}\right) \sin(\omega_1 t + \phi_1) & \text{for } t \in [0, t_{f,1}] \\ F_{0,2} \sin^2\left(\frac{\pi(t+t_{f,1})}{t_{f,2}}\right) \sin(\omega_2(t+t_{f,1}) + \phi_2) & \text{for } t \in [t_{f,1}, (t_{f,1} + t_{f,2})] \end{cases} \quad (4.7)$$

Shown in Fig. 4.19 are pulse (upper panel) and population dynamics (lower panel) ob-

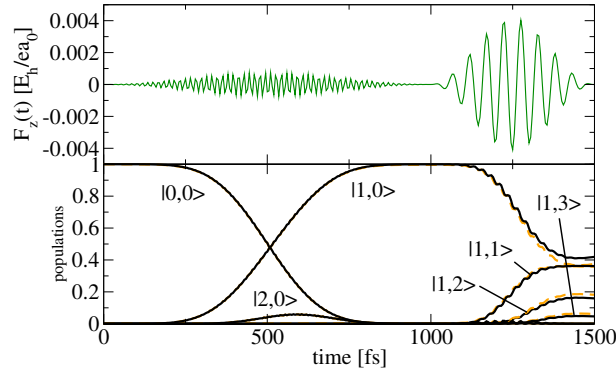


Figure 4.19: Excitation of the state $|n_r = 1, n_\phi = 1\rangle$ at $(T = 4 \text{ K})$ by a two-pulse strategy using a field (upper panel) of type (4.7) with “hand-optimized” parameters for maximum field strengths and frequencies: Shown in the lower panel in black solid lines is the non-Markovian dynamics the field was optimized for as well as state populations (dashed orange) obtained within the Markov approximation if the same field is applied.

tained by “hand-optimization” within the non-Markov picture (solid lines) and with the goal to populate state $|1, 1\rangle$ maximally. The parameters are: $t_{f,1} = 1.0 \text{ ps}$, $t_{f,2} = 0.5 \text{ ps}$, $F_{0,1} = 0.0007517 E_h/ea_0$, $F_{0,2} = 0.004121 E_h/ea_0$, $\omega_1 = 2042 \text{ cm}^{-1}$ ($\omega_r = 2037 \text{ cm}^{-1}$), $\omega_2 = 636.3 \text{ cm}^{-1}$ ($\omega_\phi = 637.0 \text{ cm}^{-1}$) and $\phi_1 = \phi_2 = 0$. Thereby, pulse durations as well as phase shifts were kept fixed, only the other parameters were optimized in Ref. [104]. The first transition in r $|0, 0\rangle \rightarrow |1, 0\rangle$ constitutes a basically complete population inversion within the first 1 ps pulse, although there is some transient excitation of $|2, 0\rangle$, the overtone in r .

There is only a small difference between the non-Markovian model (solid black lines) and the Markovian one (dashed orange lines) – dissipation is small, that is, the “memory effect” is small. This is different for the following 500 fs where state $|1, 1\rangle$ becomes populated by 0.3615 (non-Markovian dynamics) and by 0.3586 (Markovian dynamics), respectively, and where also higher combination mode states $|1, n_\phi \geq 2\rangle$ receive considerable amounts of population. Again, the “memory effect”, neglected by the Markovian picture, plays a larger role when dissipation is stronger.

In summary, it was possible to selectively excite r and ϕ modes in the two-dimensional model of H/Si(100). Thereby, state selectivity is successful in case of r , whereas the harmonic potential term along ϕ allows only for mode-selectiveness for this mode. Non-Markovian effects were shown to be negligible when dissipation is small and the excitation mechanism involves only few intermediate steps. A different functional behaviour of population dynamics was observed for Markovian and non-Markovian models for the limits ($t \rightarrow 0$) and ($t \rightarrow \infty$).

4.3 2H/Ru(0001) [111]

In the following, the results for the IR-excitation of the two-dimensional (r, Z) model of 2H/Ru(0001) (Sec. 3.3) are reviewed.

The 2D system 2H/Ru(0001) poses several “problems” for selective vibrational excitation:

- There are short (sub-picosecond) vibrational lifetimes for both modes (compare also Sec. 3.3.2), making short and thus high-fluence pulses necessary.
- There is only weak (r) and medium (Z) IR activity (see Table 3.11), a further factor demanding for larger intensities/fluences.
- Both modes are very harmonic (see the eigenenergies of the lowest 10 states in Table 3.11).
- The inter-mode dipole coupling is comparatively strong, with dipole transition moments of the same order of magnitude as that for single-photon transitions in the r mode. Thus, it is likely that a certain amount of “pure” Z mode states as well as (r, Z)

combination mode states are populated if “pure” r states are to be excited, and vice versa.

For these reasons state-selective IR excitation is difficult/impossible and the aim in the following is a high mode-selectivity. The latter is neither granted as the resonance frequencies are rather similar ($\omega_r = 760 \text{ cm}^{-1}$ and $\omega_Z = 1095 \text{ cm}^{-1}$) and the short, high-intensity/-fluence pulses needed might cause a broad energy spectrum by which both modes can be reached.

In the following calculations, the 20 lowest eigenstates in the 2D model of 2H/Ru(0001) are used for density matrix propagation. The field optimization is done by global OCT at ($T = 0 \text{ K}$). For the fundamental relaxation rate, vibrational lifetimes of $\tau_r = \tau_Z = 500 \text{ fs}$ have been chosen, as outlined above.

4.3.1 Excitation of the Z mode

Starting with a \sin^2 -shaped π pulse of duration $t_f = 300$ ($I^{max} = 2.4 \cdot 10^{12} \text{ W/cm}^2$, $f = 274 \text{ mJ/cm}^2$) adjusted to $|0, 0\rangle \rightarrow |0, 1\rangle$, the fundamental transition in Z , one obtains (upper panel of Fig. 4.20 (a)), as typical for a very harmonic mode, a distribution of population in the lowest states $|0, n_Z\rangle$. Thereby,

$$P_{(0,1)}(t_f) > P_{(0,2)}(t_f) > P_{(0,3)}(t_f) > P_{(0,4)}(t_f) \quad (4.8)$$

(see Table 4.2) and the initial state $|0, 0\rangle$ remains still strongly populated by 0.242. The Z -selectivity

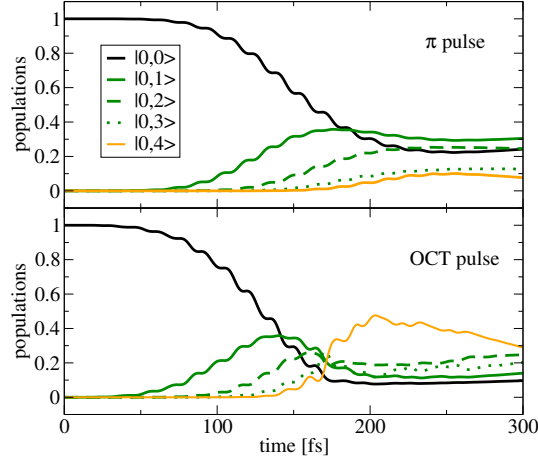
$$S_Z(t_f) = \frac{P_Z(t_f)}{P_Z(t_f) + P_r(t_f) + P_{combi}(t_f)} = 0.995 \quad (4.9)$$

is very high, as “pure” states in r and combination mode state $|n_r > 0, n_Z > 0\rangle$ become only weakly populated, by ~ 0.002 in both cases. Here, $P_Z(t_f)$ is the population of Z -excited states, $P_r(t_f)$ that of r -excited states and $P_{combi}(t_f)$ that of (r, Z) combination states at ($t = t_f$), as defined in the caption of Table 4.2. The denominator in Eq. (4.9) thus defines the total excitation probability $P_{ex}(t_f)$.

With the goal to invert the relation of populations in (4.8) and thus increase the level of excitation, an optimal control pulse with target operator

$$\hat{O} = 0.01 |0, 1\rangle\langle 0, 1| + 0.05 |0, 2\rangle\langle 0, 2| + 0.19 |0, 3\rangle\langle 0, 3| + 0.75 |0, 4\rangle\langle 0, 4| \quad (4.10)$$

(a)



(b)

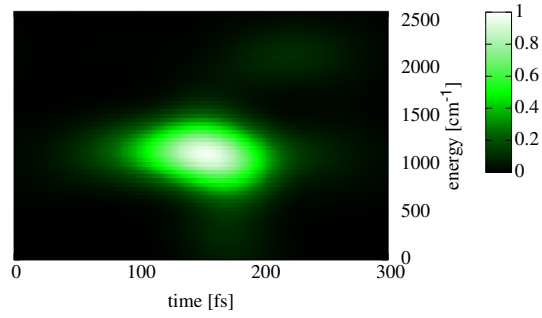


Figure 4.20: Excitation of the Z mode at ($T = 0$ K): (a) Dynamics for a π pulse (upper panel) adjusted to the fundamental transition $|n_r = 0, n_Z = 0\rangle \rightarrow |n_r = 0, n_Z = 1\rangle$ and the optimal control pulse (lower panel) described in the text; (b) Husimi plot of the OCT pulse.

is set up to enforce

$$P_{(0,1)}(t_f) < P_{(0,2)}(t_f) < P_{(0,3)}(t_f) < P_{(0,4)}(t_f) \quad . \quad (4.11)$$

And indeed, as the result for the dynamics in the lower panel of Fig. 4.20 (a) and the explicit (sums of) final populations in Table 4.2 show, this is possible to a large extent (with the exception of $P_{(0,2)}(t_f) > P_{(0,3)}(t_f)$). Further, the OCT pulse achieves a more complete depopulation of the ground state ($P_{(0,0)}(t_f) = 0.097$) and a higher total excitation of the Z -mode with $P_r(t_f) = 0.879$ (being 0.753 for the π pulse), increasing the amount of energy transferred into the Z mode from 0.20 to 0.32 eV. But the Z -selectivity drops by about 2%,

$t = t_f$ pulse	$P_{(0,1)}$	$P_{(0,2)}$	$P_{(0,3)}$	$P_{(0,4)}$	P_Z	P_r	P_{combi}	S_Z
π	0.305	0.245	0.126	0.077	0.753	0.002	0.002	0.995
OCT	0.140	0.247	0.203	0.290	0.879	0.010	0.014	0.973

Table 4.2: Comparison of π pulse (Fig. 4.20 (a), upper panel) and OCT pulse (Fig. 4.20 (a), lower panel): Final populations $P_{(0,n_Z)}(t_f)$, sums of excited populations in Z , r and (r,Z) combination mode states, $P_Z(t_f) = \sum_{n_Z=1}^4 P_{(0,n_Z)}(t_f)$, $P_r(t_f) = \sum_{n_r=1}^6 P_{(n_r,0)}(t_f)$, $P_{combi} = \sum_{n_r \geq 1, n_Z \geq 1} P_{(n_r, n_Z)}(t_f)$. Listed further are the Z -selectivities $S_Z(t_f)$ as defined in Eq. (4.9).

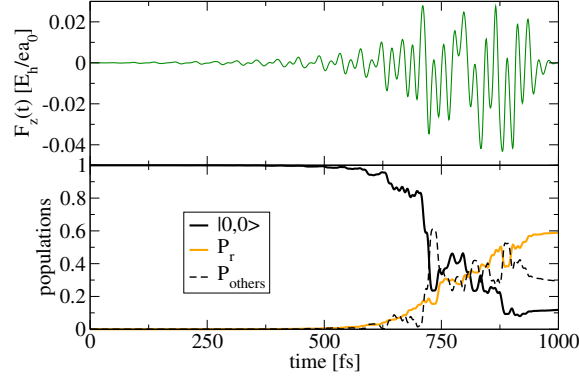
as “pure” r states as well as combination mode states are more strongly populated by this high-fluence OCT pulse ($f = 941 \text{ mJ/cm}^2$).

The Husimi transformation of the OCT pulse (Fig. 4.20 (b)) reveals a dominating, downward-”chirped” signal, as typical for a “ladder climbing” mechanism, centered around the resonance energy for $(n_Z \rightarrow n_Z + 1)$ transitions ($\sim 1000 - 1100 \text{ cm}^{-1}$). During the last 100 fs, where the main population transfer into state $(0,4)$ occurs, there is also a weaker signal at overtone-excitation energies ($\sim 2200 \text{ cm}^{-1}$). Thus, a rough description of the excitation mechanism is, that during the first 200 fs mainly one-photon “ladder climbing” $|0,0\rangle \rightarrow |0,1\rangle \rightarrow |0,2\rangle \rightarrow |0,3\rangle$ takes place, while in a last, shorter step the two-photon transition $|0,2\rangle \rightarrow |0,4\rangle$ occurs. This mechanism is well suited to somewhat inhibit the fast dissipative loss of state $|0,4\rangle$. In this light, the “surplus” of final population in state $|0,2\rangle$ can be understood: Although $|0,2\rangle$ “feeds” the excitation of state $|0,4\rangle$ it receives again population from state $|0,3\rangle$ which becomes excited early, but nevertheless decays with a rate of $(167 \text{ fs})^{-1}$ to $|0,2\rangle$, while state $|0,2\rangle$ has a lifetime almost as long (250 fs) as the whole pulse duration.

4.3.2 Excitation of the r mode

In analogy to the OCT pulse above to excite the Z mode, the objective of this sub-section is to transfer a maximal amount of energy into the (weakly dipole active) r mode. Several target operators were chosen, but it is found that the best result is obtained for targets making advantage of the fact that $\mu_{(n_r,0)(n_r+2,0)} \approx 2\mu_{(n_r,0)(n_r+1,0)}$ (compare Table 3.11). For

(a)



(b)

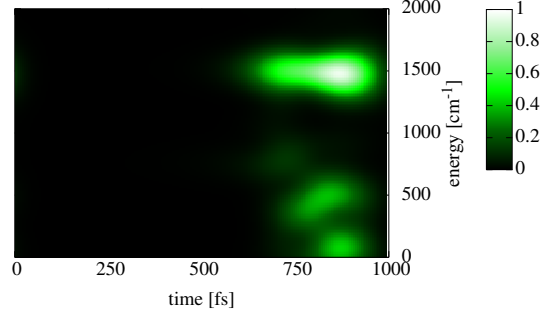


Figure 4.21: Excitation of the r mode at ($T = 0$ K): (a) Population dynamics, where $P_r(t) = \sum_{n_r=1}^6 P_{(n_r,0)}(t)$ and $P_{others}(t) = \sum_{n_r, n_z \geq 1} P_{(n_r, n_z)}(t)$, and (b) Husimi plot of the OCT pulse.

the example presented in Fig. 4.21, a target operator

$$\hat{O} = 0.08 |2, 0\rangle\langle 2, 0| + 0.23 |4, 0\rangle\langle 4, 0| + 0.69 |6, 0\rangle\langle 6, 0| \quad (4.12)$$

and a control time of 1 ps was chosen. Shown in the upper panel of Fig. 4.21 (a) is the control field ($I^{max} = 6.6 \cdot 10^{13} \text{ W/cm}^2$, $f = 7122 \text{ mJ/cm}^2$) obtained when applying a penalty function of type (4.2) with $\alpha = 0.02$. The mechanism is rather complex. By no means only the “intended” mechanism $|0, 0\rangle \rightarrow |2, 0\rangle \rightarrow |4, 0\rangle \rightarrow |6, 0\rangle$ takes place, but also transitions between states of uneven quantum numbers n_r . Therefore, only the sum $P_r(t)$ of all “pure” states in r is plotted in the lower panel of Fig. 4.21 (a). Pure r mode states $|n_r, 0\rangle$ are populated by 0.59 at final time t_f , being an improvement when comparing this to the according values of $P_r(t_f) = 0.39/0.43$ if one uses π pulses adjusted to transitions $|0, 0\rangle \rightarrow |1, 0\rangle / |0, 0\rangle \rightarrow |2, 0\rangle$ with frequencies $\omega = 760/1518 \text{ cm}^{-1}$ and fluences $f = 6397/1635 \text{ mJ/cm}^2$ – latter used as

initial field for optimization here. As expected, there is some coupling to pure Z states ($P_Z(t_f) = 0.09$) and, more strongly, to (r, Z) combination mode state ($P_{combi}(t_f) = 0.21$). The pulse itself is “late” as to avoid dissipation and its main frequency component (Husimi plot in Fig. 4.21 (b)) is that of $(n_r \rightarrow n_r + 2)$ transitions around frequencies of 1500 cm^{-1} . The signal has a downward-chirp for “ladder climbing”. There is no contribution observable which would suggest one-photon transitions, but there are weaker contributions at frequencies $< 600 \text{ cm}^{-1}$ which cannot be assigned to any transition(s). It is possible that some sort of dressed state is formed similar to STIRAP [124, 125] and in analogy to the observation of a static field component made in Sec. 4.1.4 when calculating an optimal pulse to excite the θ mode of CO/Cu(100). Generally speaking, the r -excitation is indeed very difficult and requires prohibitively large fluences.

In case of the 2D (r, Z) model of 2H/Ru(0001) state selective excitation was not possible due to the harmonicity of both modes and, particularly in case of r , the need for high-intensity pulses with broad energy widths. However, it was shown that via OCT it is possible to “invert” the population distribution in Z as achieved by a π pulse and, thereby, transfer a large amount of energy targeted into this mode.

Chapter 5

Optimal control with time-dependent targets

The problem common to both the global optimal control theory algorithm (Sec. 2.4.2), as used in the previously presented density matrix calculations, as well as the variant of local control theory (Sec. 2.4.2) which served to study the simple non-dissipative scenario (Appendix H) is the lack of a *time-dependent* target operator. The iterative scheme of global control allows only to specify the desired system at ($t = t_f$), whereas local control, based on a single forward propagation, even lacks this second boundary condition. However, to some extent, compare the second example in Appendix H, the weight (“target”) factors o_{ii} which enter the equation (2.45) for the control field can influence the dynamics, although in a very non-systematic way. In condensed phase environments [9] and/or for quantum computing [31, 32] the selective preparation of a state at t_f may not be useful (it subsequently decays), but one may be interested in preserving target state populations and/or coherences over a longer period of time.

Optimal control or related algorithms with time-dependent targets are still rare (particularly in the density matrix formulation); the most important examples from the literature are listed in the following:

- Optimal control of time-averaged quantities by controlling the pulse envelope in a dissipative two-level system was used in Ref. [130].

- The optimization of the pump-probe signal in a non-dissipative three-level system was performed in Ref. [131].
- A combination of optimal and coherent control theories for a non-dissipative three-level system was applied in Ref. [132].
- The “adaptive tracking method” and locally designed coherent control theory for dissipative and non-dissipative systems were formulated in Ref. [133,134].
- A global OCT for non-dissipative systems was used in Ref. [135].
- A generalization of global OCT to time-dependent targets was suggested, and applied to dissipative and non-dissipative four-level test systems in Ref. [33].

The first two methods do not contain an explicitly time-dependent “target”. The third method is no optimal control theory in the common sense, as it is based on coherent control theory and results in analytical expressions for the control field. Unlike the first two methods the fourth does contain a time-dependent target, that is, the control field directly depends on a time-dependent trajectory – the so-called “performance index”. The disadvantage, however, is that instabilities may occur through singularities which have to be corrected for [133]. The last two algorithms are global, insofar as they are based on an iterative forward-backward propagation plus optimization scheme. The former of the two algorithms, however, is set up in the non-dissipative wavepacket frame only. The disadvantage of the latter is that it is formulated in the rotating-wave approximation, requires two further parameters guaranteeing the monotonic convergence and has only been tested on small systems so far. In what follows a new algorithm is presented which does not have the disadvantages just mentioned.

5.1 Algorithm

The algorithm formulated in the present work is a simple model based on the monotonically and quadratically convergent, iterative global OCT algorithm as formulated by Ohtsuki *et al.* for dissipative systems [30] which often gives very good target yields (compare Sec.4) and combines it with the local, non-iterative control scheme which exhibits computational efficiency and applicability to strong-field situations. Therefore, the total control interval $[0, t_f]$ is subdivided into M intervals $[t_0^{(n)}, t_f^{(n)}]$ and in the n th sub-interval a global optimization

scheme is applied to drive the density operator from $\hat{\rho}(t_0^{(n)})$ to $\hat{\rho}(t_f^{(n)})$ with the goal to optimize the predefined, time-dependent operators $\hat{O}(t_0^{(n)})$ and $\hat{O}(t_f^{(n)})$ at beginning and end of the sub-interval, respectively.

For the ‘‘conventional’’ global optimal control algorithm (compare Sec. 2.4.2) a solution algorithm for the coupled equations (2.13), (2.49), and (2.50) was proposed in Ref. [30]:

$$\text{step 0: } i\hbar \frac{\partial \hat{\sigma}^{(0)}(t)}{\partial t} = (\mathcal{L}_H(\varepsilon_0) + \mathcal{L}_D)^\dagger \hat{\sigma}^{(0)}(t) \quad (5.1)$$

$$\text{step } k > 0: \quad i\hbar \frac{\partial \hat{\rho}^{(k)}(t)}{\partial t} = (\mathcal{L}_H(F^{(k)}) + \mathcal{L}_D) \hat{\rho}^{(k)}(t) \quad (5.2)$$

$$i\hbar \frac{\partial \hat{\sigma}^{(k)}(t)}{\partial t} = (\mathcal{L}_H(\bar{F}^{(k)}) + \mathcal{L}_D)^\dagger \hat{\sigma}^{(k)}(t) \quad (5.3)$$

where the arguments in brackets of \mathcal{L}_H denote on which field the Liouvillian depends. Here, ε_0 is a trial field, and

$$F^{(k)} = -\frac{1}{\hbar\alpha} \text{Im} \left\langle \left\langle \hat{\sigma}^{(k-1)}(t) | \hat{\mu} | \hat{\rho}^{(k)}(t) \right\rangle \right\rangle \quad (5.4)$$

$$\bar{F}^{(k)} = -\frac{1}{\hbar\alpha} \text{Im} \left\langle \left\langle \hat{\sigma}^{(k)}(t) | \hat{\mu} | \hat{\rho}^{(k)}(t) \right\rangle \right\rangle \quad (5.5)$$

are the fields for forward and backward propagation in iteration k . To extend this formalism to time-dependent targets the above control equations (2.13), (2.49) and (2.50) are solved now iteratively, in every interval $[t_0^{(n)}, t_f^{(n)}]$, using the algorithm with forward-backward propagation of above. In the n -th interval, for the density operator $\hat{\rho}(t)$ and the Lagrange density $\hat{\sigma}(t)$, the respective initial conditions are:

$$\hat{\rho}(t_0^{(n)}) = \hat{\rho}(t_f^{(n-1)}) \quad \text{forward propagation} \quad (5.6)$$

$$\hat{\sigma}(t_f^{(n)}) = \hat{O}(t_f^{(n)}) \quad \text{backward propagation} \quad , \quad (5.7)$$

i. e. for $\hat{\rho}(t)$ the final density of the $(n-1)$ th interval serves as initial condition for the n th interval, and $\hat{O}(t_f^{(n)})$ is the initial condition for backward propagation of $\hat{\sigma}(t)$ in that interval. If the individual time slices are chosen narrow enough, a continuous time-dependent target can be modelled. If there is only one time slice over the entire control time, the conventional optimal control algorithm [30] is regained. Within every sub-interval, the initial guess field for the first propagation, $\varepsilon_0^{(n)}$, is set to zero to avoid any dependence of the final control field on the initial one. By this procedure discontinuities in $F(t)$ between two intervals are avoided, even when the Lagrange multiplier density $\hat{\sigma}(t)$ becomes discontinuous. The latter can happen in case of long sub-intervals, because backward propagation always starts with the value of \hat{O} at $t_f^{(n)}$. Then the envelope of the obtained optimal pulse is no longer smooth

(not shown for brevity). The global nature of control as well as the convergence behaviour of the algorithm in Ref. [30], are strictly fulfilled only within a sub-interval $[t_0^{(n)}, t_f^{(n)}]$, while individual intervals are *locally coupled* in time. The objective functional J for the total control time $[0, t_f]$ is a sum

$$J = \sum_{n=1}^M J_n \quad , \quad (5.8)$$

where J_n is identical with the right side of Eq. (2.47) when substituting $[t_0^{(n)}, t_f^{(n)}]$ for $[0, t_f]$.

In the eigenstate representation used here both densities $\hat{\rho}(t)$ and $\hat{\sigma}(t)$ and the target $\hat{O}(t)$ are of matrix form, *e.g.*

$$\hat{O}(t) = \sum_{i=1, j=1}^L |i\rangle o_{ij}(t) \langle j| \quad . \quad (5.9)$$

The matrix elements $o_{ij}(t)$ are given as analytical functions of time in the calculations presented in the following.

As test system a one-dimensional model of the Z mode of CO/Cu(100) at ($T = 10$ K) is used which is “extracted” from the three-dimensional model (compare Sec. 3.1.1) by choosing from states $|n_r, n_Z, n_X\rangle$, states $|0, n_Z, 0\rangle$ only.

5.2 Numerical tests

In order to study the algorithm’s numerical performance, a two-level model with $|n_Z = 0\rangle \equiv |0\rangle$ and $|n_Z = 1\rangle \equiv |1\rangle$ is used, in which a population inversion $|0\rangle \rightarrow |1\rangle$ is to take place within a control time $t_f = 5500$ fs ($= \frac{\tau_1 \rightarrow 0}{4}$). The time-dependent diagonal (real) target matrix elements $o_{ii}(t)$ (“populations”) are chosen here as

$$o_{00}(t) = \frac{C_0}{N(t) e^{-\frac{(t-a_0)^2}{2\sigma_0^2}}} \quad (5.10)$$

$$o_{11}(t) = \frac{C_1}{N(t) e^{-\frac{(t-a_1)^2}{2\sigma_1^2}}} \quad , \quad (5.11)$$

with $C_0 = C_1 = 1$, $\sigma_0 = \sigma_1 = 1375$ fs and the normalisation $N(t) = o_{00}(t) + o_{11}(t)$ ensuring that $\text{Tr}\{\underline{O}\} = 1$. We further take $a_0 = 0$ and $t_f = a_1 = 5500$ fs. Further, $N(t)$ causes the

population target matrix elements $o_{00}(t)$ and $o_{11}(t)$ to resemble a smoothed step function – see the dashed lines labeled 00 and 11 in the lower panel of Fig. 5.1. Inherent to the algorithm (which starts each sub-interval optimization by a backward propagation beginning with the according $\hat{O}^{(n)}(t_f^{(n)})$), an analytic function for at least one off-diagonal element $o_{ij}(t) = o_{ji}^*(t)$ is required which has to oscillate in the complex plane with a frequency ω_{ij} (chosen as the/a resonance frequency of the desired state, for example). Omitting an oscillatory part in the off-diagonal target matrix elements (“coherences”), one also obtains a non-oscillatory control field. Chosen here is

$$o_{01}(t) = |o_{01}(t)|e^{i\omega_{01}t} \quad , \quad (5.12)$$

where $-\omega_{01} = \omega_{10} = 293 \text{ cm}^{-1}$ and the coherence “envelope” $|o_{01}(t)|$ is chosen of Gaussian form, centered at $\frac{t_f}{2} = a_{01} = 2750 \text{ fs}$

$$|o_{01}(t)| = C_{01}e^{-\frac{(t-a_{01})^2}{2\sigma_{01}^2}} \quad , \quad (5.13)$$

where $C_{01} = 0.5$ and $\sigma_{01} = 786 \text{ fs}$, see Fig. 5.1. The parameters in both cases are chosen deliberately such that the shape of density matrix elements o_{ij} resembles that for a dissipation-free two-level system upon which a typical π pulse, centered at $(t = \frac{t_f}{2})$ is applied. For the cal-

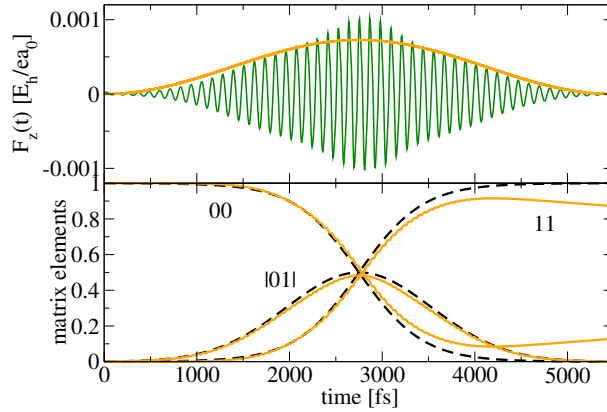


Figure 5.1: Optimal field (upper panel) and dynamics of ρ_{00} , ρ_{11} , $|\rho_{01}| = |\rho_{10}|$ (lower panel, solid orange lines) as obtained for the time-dependent target of Eqs. (5.10), (5.11), (5.12) and (5.13), $M = (N - 1) = 100\,000$ (one time step per sub-interval) and $\alpha = 1 \neq f(t)$; the time-dependent target elements o_{00} , o_{11} , $|o_{01}| = |o_{10}|$ are plotted as dashed lines in the lower panel. Given for comparison in the upper panel is $s(t)$, the (\sin^2) shape function of a π pulse obeying $|\mu_{01}|F_0 \int_0^{t_f} s(t)dt = \hbar\pi$ for the present target time t_f .

ulation presented in Fig. 5.1, with the solid lines representing the actually obtained density

matrix elements, ($N = 100\,001$) timesteps and ($M = 100\,000$) sub-intervals are used, *i. e.* each sub-interval contains only a single timestep, further a time-independent penalty $\alpha = 1$ is chosen. It is seen that target (dashed) and density (solid) matrix elements agree generally quite well, only towards the end of the pulse there are deviations in the populations of a bit more than 10%. This is due to dissipation. For the coherence term the agreement is even better, with the maximum deviation being less than 2% at ($t = \frac{t_f}{2}$). In order to have a global measure for the success of a time-dependent optimal control calculation, an achievement factor A is defined as

$$A = \frac{1}{t_f} \int_0^{t_f} A(t) dt = \frac{1}{t_f} \int_0^{t_f} \langle \langle \hat{O}(t) | \hat{\rho}(t) \rangle \rangle dt \quad (5.14)$$

which is ideally 1 if $\hat{\rho}(t) = \hat{O}(t)$. In the example of Fig. 5.1, it is 0.9701. The control field (upper panel of Fig. 5.1) is centered at ($t = \frac{t_f}{2}$) and resembles a π pulse (the shape of a $\sin^2 \pi$ pulse is shown in orange). Only around ($t = \frac{t_f}{2}$) the control field is more intense than the π pulse. The control field for which $|\mu_{01}| F_0 \int_0^{t_f} s(t) dt = 1.049 \hbar \pi$ (the fluence, 48 mJ/cm², being 5% larger than that of the π pulse) is able to populate the target state 1 by $\rho_{11}(t_f) = 0.882$, while with the π pulse one gets $\rho_{11}(t_f) = 0.871$. This is a proof of the reliability of the conventional OCT algorithm upon which the algorithm is based.

After having shown that the algorithm can control time-dependent targets, the question now is how accuracy and computational cost of the algorithm depend on N_i

$$N_i = \frac{N - 1}{M} \quad , \quad (5.15)$$

the number of timesteps per sub-interval. The example of Fig. 5.1 is taken and a convergence threshold $\delta J_n^{(k,k-1)}$ for $J_n^{(k)}$, the objective functional in iteration k of sub-interval n , is defined as

$$\delta J_n^{(k,k-1)} = |J_n^{(k)} - J_n^{(k-1)}| \quad . \quad (5.16)$$

Further, in order to compare calculations with different numbers of sub-intervals M , a constant number of timesteps ($N = 100\,001$) is chosen and a common, total threshold of

$$\delta J = M J_n^{(k,k-1)} = 10^{-12} \quad (5.17)$$

is fixed, while N_i is varied in the calculations summarized in Table 5.1.

The first thing one notes is that for the case when ($N_i = 1$) the best accuracy and computational performance is achieved. Thus, even with A being not 1, this is chosen as reference

M	N_i	$\delta J_n^{(k,k-1)}$	I_{av}	A	$A(t_f)$	E_{rel}	CPU time [s]
10^5	1	10^{-17}	1.94	0.970 10	0.884 02	0	16
10^4	10	10^{-16}	3.75	0.970 10	0.884 03	$3.423 \cdot 10^{-6}$	18
10^3	10^2	10^{-15}	5.30	0.970 07	0.884 07	$3.689 \cdot 10^{-5}$	20
10^2	10^3	10^{-14}	17.6	0.969 51	0.883 95	$6.064 \cdot 10^{-4}$	30
10	10^4	10^{-13}	496	0.964 02	0.884 00	$6.274 \cdot 10^{-3}$	455
1	10^5	10^{-12}	18 300	0.884 20	0.884 20	$8.855 \cdot 10^{-2}$	16 334

Table 5.1: Performance test for the two-level system: M , the number of sub-intervals, and $\delta J_n^{(k,k-1)}$ of Eq. (5.16), the convergence threshold in each sub-interval n . I_{av} is the average number of backward-forward iterations per sub-interval, A and $A(t_f)$ are the total and final time achievements, respectively, see Eq. (5.14). Taking the achievement factor for N_i as reference (A_{ref}), the relative error is $E_{rel} = \frac{A_{ref} - A}{A_{ref}}$. The CPU time is given for a AMD Opteron™ Processor 246.

value. The larger N_i here, the less accurate the calculations become. For ($N_i = 10^5$) and ($M = 1$), where the algorithm is equivalent to the ordinary global OCT, the error E_{rel} relative to the reference case as defined in the caption of Fig. 5.1 is almost 1 %, as the conventional algorithm is not made for time-dependent targets. The *final* achievement $A(t_f)$ remains almost constant independent of N_i . This is another proof of reliability for the conventional algorithm contained in the new hybrid algorithm. Further, the average number of forward-backward iterations per interval n to meet the respective convergence criterion $\delta J_n^{(k,k-1)}$ grows fast for increasing N_i , although, due to N and δJ being held fixed, the convergence threshold $\delta J_n^{(k,k-1)}$ decreases. In summary, time-dependent control with the present algorithm is most efficient and accurate with sub-intervals equivalent to the timestep of density matrix propagation. Then also the “smoothness” of the (envelopes of) Lagrange multiplier matrix elements $\sigma_{ii}(t)$ ($\sigma_{ij}(t)$) is guaranteed. In each sub-interval $\hat{\sigma}(t)$ has to obey the boundary condition of Eq. (5.7) so that only if the sub-intervals are small enough smoothness is reached; a lacking smoothness of the Lagrange multiplier density matrix, particularly in the envelopes of the coherence terms, leads also to a pulse envelope being “non-smooth”.

5.3 Applications

5.3.1 Creation and preservation of a wavepacket

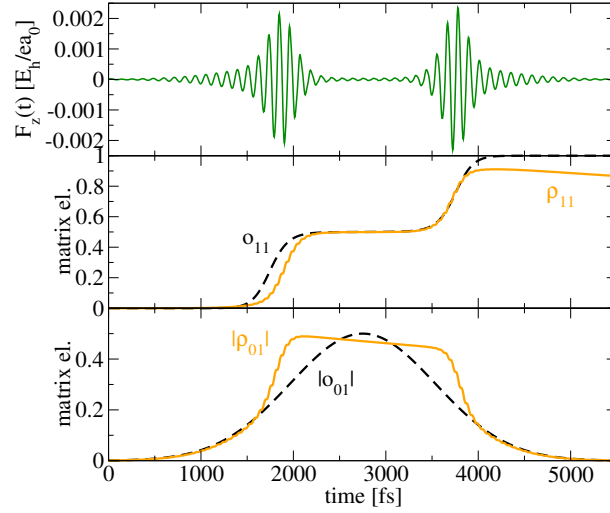


Figure 5.2: Creation – stabilization – destruction of a wavepacket in the two-level system at ($T = 10$ K): The control field (upper panel) obtained by a target matrix $\underline{Q}(t)$ consisting of elements as given in Eqs. (5.21), (5.21), (5.12) and (5.13). Shown in the middle panel are $o_{11}(t)$ (dashed) and the obtained $\rho_{11}(t)$ (solid orange); plotted in the lower panel are $|o_{01}(t)| = |o_{10}(t)|$ (dashed) and $|\rho_{01}(t)| = |\rho_{10}(t)|$ (solid orange).

One of the main reasons, why optimal control with time-dependent-target is so interesting, is the possibility to control populations and/or coherences during the control time. This is a feature needed, for example, in the following application of the present algorithm, where

- first a wavepacket $|\psi(t)\rangle$ is created from the ground state $|0\rangle$,

$$|\psi(t)\rangle = \frac{1}{\sqrt{2}} (|0\rangle + e^{-i\omega_{10}t}|1\rangle) \quad (5.18)$$

as a linear combination of states $|0\rangle$ and $|1\rangle$ within the two-level system;

- then the wavepacket is stabilized for a while, despite dissipation, such that (except for phase factors) one ideally has

$$\underline{\rho}(t) = \frac{1}{2} \begin{pmatrix} 1 & 1 \\ 1 & 1 \end{pmatrix} ; \quad (5.19)$$

- finally, the whole population is transferred to state $|1\rangle$.

Such a scenario would be useful, for example, in quantum computing using vibrational states to set up “qubits” to switch a linear combination of states constituting a qubit “on” and “off”. The target populations $o_{00}(t)$ and $o_{11}(t)$ are set up as to create a “plateau” region centered at $\frac{t_f}{2} = 2750 \text{ fs} = a'_0 = a'_1$

$$o_{00}(t) = \frac{1}{N(t)} \left[C_0 e^{\frac{(t-a_0)^2}{2\sigma_0^2}} + C'_0 e^{\frac{(t-a'_0)^2}{2\sigma_0'^2}} \right] \quad (5.20)$$

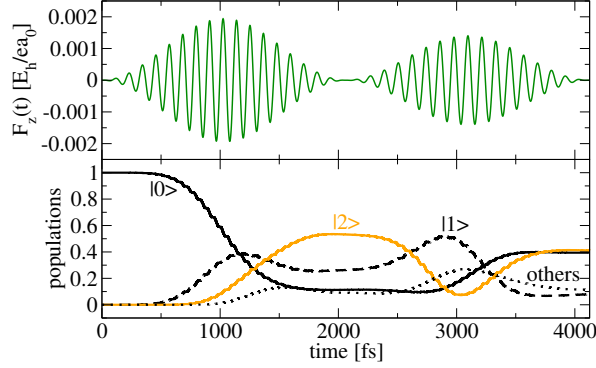
$$o_{11}(t) = \frac{1}{N(t)} \left[C_1 e^{\frac{(t-a_1)^2}{2\sigma_1^2}} + C'_1 e^{\frac{(t-a'_1)^2}{2\sigma_1'^2}} \right] . \quad (5.21)$$

The other parameters are $C_0 = C_1 = 1$, $C'_0 = C'_1 = 0.5$, $a_0 = a_1 = 0$, $\sigma_0 = \sigma_1 = 687.5 \text{ fs}$ and $\sigma'_0 = \sigma'_1 = 392.9 \text{ fs}$. $N(t) = o_{00}(t) + o_{11}(t)$ is again the norm-preserving factor. Further a time-independent penalty factor $\alpha = 1$ is used. The target element $o_{11}(t)$ is shown in dashed in the middle panel of Fig. 5.2. It is not absolutely clear how the envelope $|o_{ij}(t)| = |o_{ji}(t)|$ of the coherence terms might look like, so the same, simple form of Eqs. (5.12) and (5.13) is chosen (Fig. 5.2, lower panel, dashed line).

The target populations are well reached by the optimal pulse, as demonstrated in Fig. 5.2. There is only a small deviation when the “plateau” region starts and towards the end when dissipation inhibits a complete population transfer, but it is ($P_0 = P_1 = 0.5$) during the whole ca. 1500 fs where the corresponding target matrix elements take on this value. And, indeed, such a population stabilization is feasible for long times with the present algorithm, up and above times of 22 ps, being the lifetime of state $|1\rangle$. The envelope of coherence terms deviates more strongly, as the optimal control algorithm enforces a “plateau” region for $|\rho_{01}| = |\rho_{10}|$, too, though slightly inclined due to dephasing. In this case, one can see, that the algorithm has the ability of “self-healing” if the choice for $|o_{01}(t)|$ is physically incorrect as here. Through more physical choices of $|o_{01}(t)| = |o_{10}(t)|$ (for example a smoothed step-function being flat in the regime where the wavepacket shall be stabilized), the achievement factor A being 0.872 here could be increased. The control field (upper panel of Fig. 5.2, $f = 94 \text{ mJ/cm}^2$) consists of two intense sub-pulses (approximately corresponding to two $\frac{\pi}{2}$ pulses) acting in the time-domains where population transfer takes place, and a low-intensity, cw-like field preserving the wavepacket in between.

5.3.2 Controlling a multi-level system

(a)



(b)

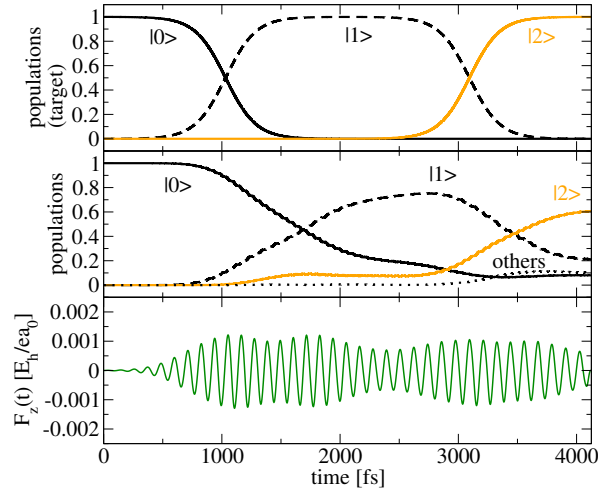


Figure 5.3: “Ladder climbing” $|0\rangle \rightarrow |1\rangle \rightarrow |2\rangle$ within the 9-level system: (a) Two \sin^2 -shaped π pulses (phase shift $\Delta\phi = \frac{\pi}{2}$) adjusted to the two respective transitions and the according population dynamics, where “others” labels $\sum_{i=3}^8 \rho_{ii}(t)$; (b) non-zero population target matrix elements $o_{ii}(t)$ for $(i = 0, 1, 2)$ in the upper panel and the actually obtained populations $\rho_{ii}(t)$ for $(i = 0, 1, 2)$ in the middle panel for the control field (lower panel).

Finally, to test the method for a multi-level system, the ground state $|0\rangle$ and the eight lowest excited eigenstates in Z (labeled $|1\rangle, |2\rangle, \dots, |8\rangle$), that is a 9-level system, is chosen. As the Z mode is rather harmonic for small quantum numbers, inducing a “ladder climbing” analogous to the five-fold excitation of the r mode in H/Si(100) (Sec. 4.2.1) is more difficult. Shown in Fig. 5.3 (a) is the field (upper panel) and the population dynamics (lower panel) as induced by two successive \sin^2 -shaped π pulses, each of duration 2062.5 fs and adjusted

to the transitions $|0\rangle \rightarrow |1\rangle$ and $|1\rangle \rightarrow |2\rangle$ in order to induce a two-step “ladder climbing”. Depending on the phase factor ϕ of the second π pulse (ϕ is being kept fixed at zero for the first pulse) one can excite state $|2\rangle$ at ($t = t_f = 4125$ fs) to populations of, for example, about 0.2 ($\phi = 0, \pi$) or ca. 0.4 for ($\phi = \frac{\pi}{2}$) as shown here. By fine-tuning the phase difference between the two pulses the result cannot be improved much further, as the population transfer does not occur sequentially. Thus the second pulse can only optimally transfer population to state $|2\rangle$, which is in state $|1\rangle$ during the second half of the control interval $[0, t_f]$. But, as can be seen in the lower panel of Fig. 5.3 (a), a considerable amount of population is still in the ground state 0 and up to 30 % are in higher excited states $|3\rangle, |4\rangle, \dots$

We now use the time-dependent target algorithm to enforce a *sequential* “ladder climbing” $|0\rangle \rightarrow |1\rangle \rightarrow |2\rangle$. Specifically we choose:

$$o_{00}(t) = \frac{C_0}{N(t)} e^{-\frac{(t-a_0)^2}{2\sigma_0^2}} \quad (5.22)$$

$$o_{11}(t) = \frac{C_1}{N(t)} e^{-\frac{(t-a_1)^2}{2\sigma_1^2}} \quad (5.23)$$

$$o_{22}(t) = \frac{C_0}{N(t)} e^{-\frac{(t-a_2)^2}{2\sigma_2^2}} \quad (5.24)$$

$$o_{01}(t) = C_{01} e^{-\frac{(t-a_{01})^2}{2\sigma_{01}^2}} e^{i\omega_{01}t} = o_{10}^*(t) \quad (5.25)$$

$$o_{12}(t) = C_{12} e^{-\frac{(t-a_{12})^2}{2\sigma_{12}^2}} e^{i\omega_{12}t} = o_{21}^*(t) \quad (5.26)$$

All other target matrix elements are kept zero. The upper panel of Fig. 5.3 (b) shows $o_{00}(t)$, $o_{11}(t)$ and $o_{22}(t)$ and the middle panel the actually obtained state populations $\rho_{00}(t)$, $\rho_{11}(t)$ and $\rho_{22}(t)$ for a penalty function of type (4.2) with $\alpha = 0.1$. The lower panel displays the control field of fluence 120 mJ/cm^2 (the total fluence of the two π pulses is 155 mJ/cm^{-1}). Although the target is not perfectly fulfilled ($A = 0.726$), the intended sequential mechanism is. As expected, this increases $\rho_{22}(t)$ to 0.61 and the amount of population transferred to higher states $|3\rangle, |4\rangle, \dots$ is decreased by the optimal pulse. The shape of the control pulse is rather complex, but one can roughly identify two “sub-pulses” which are responsible for the two transitions.

Chapter 6

Summary

The goal of the present work was to selectively excite vibrations of adsorbates on dissipative surfaces by pulsed IR light.

Models for CO/Cu(100), H/Si(100) and H₂/Ru(0001), where two, three and four vibrational degrees of freedom of the adsorbate were taken into account, have been set up in a reduced density matrix scheme. Energy and phase relaxation, that is the coupling to the electronic and phononic degrees of the surface “bath”, have been included within a Markovian, Lindblad scheme via dissipation and dephasing rates. The latter were taken/calculated from perturbation theory approaches. The vibrational rates explicitly calculated in this work for the system H₂/Ru(0001), being approximately 150 fs for the internal H–H stretch mode r and ca. 560 fs for the motion Z of H₂ with respect to the Ru(0001) surface, fit well with estimates from theory and experiment [21, 48] based on electronic friction coefficients. Vibrational lifetimes for the systems CO/Cu(100) and H/Si(100) were taken from earlier work by Tully *et al.* [36, 37] and Andrianov *et al.* [52], respectively. For the former system these range from about 2 ps for the C–O stretch mode r , confirmed by experiment [20], to over 100 ps for X/Y , the lateral motion of CO with respect to the copper surface. The adsorbate-surface stretch mode Z and angular degrees of freedom θ/ϕ have lifetimes ranging in between these values. In case of H/Si(100) the adsorbate-surface stretch mode r is long-lived (nanoseconds), while the adsorbate/surface bending mode ϕ lives for few picoseconds, in both cases in agreement with experimental findings [16, 17]. Dipole functions to model the semi-classical field-adsorbate interaction are obtained from fitting the data of quantum chemistry calculations to suitable

functions, reflecting the physically correct asymptotic behaviour and symmetries. Vibrational IR excitation was simulated by (a series of) \sin^2 -shaped pulses and pulses obtained from global optimal control theory. The according algorithm from Ohtsuki *et al.* [30] was implemented utilizing spectral decomposition of the time-evolution operator, interpolation via Newton polynomials and Schwarz-Christoffel conformal mapping [92, 93] to propagate the system in time, in obedience of the Liouville-von Neumann equation (2.13).

The challenges of the IR-excitation in the multi-dimensional and dissipative scenarios studied here are (1) the inter-mode coupling in the adsorbate and (2) dissipative processes, *i. e.* the coupling of the adsorbate vibrations to the surface “bath”. In the system CO/Cu(100), the internal adsorbate stretch mode r as well as the adsorbate-surface stretch mode Z at low temperatures can be highly and state-selectively populated. “Pure” dephasing (elastic scattering processes), which can be estimated for the r mode from experimental data [39], has been shown to be negligible for pulse lengths smaller than the “pure” dephasing time T_2^* . Henceforward, working in general with rather short pulses (in the picosecond and subpicosecond regime, usually chosen smaller than the energy relaxation time T_1), “pure” dephasing was neglected, only dephasing due to energy relaxation (inelastic scattering processes) was considered. For the high-energetic r mode, the dependence of “hot-band” excitation on pulse fluence was studied for monochromatic \sin^2 pulses as well as OCT pulses. It turned out that, delivering similar results for small fluences, OCT is of advantage at higher fluences as the algorithm finds a complex “chirp” structure which is able to avoid stimulated emission processes and can highly populate the overtone. The non-linear dependence of “hot-band intensities” on fluence found here for the system CO/Cu(100) is in agreement with a similar finding of Bonn *et al.* [119] for the C–O stretch mode in CO/Ru(0001). The r mode, further, does scarcely couple to the other, low-energetic modes, as a comparison of the according OCT pulses for a one- and a three-dimensional model has shown. This, however, is an effect of the potential of Tully *et al.* [36, 37] used here, it is possible that improved potentials will result in a different coupling behaviour. High temperatures, where the low-lying states are considerably Boltzmann-populated, have proven to lead to a decrease in population but not in state-selectivity upon irradiation with light in resonance with the Z mode. Even the overtones of the (“dark”) lateral mode X and the angular mode θ are accessible, although with smaller selectivity and the need for high-intensity pulses as they are (1) only weakly IR active and (2) there is considerable coupling to the Z mode. Latter, though, simplifies the excitation of the combination mode Z/X . The ϕ mode can be excited to some extent either, exploiting its population from the excited θ mode through dissipative effects. The Husimi

transforms, carried out to resolve the often complicated OCT pulses simultaneously in time and energy, deliver interesting information on “chirps”, off-resonant / static field contributions and allow to give better explanations on the excitation mechanisms. It was found that optimal control often chooses the best pathway on its own, so it might serve to deliver “non-intuitive” strategies to experimentalists. Within the two-dimensional model (r, Z) it was shown that vibrationally induced desorption would be achieved best via a pathway including as few as possible intermediate excitation steps, that is climbing the “ladder” in both r and Z modes. In future calculations with a similar aim, employing a suitable four- (r, Z, θ, ϕ) or full six-dimensional model, it can be expected that the rather energy-rich θ mode might play an additional role.

For the system H/Si(100), IR-induced desorption was attempted within a simple one-dimensional model of the H–Si stretch mode r , inspired by such a process experimentally induced for H/Si(111) [14]: The long-lived r mode can be excited by five quanta (state $|n_r = 5\rangle$ populated by over 94%), transferring 1.1 eV into the system, which allows, considering the energy gain of 2×2.3 eV per H–H bond formed, to overcome the (minimum) desorption barrier of 3.4 eV (as obtained from the energy balance for a single H atom). Thereby, it is suggested here to use five \sin^2 -shaped pulses (of moderate 17 mJ/cm² total fluence), “adjusted” to the five one-photon transitions. This is in contrast to the experimental set-up employed in case of the isotope-selective desorption of H₂ from a Si(111) surface with H and D co-adsorbed [14], where pulsed light of constant energy was employed. A possible explanation why desorption was still observed in Ref. [14] might be the occurrence of so-called energy pooling [129]. For the two-dimensional model, additionally including the angular mode ϕ (the angle of the H–Si bond with respect to the Si(100) surface), density matrix propagations employing the Markovian approximation (as throughout in the present work) were compared to non-Markovian calculations. For both field-free decay processes and IR excitations via \sin^2 -shaped pulses “hand-optimized” for the non-Markovian case, it was found that memory effects can play a role if (1) the excited states couple strongly to the substrate phonons, that is dissipation is strong and (2) a multitude of intermediate transitions takes place, as the non-Markovian effects “accumulate”; this is the case for high-energetic “ladder climbing” for example. Otherwise, the Markovian approximation holds well. Further, it was seen that, unlike the r mode, the ϕ mode is not as easy to populate, being less dipole active. Due to the harmonicity of the potential in ϕ , state-selective excitation is hard to achieve, optimal control theory being only able to reduce intensities/fluences slightly. Mode-selective excitation, however, is successful.

A similar situation was observed in the two-dimensional model of $\text{H}_2/\text{Ru}(0001)$, where both the H–H stretch mode r and the H_2 -surface stretch Z are quite harmonic. Additionally, unlike in the previous cases where vibrational lifetimes are in the ps or even ns (for the r mode of $\text{H}/\text{Si}(100)$) regime, both modes have a lifetime of only several hundreds of fs. The Z mode is easier to populate, even some state-selectivity can be achieved by OCT pulses. The only weakly IR allowed r mode is best accessed by overtone excitation for which the dipole transition moments are more advantageous.

Finally, a novel hybrid global/local OCT algorithm has been developed allowing to incorporate explicitly time-dependent target operators in the control scheme for dissipative systems according to Ref. [30]. The principle was to execute a series of global OCT calculations within small time-intervals (making up the total control interval) and thereby taking the final outcome of interval n as initial condition for the $(n + 1)$ th interval. For a two-level test system, the algorithm proved to be reliable, with the “normal” global OCT as limiting case for a single “sub-interval”. The algorithm proved to be both most accurate and computationally advantageous if the the number of sub-intervals coincides with the number of timesteps used for propagation. However, when choosing smaller timesteps (here some fs were used) this relation, particularly concerning the computational cost, might no longer hold true. The elements of the time-dependent target density matrix were given as analytical functions of time. Both populations and coherences of/between the states of interest were given in the time-dependent target. Although the set-up of a functional form for coherences is difficult, the algorithm possesses certain “self-healing” abilities, by fulfilling the population targets and “adjusting” the coherence terms. The algorithm has been successfully applied to two examples: (1) The creation, preservation and, finally, destruction of a wavepacket within the two-level model and (2) a two-step “ladder climbing” within a 9-level model of the Z mode of $\text{CO}/\text{Cu}(100)$. In the first case, the algorithm was able to correct the unphysically chosen coherence term of the target operator and thereby fulfilling the population dynamics as required by the target. It was possible to preserve the wavepacket for ca. 2 ps and with the present algorithm it is even feasible to keep the state populations constant for timescales equivalent to or longer than the respective lifetime of the excited state of 22 ps. The stabilization of the coherence, however, was futile. Within the present scheme it was only possible to let the absolute value of a coherence term oscillate about its natural decay (not shown for brevity). In the second case, the algorithm enables to enforce successive “ladder climbing” where a sequence of two π pulses excites many states at once (due to the rather large harmonicity of the considered mode at low energies) and thereby decreases the final target

outcome dramatically, somewhat depending on the phase difference between them.

This work offers the possibility for further extensions. The immediate prospects for the system CO/Cu(100) are full-dimensional calculations. The challenge for density matrix propagations, but even more so for OCT calculations, are numerical limitations with respect to the number of states considered. Global OCT in density matrix representation becomes numerically unstable and too costly for more than 40 to 50 states. One possibility is to select states “by hand” as done for the three- and four-dimensional models in the present work. Another interesting possibility might be to automatize this procedure by *iterated local balancing*; the according algorithm interfaced to OCT is currently developed by Scott Greenwald (Freie Universität Berlin). For H₂/Ru(0001) and possibly H/Si(100) higher-/full-dimensional models would also be of interest, in latter case the simulation of the desorption of H₂ and a comparison with H/Si(111), still to be modelled in theory, would be main goals. The OCT algorithm with time-dependent targets can be still improved, as at the moment the often unknown and/or complicated coherence terms are still necessary in the target as to generate an oscillating field. Generally, the control of larger dissipative systems such as surfaces, solids, liquids and biomolecules is aimed at. The present work shows that this goal is within reach.

Appendix A

Numerical methods for solving the stationary problem

In order to determine the multi-dimensional vibrational states in anharmonic systems, the time-independent Schrödinger equation (2.1) has to be solved. The numerical methods used to represent the Hamiltonian are summarized in the following.

A.1 Sinc-function discrete variable representation

A common approach for the numerical representation of Eq. (2.1) is to use a so-called discrete variable representation (DVR) [136–144] which has first been applied to solve the vibrational eigenproblem by Peet and Yang [145–147]. Unlike in variational basis representation (VBR) [141], the solutions of the eigenproblem in DVR are not expressed as coefficients of a set of basis functions $\phi_i(x)$ (x being the spatial coordinate, a vibrational mode q for example), but as coefficients of the approximate solutions $\tilde{\phi}_i(x_i)$ at chosen interpolation points x_i .

For both the discrete variable representation and the Fourier Grid Hamiltonian methods, the potential term \hat{V} of the total Hamiltonian $\hat{H} = \hat{T} + \hat{V}$ is diagonal in grid basis, that is the Hamiltonian matrix element (i, j) reads

$$H_{ij} = T_{ij} + V(q_i)\delta_{ij} \quad , \quad (\text{A.1})$$

with δ_{ij} being the Kronecker- δ which is 1 in case of $(i = j)$ and 0 if $(i \neq j)$. The derivation of expressions for T_{ij} in sinc-function DVR is sketched in the following.

In a one-dimensional quantum system, the kinetic energy operator \hat{T} reads

$$\hat{T} = -\frac{\hbar^2}{2m} \frac{d^2}{dx^2} \quad , \quad (\text{A.2})$$

with m being the (reduced) mass. In the sinc-function DVR method the coordinate x shall be restricted to the interval $[a, b]$ and the discrete points x_i for the DVR equally spaced, that is

$$\left(x_i = a + (b - a) \frac{i}{N} \right) \quad , \quad (\text{A.3})$$

with $i = 1, 2, \dots, (N - 1)$. The $(N - 1)$ functions for the $(N - 1)$ grid points are required to vanish at $(x = a)$ and $(x = b)$, respectively. The sinc-function DVR of Colbert and Miller [98] employed in this work, uses the particle-in-a-box eigenfunctions $\phi_n(q)$

$$\phi_n(x) = \left(\frac{2}{b - a} \right)^{\frac{1}{2}} \sin \left[\frac{n\pi(x - a)}{b - a} \right] \quad , \quad (\text{A.4})$$

which fulfill the condition $\phi_n(a) = \phi_n(b) = 0$.

In grid point representation, the matrix element (ij) of the kinetic energy operator of Eq. (A.2) becomes

$$T_{ij} = -\frac{\hbar^2}{2m} \Delta x \sum_{n=1}^{N-1} \tilde{\phi}_n(x_i) \tilde{\phi}_n''(x_j) \quad , \quad (\text{A.5})$$

where $\Delta x = (b - a)/N$ is the grid spacing, and $\tilde{\phi}_n''(x_j)$ is the second derivative of $\tilde{\phi}_n(x_j)$ with respect to x_j . Inserting Eq. (A.4) into Eq. (A.5), the latter becomes

$$T_{ij} = \frac{\hbar^2}{2m} \left(\frac{\pi}{b - a} \right)^2 \frac{2}{N} \sum_{n=1}^{N-1} n^2 \sin \left(\frac{n\pi i}{N} \right) \sin \left(\frac{n\pi j}{N} \right) \quad ; \quad (\text{A.6})$$

and if one evaluates the sum over n analytically¹, then:

$$T_{ij} = \frac{\hbar^2}{2m} \frac{(-1)^{(i-j)} \pi^2}{(b - a)^2} \frac{1}{2} \left(\frac{1}{\sin^2 [\pi(i - j)/2N]} - \frac{1}{\sin^2 [\pi(i + j)/2N]} \right) \quad . \quad (\text{A.7})$$

¹The term inside the sum gives $\frac{n^2}{2} \cos(nA) - \frac{n^2}{2} \cos(nB)$, with $A = \pi(i - j)$ and $B = \pi(i + j)$. Then $\sum_{n=1}^{N-1} n^2 \cos(nA) = -\frac{\partial^2}{\partial A^2} \text{Re} \sum_{n=1}^{N-1} e^{inA}$ and a second analogous expression for the B -term, with which the geometric series can be rewritten as $\text{Re} \sum_{n=1}^{N-1} e^{inA} = -\frac{1}{2} + \frac{1}{2} \frac{\sin[(N - \frac{1}{2})A]}{\sin(\frac{A}{2})}$, and the procedure to obtain Eq. (A.7) becomes clear.

Note, that Eq. (A.7) is only valid for ($i \neq j$).

For the limit ($a \rightarrow -\infty$) and ($b \rightarrow \infty$), but finite grid spacing $\Delta x_i = (x_{i+1} - x_i)$ with x_i according to Eq. (A.3), Eq. (A.7) becomes

$$T_{ij} = \frac{(-1)^{(i-j)}}{2m\Delta x_i^2} \cdot \begin{cases} \frac{\pi^2}{3} & , \text{ if } i = j \\ \frac{1}{(i-j)^2} & , \text{ else} \end{cases} . \quad (\text{A.8})$$

For a radial coordinate r with ($a = 0$) and ($b \rightarrow \infty$) and a grid spacing δr the matrix elements of the kinetic energy read [98]

$$T_{ij} = \frac{\hbar^2}{2m\delta r^2} (-1)^{(i-j)} \cdot \begin{cases} \frac{\pi^2}{3} - \frac{1}{2i^2} & , \text{ if } i = j \\ \frac{2}{(i-j)^2} - \frac{2}{(i+j)^2} & , \text{ else} \end{cases} . \quad (\text{A.9})$$

Note, that the matrix element vanishes if ($i = 0$) or ($j = 0$), that is ($r = 0$) itself is not a point on the grid. Further, it is [98]

$$T_{ij} = \frac{\hbar^2}{2m} \cdot \begin{cases} \frac{(-1)^{(i-j)}}{2} \left(\frac{1}{\sin^2\left[\frac{\pi(i-j)}{2N}\right]} - \frac{1}{\sin^2\left[\frac{\pi(i+j)}{2N}\right]} \right) & , \text{ if } i = j \\ \frac{1}{2} \left(\frac{2N^2+1}{3} - \frac{1}{\sin^2\left[\frac{\pi i}{N}\right]} \right) & , \text{ else} \end{cases} \quad (\text{A.10})$$

for a polar coordinate ($\theta \in [0, \pi]$) with grid points $\phi_i = \frac{i\pi}{N}$; the matrix element vanishes for ($i = 0$) or ($j = 0$), *i. e.* the points ($\theta = 0, \pi$) are not on the grid. Finally, in case of an azimuthal coordinate $\phi \in [0, 2\pi]$ represented by basis functions

$$\Phi_n(\phi) = \frac{e^{in\phi}}{\sqrt{2\pi}} , \quad (\text{A.11})$$

with ($n = 0, \pm 1, \pm 2, \dots, \pm N$) which obey the periodic boundary condition $\Phi_n(0) = \Phi_n(2\pi)$ and which are represented by grid points ($\phi_i = i\frac{2\pi}{2N+1}$) with ($i = 1, 2, \dots, 2N+1$), the matrix element becomes [98]

$$T_{ij} = \frac{\hbar^2}{2m} (-1)^{(i-j)} \cdot \begin{cases} \frac{N(N+1)}{3} & , \text{ if } i = j \\ \frac{\cos\left[\frac{\pi(i-j)}{2N} + 1\right]}{2\sin^2\left[\frac{\pi(i-j)}{2N} + 1\right]} & , \text{ else} \end{cases} , \quad (\text{A.12})$$

with $\Delta\phi$ being the grid spacing.

Equations (A.8), (A.9), (A.10), and (A.12) are simple expressions for the kinetic energy term as compared to other DVRs, see references cited above for example.

In a F -dimensional system the complete Hamiltonian matrix element $H_{n_i n_j}$ belonging to the two quantum number F -tupels n_i and n_j thus reads

$$H_{n_i n_j} = \sum_{i=1, j=1}^F T_{ij} \prod_{j, j' \neq i}^F \delta_{jj'} + V(x_i) \prod_{i, j=1}^F \delta_{ij} \quad , \quad (\text{A.13})$$

as the potential energy matrix is diagonal as for all DVRs in general, independent of the type of basis functions used.

A.2 Fourier Grid Hamiltonian

Similar to the sinc-function DVR method in Sec. A.1, in the Fourier Grid Hamiltonian (FGH) method [148] the $\phi_i(x)$ are to be determined in a grid basis, such that $\phi_i(x)$ is numerically represented at a finite number (N) of discrete, equidistant points x_i , for which ($\Delta x = x_{i+1} - x_i$). A possibility to do that, is to use so-called Dirac δ -functions [149] as basis functions

$$\phi_i(x) = \delta(x - x_i) \quad (\text{A.14})$$

which, although being not a *discrete* ortho-normal basis [150] as $\langle \phi_i(x) | \phi_j(x) \rangle = \delta(x_i - x_j)$ and thus $\delta(0)$ (for $i = j$) is not normalizable. This problem can be overcome in treating the δ -functions as *continuous* basis functions, from which in the development of the basis set only a subset is used, leading to a basis set error, but leaving a simple, diagonal expression for the potential energy

$$\langle \delta(x - x_i) | V(x) | \delta(x - x_j) \rangle = V(x_i) \delta(x_i - x) \quad . \quad (\text{A.15})$$

Using the general relations in quantum mechanics for the (inverse) Fourier transformation of wavefunctions $\psi(x)$ to (from) momentum space p

$$\bar{\psi}(p) = \frac{1}{\sqrt{2\pi\hbar}} \int_{-\infty}^{\infty} \psi(x) e^{-\frac{ipx}{\hbar}} dx \quad \text{and} \quad \psi(x) = \frac{1}{\sqrt{2\pi\hbar}} \int_{-\infty}^{\infty} \bar{\psi}(p) e^{\frac{ipx}{\hbar}} dp, \quad (\text{A.16})$$

from which the so-called Parseval equation

$$\int_{-\infty}^{\infty} |\psi(x)|^2 dx = \int_{-\infty}^{\infty} |\bar{\psi}(p)|^2 dp \quad (\text{A.17})$$

follows, one obtains as Fourier transformation $\bar{\delta}_{x_i}(p)$ of the δ -function

$$\bar{\delta}_{x_i}(p) = \frac{1}{\sqrt{2\pi\hbar}} \int_{-\infty}^{\infty} \delta(x - x_i) e^{-\frac{ipx}{\hbar}} dx = \frac{1}{\sqrt{2\pi\hbar}} e^{-\frac{ipx_i}{\hbar}} \quad . \quad (\text{A.18})$$

Using this relation, the elements H_{ij} of the field-free Hamiltonian $\hat{H}_0 = \frac{\hat{p}^2}{2m} + V(x) = -\frac{\hbar^2}{2m} \frac{d^2}{dx^2} + V(x)$ can be expressed in the basis of the $\delta(x - x_i)$ as

$$\begin{aligned} \left\langle \delta(x - x_i) \left| \hat{H}_0 \right| \delta(x - x_j) \right\rangle &= \left\langle \bar{\delta}_{x_i}(p) \left| \frac{\hat{p}^2}{2m} \right| \bar{\delta}_{x_j}(p) \right\rangle + V(x_i) \delta(x_i - x_j) \\ &= \frac{1}{2\pi\hbar} \int_{-\infty}^{\infty} e^{-\frac{ip(x_i - x_j)}{\hbar}} \frac{p^2}{2m} dp + V(x_i) \delta(x_i - x_j) \quad . \end{aligned} \quad (\text{A.19})$$

To simplify and merge Eq.(A.19) into a numerically easily applicable relation, *discrete* Fourier transformation is afforded, as in reality one only has a finite number of N data points and the values ψ_n of the function $\psi(x)$ are only known at spatial points ($x_n = n\Delta x$), with ($n = 0, 1, \dots, N - 1$) and Δx being the grid spacing in x . Through these N data points one can only access N independent values of the connected Fourier-transformed function $\bar{\psi}(p)$ within the momentum domain $p \in [-p_{max} : p_{max}]^2$, namely

$$p_j = \frac{\hbar j}{2N\Delta x} \quad , \quad j = -\frac{N}{2}, \dots, \frac{N}{2} \quad . \quad (\text{A.20})$$

Approximating the integral $\int_{-\infty}^{\infty}$ in (A.16) as sum $\sum_{n=0}^{N-1}$

$$\bar{\psi}(p_j) \approx \bar{\psi}_j = \frac{1}{\sqrt{2\pi\hbar}} \sum_{n=0}^{N-1} \psi_n e^{-\frac{ip_j x_n}{\hbar}} \Delta x \quad (\text{A.21})$$

and inserting $p_j x_n = \frac{\hbar j}{2N\Delta x} n\Delta x = \frac{\hbar j n}{2N}$, the expression for discrete Fourier transformation results

$$\bar{\psi}_j = \frac{\Delta x}{\sqrt{N}} \sum_{n=0}^{N-1} \psi_n e^{-\frac{ijn}{2N}} \quad , \quad (\text{A.22})$$

and analogously the inverse transformation

$$\psi(t_n) \approx \psi_n = \frac{\Delta p}{\sqrt{N}} \sum_{j=-\frac{N}{2}}^{\frac{N}{2}} \bar{\psi}_j e^{\frac{ijn}{2N}} \quad , \quad \text{with} \quad \Delta p = \frac{\hbar}{N\Delta x} \quad . \quad (\text{A.23})$$

Inserting the above relation (A.22) into Eq. (A.19) and assuming ($N = 2^i$) with $i, j \in \mathbf{N}$ and some lengthy conversions, the diagonal and off-diagonal elements of the Hamiltonian can be expressed as

$$T_{ii} = \frac{\pi^2}{\mu L^2} \frac{N^2 + 2}{6} \quad \text{and} \quad T_{ij} = (-1)^{(i-j)} \frac{\pi^2}{\mu L^2} \frac{1}{\sin^2 \left[\frac{(i-j)\pi}{N} \right]} \quad , \quad (\text{A.24})$$

² $p_{max} = \frac{\pi\hbar}{\Delta x}$ is the maximal momentum which can be resolved via the N grid points according to the Heisenberg principle $\Delta x \Delta p \geq \frac{\hbar}{2}$ and the so-called ‘‘sampling theorem’’ [151].

with $L = (N - 1)\Delta x$ being the grid length. As in case of the sinc-function DVR, the potential terms of the Hamiltonian are diagonal and H_{ij} is calculated according to Eq.(A.1).

The Hamiltonian matrix, when represented in either sinc-function DVR or FGH has then to be diagonalized in order to retrieve eigenvalues and eigenfunctions. This is done in the present work by the LAPACK routine DSYEVX [152].

A.3 Iterative two-term Lanczos eigensolver

As straightforward implementation of sinc-DVR and FGH methods of diagonalization as outlined in Secs. A.1 and A.2 reach their limits here with three dimensions, in Ref. [97] four- and six-dimensional eigenpairs (eigenstates and eigenvalues) were extracted according to recently published ideas [153–156], using a contracted iterative coupled two-term Lanczos eigensolver for extracting eigenpairs of the full dimensional Hamiltonian [157–159]. Advantages of iterative methods over direct methods are that they allow exploiting the structure of the Hamiltonian [160–168], and make it possible to extract only parts of the spectrum. The bottom part of the spectrum, which is needed for latter calculations, is known to converge first for Krylov subspace methods [160–168].

For the iterative scheme a basis of simply contracted functions was chosen, where the basic idea is to split the full dimension Hamiltonian into two or more reduced-dimension Hamiltonians. For a particular sub-dimensional Hamiltonian, the operator is represented in a tensor product basis of time-independent one-dimensional functions, such as DVR functions [98, 141, 169–175]. The lowest few energy levels and wavefunctions of each reduced-dimension Hamiltonian are obtained using an iterative eigensolver [170, 172, 176–183]. The resulting reduced-dimension wavefunctions are then used as a tensor product basis for the full dimension problem. Its eigenvalues and eigenvectors are then extracted using yet again an iterative eigensolver, for which it was shown that the structure of the matrix in the contracted basis can be exploited efficiently [153, 154]. The main advantage of this simple contraction strategy coupled to an iterative eigensolver is that it allows tackling larger systems in full dimension.

In the present study a mixed basis of potential optimized DVR (PO-DVR) was chosen for the motion on the surface along $\{X, Y\}$, and a contracted basis for the remaining degrees

of freedom, compare also the full six-dimensional Hamiltonian of Eq. (3.1). First, the four-dimensional Hamiltonian

$$\hat{H} = -\frac{\hbar^2}{2\mu} \frac{\partial^2}{\partial r^2} - \frac{\hbar^2}{2m} \frac{\partial^2}{\partial Z^2} + \frac{\hbar^2}{2\mu r^2} \hat{J}^2(\theta, \phi) + V(r, Z, \theta, \phi) \quad (\text{A.25})$$

was solved, where $V(r, Z, \theta, \phi)$ is obtained by fixing X and Y at their equilibrium values (see Sec. 3.1). The stretch degrees of freedom, r and Z , are represented using PO-DVR bases. They were generated by diagonalizing one-dimensional Hamiltonians represented using the sinc-DVR functions of Colbert and Miller [98], see above. The required one-dimensional potentials were obtained by freezing all other coordinates to their equilibrium values.

Real spherical harmonics were used to describe the angular degrees of freedom

$$|jm\rangle = N_{jm} P_j^{|m|}(\cos(\theta)) \begin{cases} \cos(m\phi) & \text{for } m \geq 0 \\ \sin(m\phi) & \text{for } m < 0 \end{cases}, \quad (\text{A.26})$$

where $P_j^{|m|}(\cos(\theta))$ are associated Legendre polynomials and N_{jm} are normalization constants, including the Condon-Shortley phase factor [153]. All spherical harmonics up to ($j_{max} = 30$) and ($-j_{max} < m \leq j_{max}$) were included in the basis for the contraction scheme. The angular part of the potential was represented on a direct product grid of ($N_\theta = j_{max} + 1$) points ranging from 0 to π for θ , and ($N_\phi = 2j_{max} + 1$) points ranging from 0 to 2π for ϕ . The lowest lying eigenvalues and eigenvectors of the resulting four-dimensional Hamiltonian matrix were extracted using the coupled two-term Lanczos algorithm. The eigenfunctions of the four-dimensional Hamiltonian have the form

$$|\Phi_i^{4D}\rangle = \sum_{\alpha\beta jm} C_{\alpha\beta jm}^{(i)} |\chi_\alpha(Z)\rangle |\chi_\beta(r)\rangle |jm\rangle, \quad (\text{A.27})$$

where $|\chi_\alpha(Z)\rangle$ are PO-DVR functions along Z and $|\chi_\beta(r)\rangle$ are PO-DVR functions along r . Full re-orthogonalization of the Lanczos vectors was used to favour convergence and to recover the true degeneracy of the eigenstates.

The eigenfunctions of the four-dimensional problem are used as a basis for the full dimension problem in combination with PO-DVR functions for the $\{X, Y\}$ coordinates. That is, the n th six-dimensional wavefunction has the form

$$|\psi_n\rangle = \sum_{\kappa\sigma i} A_{\kappa\sigma i}^{(n)} |\chi_\kappa(X)\rangle |\chi_\sigma(Y)\rangle |\Phi_i^{4D}\rangle, \quad (\text{A.28})$$

where $|\chi_\kappa(X)\rangle$ is a PO-DVR basis for X and $|\chi_\sigma(Y)\rangle$ is a PO-DVR basis for Y . The eigenfunctions are again extracted using a coupled two-term Lanczos eigensolver with full reorthogonalization. For implementation details, see Ref. [156].

Appendix B

Boundstate calculations for CO/Cu(100)

Shown in Fig. B.1 are selected two-dimensional eigenstates $|n_r, n_Z\rangle$ obtained from solving Eq. (3.6) on a grid, compare Sec. 3.1.1.

Figs. B.2 and B.3 depict two-dimensional cuts through the three-dimensional potential surface $V(r, Z, X)$ and selected vibrational eigenstates $|n_r, n_Z, n_X\rangle$, respectively. See Sec. 3.1.1 for more details.

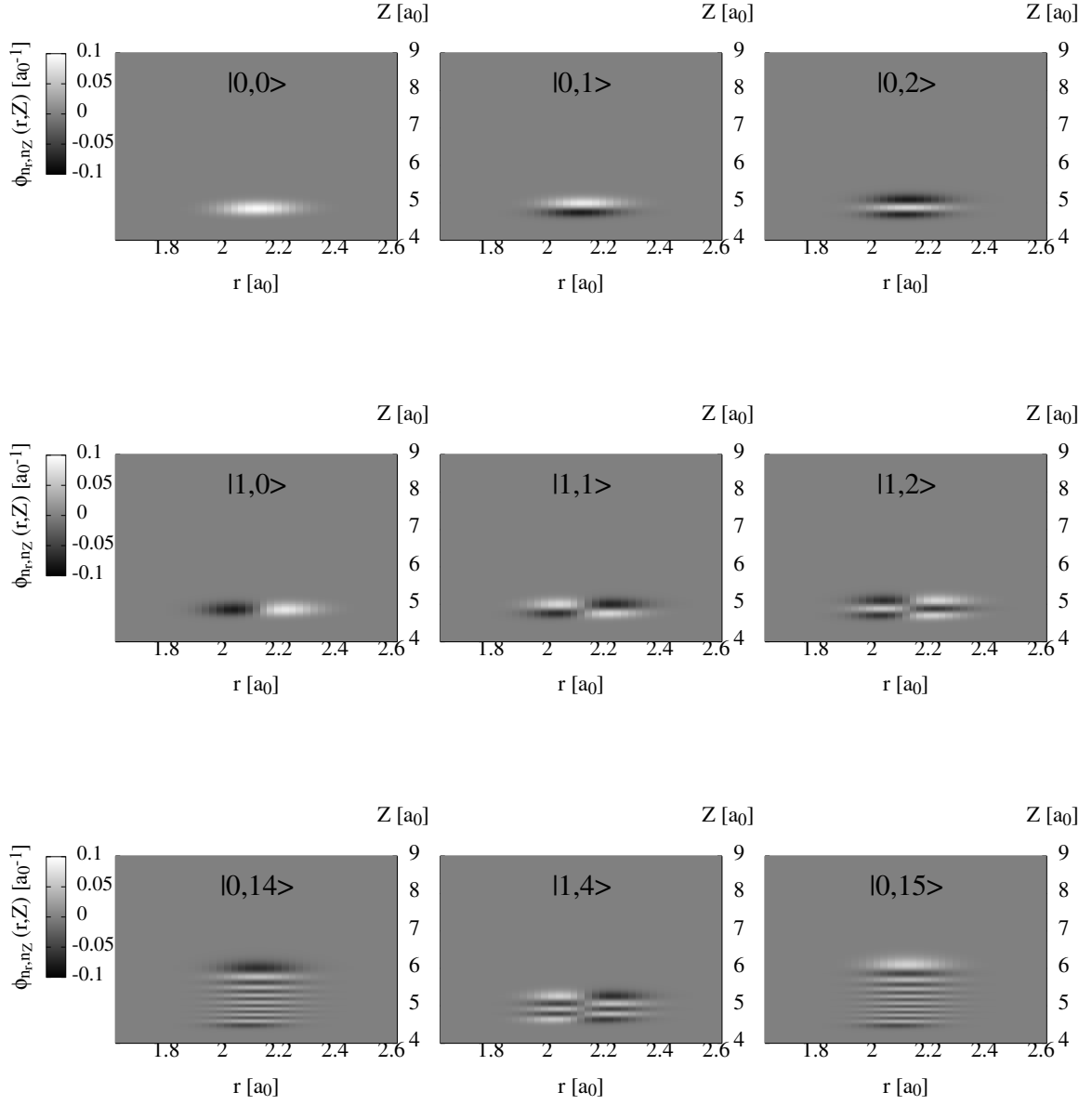
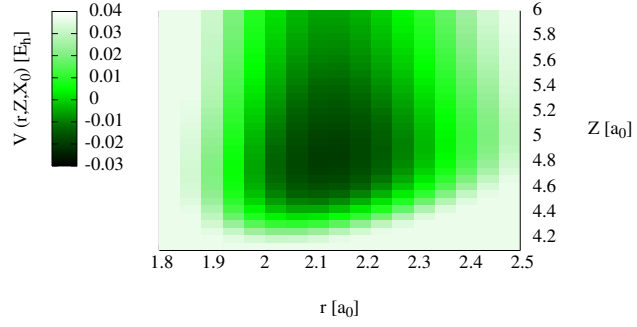
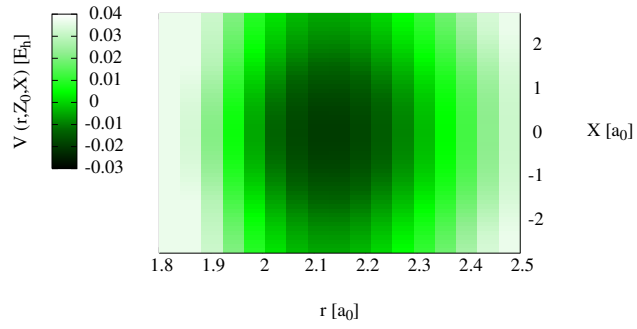


Figure B.1: Selected vibrational eigenstates $|n_r, n_z\rangle$ of the 2D CO/Cu(100) model as discussed in Sec. 3.1.1. State $|0, 14\rangle$ is the last bound state, states $|1, 4\rangle$ and $|0, 15\rangle$ are the first unbound states.

(a)



(b)



(b)

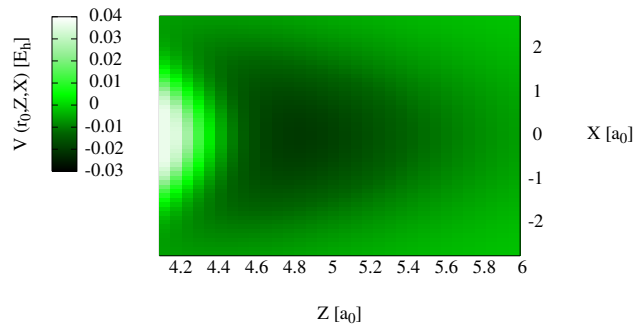


Figure B.2: 2D cuts through the 3D potential energy surface $V(r, Z, X)$ as obtained from Eqs. (3.3), (3.4) and (3.5). The Y , θ and ϕ degrees of freedom, see Fig. 3.1(a), are fixed at their equilibrium value of zero. For the cuts $X = X_0 = 0 a_0$ is chosen in a), $Z = Z_0 = 4.81 a_0$ in case of b) and $r = r_0 = 2.12 a_0$ in plot c).

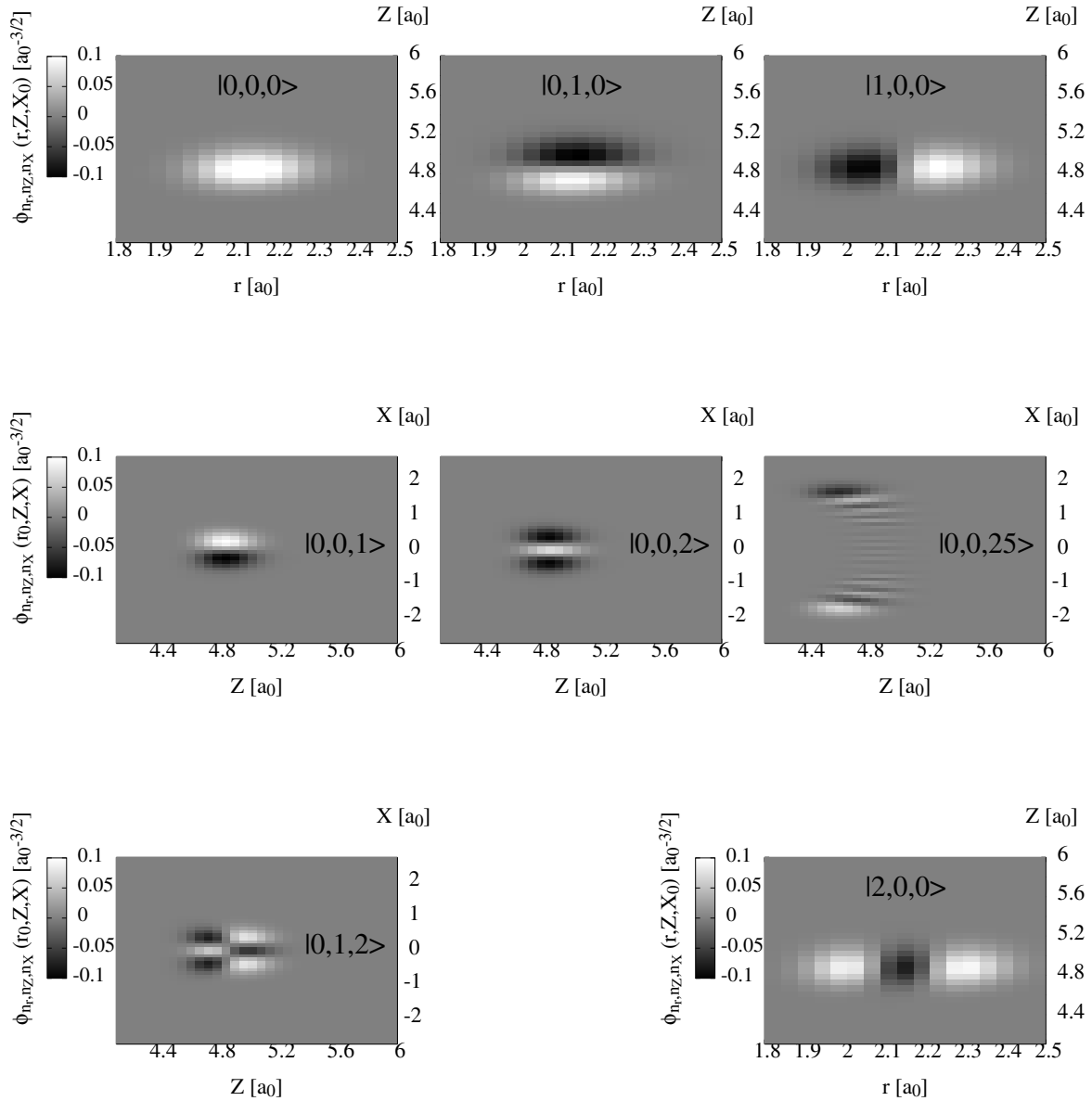


Figure B.3: Selected vibrational eigenstates $|n_r, n_Z, n_X\rangle$ of the 3D CO/Cu(100) model as discussed in Sec. 3.1.1, represented as 2D cuts with $X = X_0 = 0$ (r/Z plots) and $r = r_0 = 2.13 a_0$ (Z/X plots), respectively. Shown in the upper row are the ground state and the first excited states in Z and r – compare also Fig. B.1 above; in the middle row three wavefunctions are shown having nodes in X alone, displaying the *gerade* symmetry for even and *ungerade* for odd quantum numbers. In the lower row a “mixed” state, $|0, 1, 2\rangle$ and $|2, 0, 0\rangle$, the second excited state in the CO stretch mode r , latter lying above the desorption limit, are shown.

Appendix C

Numerical methods to solve the Liouville-von Neumann equation

The numerical solution of Eqs. (2.15) and (2.16) with a given field $F(t)$, is based on three concepts:

- The spectral decomposition of the time-evolution operator $e^{\tilde{\mathcal{L}}t} := G(\tilde{\mathcal{L}}t)$, where $\tilde{\mathcal{L}} = -\frac{i}{\hbar}\mathcal{L}$, in

$$\hat{\rho}(t) = e^{\tilde{\mathcal{L}}t}\hat{\rho}(0) = G(\tilde{\mathcal{L}}t)\hat{\rho}(0) \quad (\text{C.1})$$

by setting up the eigenequation

$$\tilde{\mathcal{L}}\hat{E}_n = \lambda_n\hat{E}_n \quad , \quad (\text{C.2})$$

with the λ_n and \hat{E}_n being the eigenvalues and eigenoperators of the Liouvillian $\tilde{\mathcal{L}}$. In this (exact!) representation the Liouvillian superoperator reads

$$\tilde{\mathcal{L}}\bullet = \sum_{n=0}^{L-1} \lambda_n \hat{E}_n \text{Tr}\{\hat{E}_n^\dagger \bullet\} \quad , \quad (\text{C.3})$$

with \bullet being the surrogate for the quantity the Liouvillian acts on and L the number of eigenvalues (if the Hamiltonian \hat{H} , from which the Liouvillian is constructed, has N eigenvalues, the Liouvillian has $N \times N$). Likewise $G(\tilde{\mathcal{L}})$ can be spectrally decomposed,

and following from that Eq. (C.1) then reads

$$\hat{\rho}(t) = \sum_{n=0}^{L-1} e^{\lambda_n t} \hat{E}_n \text{Tr}\{\hat{E}_n^\dagger \hat{\rho}(0)\} \quad , \quad (\text{C.4})$$

which can be used to obtain the time-dependent density, if \mathcal{L} can be diagonalized.

- But as eigenvalues λ_n and eigenoperators \hat{E}_n are usually not known and a direct diagonalisation of the Liouvillian is difficult or impossible, a convenient way to find approximations for them is by polynomial expansion of $G(\tilde{\mathcal{L}})$. At prespecified sampling points z_n , interpolation polynomials $P(z_n)$ reconstruct by definition the values of an unknown function $G(z_n)$. In this scheme, $G(\tilde{\mathcal{L}})$ still can be represented exactly as

$$G(\tilde{\mathcal{L}}) = P(\tilde{\mathcal{L}}) = \sum_{n=0}^{L-1} a_n R_n(\tilde{\mathcal{L}}) \quad . \quad (\text{C.5})$$

Specifically, if one uses a Newtonian interpolation scheme, it is

$$R_n(\tilde{\mathcal{L}}) = \begin{cases} \hat{\mathbb{1}} & , \quad n = 0 \\ \prod_{i=0}^{n-1} (\tilde{\mathcal{L}} - \lambda_i \hat{\mathbb{1}}) & , \quad n > 0 \end{cases} \quad , \quad (\text{C.6})$$

with $\hat{\mathbb{1}}$ being the unitary superoperator corresponding to the Liouvillian superoperator \mathcal{L} . And the coefficients a_n of Eq. (C.5) are the so-called divided differences, which generally are calculated as

$$\begin{aligned} a_0 &= \frac{G(\lambda_0)}{1} &= & G[\lambda_0] \\ a_1 &= \frac{G(\lambda_1) - G(\lambda_0)}{\lambda_1 - \lambda_0} &= & G[\lambda_0, \lambda_1] \\ a_2 &= \frac{G(\lambda_1, \lambda_2) - G(\lambda_0, \lambda_1)}{\lambda_2 - \lambda_0} &= & G[\lambda_0, \lambda_1, \lambda_2] \quad . \quad (\text{C.7}) \\ &\dots & & \\ a_n &= \frac{G(\lambda_1, \lambda_2, \dots, \lambda_n) - G(\lambda_0, \lambda_1, \dots, \lambda_{n-1})}{\lambda_n - \lambda_0} &= & G[\lambda_0, \lambda_1, \dots, \lambda_n] \end{aligned}$$

Graphically these divided differences can be obtained from a “pyramidal” scheme. Let’s assume four interpolation points $\lambda_0, \lambda_1, \lambda_2$ and λ_3 :

$$\begin{array}{l|l} \lambda_0 & G[\lambda_0] \\ & G[\lambda_0, \lambda_1] \\ \lambda_1 & G[\lambda_1] \quad G[\lambda_0, \lambda_1, \lambda_2] \\ & G[\lambda_1, \lambda_2] \quad G[\lambda_0, \lambda_1, \lambda_2, \lambda_3] \\ \lambda_2 & G[\lambda_2] \quad G[\lambda_1, \lambda_2, \lambda_3] \\ & G[\lambda_2, \lambda_3] \\ \lambda_3 & G[\lambda_3] \end{array} \quad . \quad (\text{C.8})$$

From this scheme, one obtains a certain coefficient of the Newtonian polynomial by forming the difference of the two coefficients (the lower one minus the upper one) immediately to the left of the quantity searched for and dividing this by the difference of the two interpolation points in the two rows following within this “pyramidal” pattern; so for example $G[\lambda_1, \lambda_2, \lambda_3] = \frac{G[\lambda_2, \lambda_3] - G[\lambda_1, \lambda_2]}{\lambda_3 - \lambda_1}$.

- Eq. (C.5) still requires the knowledge of the λ_n , one can indeed approximate from M sampling points $z_m^{(M)}$ as

$$G(\tilde{\mathcal{L}}) \approx \tilde{P}(\tilde{\mathcal{L}}) = \sum_{m=0}^{M-1} a_m R_m^{(M)}(\tilde{\mathcal{L}}) \quad . \quad (\text{C.9})$$

Here,

$$R_m^{(M)} = \begin{cases} \hat{1} & , \quad m = 0 \\ \prod_{i=0}^{m-1} (\tilde{\mathcal{L}} - z_i^{(M)} \hat{1}) & , \quad m > 0 \end{cases} \quad , \quad (\text{C.10})$$

and

$$\begin{aligned} a_0 &= \frac{G(z_0^{(M)})}{1} =: G[z_0^{(M)}] \\ a_1 &= \frac{G(z_1^{(M)}) - G(z_0^{(M)})}{z_1^{(M)} - z_0^{(M)}} =: G[z_0^{(M)}, z_1^{(M)}] \\ &\dots \\ a_m &= \frac{G(z_1^{(M)}, z_2^{(M)}, \dots, z_m^{(M)}) - G(z_0^{(M)}, z_1^{(M)}, \dots, z_{m-1}^{(M)})}{z_m^{(M)} - z_0^{(M)}} =: G[z_0^{(M)}, z_1^{(M)}, \dots, z_m^{(M)}] \quad . \end{aligned} \quad (\text{C.11})$$

Further, the number of sampling points actually used in the Newton interpolation is smaller than the number of eigenvalues λ_n of $\tilde{\mathcal{L}}$.

The $z_m^{(M)}$ are retrieved in the present work from a Schwarz-Christoffel conformal mapping scheme [92, 93]. This scheme finds uniformly distributed sampling points $z_m^{(M)}$ via a mapping of the complex eigenvalue spectrum on a rectangle of size $(a \times b)$, where a is the width of the energy spectrum, *i. e.* [$a = -\frac{i}{\hbar} \max(E_i - E_j)$], and [$b = \Gamma_D = \max(\Gamma_{i \rightarrow j}) + \max(\gamma_{ij})$], the maximum dissipation plus dephasing “strength”. This rectangle is located in the left half of the complex plane and mirror-symmetric with respect to the real axis, see Fig. C (a), and encloses all possible eigenvalues λ_n of $\tilde{\mathcal{L}}$.

As $G(\tilde{\mathcal{L}})$ is analytic, it can be fully specified by sampling points $(z_m^{(M)} \in D)$, where D is an arbitrary domain enclosing the eigenvalues λ_n . Almost optimal sampling points are uniformly distributed on D , that is

$$\lim_{M \rightarrow \infty} \max \left(|R_M(z)|^{\frac{1}{M}} \right) = r \quad , \quad (\text{C.12})$$

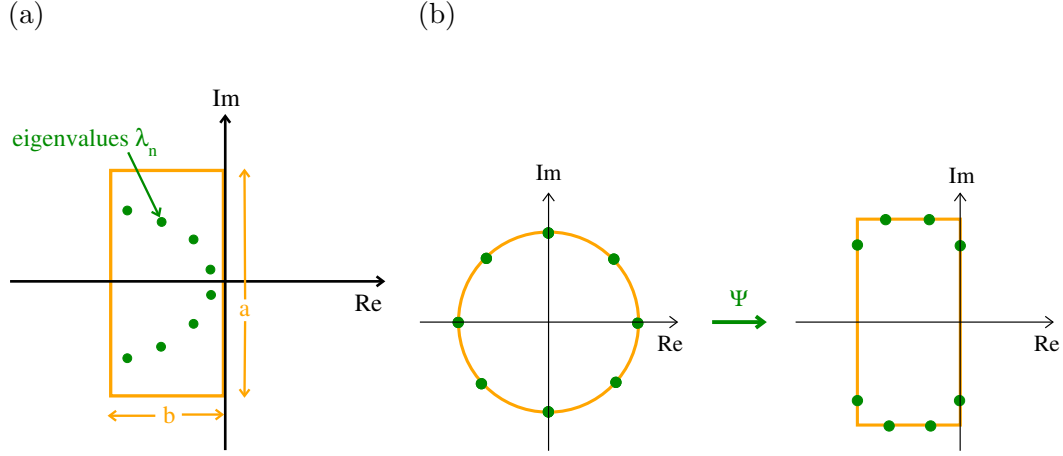


Figure C.1: Schwarz-Christoffel conformal mapping scheme: (a) A rectangle of size $(a \times b)$, located in the left half of the complex plane, with sides a and b , defined in the text, encloses all the eigenvalues λ_n of $\tilde{\mathcal{L}}$. Shown schematically in (b) is the mapping of eight sampling points $w_m^{(8)}$ uniformly distributed on the unity circle in the complex plane onto the rectangle of (a), delivering eight uniformly distributed sampling points $z_m^{(8)}$ being the optimal to represent the analytic function $G(\tilde{\mathcal{L}})$ via Eq. (C.9) and relations (C.10) and (C.11).

is valid for any $(z \in D)$. r is called the logarithmic capacity and is defined via

$$R_M(z) = \prod_{m=0}^{M-1} (z - z_m^{(M)}) \quad . \quad (\text{C.13})$$

If D is a circle, optimal sampling points $w_m^{(M)}$ can be chosen as the M roots of $(w^M = r)$ leading to $(w_m^{(M)} = re^{\frac{i2\pi m}{M}})$ with $(m = 0, 1, \dots, M - 1)$. This is exemplary shown for $(M = 8)$ in Fig. C (b) on the left side. The Schwarz-Christoffel transform [92, 93] numerically finds

$$z_m^{(M)} = \Psi \left[w_m^{(M)} \right] \quad , \quad (\text{C.14})$$

on a rectangle (in most cases), as is graphically shown in Fig. C (b) on the left. This numerical transformation is most stable if $(r = 1)$, *i. e.* when the w_m^M are the roots of the unity circle in the complex plane.

For each propagation the Schwarz-Christoffel mapping (giving the $z_m^{(M)}$ and thus the $R_M(z)$) and the calculation of the Newton polynomial coefficients a_m has to be done only

once. Then the dynamics can be solved by substituting the polynomial approximation (C.9) for $G(\tilde{\mathcal{L}}t)$ into Eq. (C.1) which describes the evolution of $\hat{\rho}(t)$ in time.

Appendix D

Numerical method to solve the TDSE: The split-operator propagator method

In order to solve the time-dependent Schrödinger equation (2.4) the wavefunction $|\psi(t)\rangle$ is expanded here in the basis of vibrational eigenstates $|\phi_i\rangle$

$$|\psi(t)\rangle = \sum_i C_i(t) |\phi_i\rangle \quad , \quad (\text{D.1})$$

with the $C_i(t)$ being the elements of the coefficient vector $\underline{C}(t)$ being evolved in time in accordance to Eq. (2.4). Further, time is discretized ($t \rightarrow t_i$) with $\Delta t = t_{i+1} - t_i$.

Using a splitting technique [184], the coefficient vector $\underline{C}(t + \Delta t)$ at time ($t = t + \Delta t$) can be evaluated as

$$\underline{C}(t + \Delta t) = \underline{U}^\dagger e^{-iF(t)\tilde{\underline{\mu}}\Delta t} \underline{U} e^{-i\tilde{\underline{H}}\Delta t} \underline{C}(t) \quad . \quad (\text{D.2})$$

Thereby, $\tilde{\underline{H}}$ is the (unperturbed) Hamiltonian matrix in basis of vibrational eigenstates which is diagonal with $\tilde{H}_{ii} = E_i$, the E_i being the vibrational eigenvalues. $\tilde{\underline{\mu}}$ is the (diagonal) dipole matrix and \underline{U} is an unitary matrix which transforms from the basis of vibrational eigenstates into a basis where the dipole matrix is diagonal.

Appendix E

Quantum chemical methods

E.1 Hartree-Fock theory

The Hartree-Fock (HF) method [70] offers an approximate solution for the (non-relativistic) time-independent electronic Schrödinger equation (2.1) within the Born-Oppenheimer approximation [69].

The ground state wavefunction $|\Psi_0\rangle$ is taken as a single Slater determinant [70] which is the simplest form of an antisymmetric N -electron wavefunction

$$|\Psi_0\rangle = \frac{1}{\sqrt{N!}} \begin{vmatrix} \chi_1(\underline{x}_1) & \chi_2(\underline{x}_1) & \cdots & \chi_N(\underline{x}_1) \\ \chi_1(\underline{x}_2) & \chi_2(\underline{x}_2) & \cdots & \chi_N(\underline{x}_2) \\ \vdots & \vdots & \ddots & \vdots \\ \chi_1(\underline{x}_N) & \chi_2(\underline{x}_N) & \cdots & \chi_N(\underline{x}_N) \end{vmatrix}. \quad (\text{E.1})$$

Here, the χ_i are one-electron spin orbitals with \underline{x}_j as vector describing the spin and spatial coordinates of electron j , where $\underline{x} = (r, \omega)$ consists of spatial and spin coordinates.

The electronic Hamiltonian \hat{H}_e consists of a sum of operators for the kinetic energy of the electrons \hat{T}_e , the attractive electron-nuclear interaction potential V_{en} and the repulsive electron-electron potential V_{ee} . The repulsive internuclear potential V_{nn} is a constant within the Born-Oppenheimer approximation for a given molecular geometry. With N_A being the number of nuclei, Z_A the charge of nucleus A and r_{pq} being the distance between particles p

and q , \hat{H}_e , expressed in atomic units, is

$$\hat{H}_e = - \underbrace{\sum_{i=1}^N \frac{\Delta_i}{2}}_{\hat{T}_e} - \underbrace{\sum_{i=1}^N \sum_{A=1}^{N_A} \frac{Z_A}{r_{iA}}}_{V_{en}} + \underbrace{\sum_{i=1}^N \sum_{j>i}^N \frac{1}{r_{ij}}}_{V_{ee}} + \underbrace{\sum_{A=1}^{N_A} \sum_{B>A}^{N_A} \frac{Z_A Z_B}{r_{AB}}}_{V_{nn}} . \quad (\text{E.2})$$

E.1.1 Hartree-Fock Equations

By variationally minimizing the expectation value for the ground state energy

$$E_0 = \langle \Psi_0 | \hat{H}_e | \Psi_0 \rangle \quad (\text{E.3})$$

and additionally applying the condition of orthonormal spin orbitals

$$\langle \chi_i | \chi_j \rangle = \delta_{ij} \quad (\text{E.4})$$

the Hartree-Fock equations are obtained

$$\hat{f}(\underline{x}_1) \chi_a(\underline{x}_1) = \varepsilon_a \chi_a(\underline{x}_1) \quad , \quad (\text{E.5})$$

where ε_a is the one-electron energy of spin orbital a . For closed-shell systems the spin variable can be eliminated by integration over ω to give the spin-free restricted Hartree-Fock (RHF) equations in which the spatial orbitals ψ_a are the same for α - and β -electrons:

$$\hat{f}(\underline{r}_1) \psi_a(\underline{r}_1) = \varepsilon_a \psi_a(\underline{r}_1) \quad . \quad (\text{E.6})$$

Here, the Fock operator reads

$$\hat{f}(\underline{r}_1) = \hat{h}(\underline{r}_1) + \underbrace{\sum_{b=1}^{\frac{N}{2}} \left(2\hat{J}_b(\underline{r}_1) - \hat{K}_b(\underline{r}_1) \right)}_{\hat{V}^{HF}(\underline{r}_1)} \quad , \quad (\text{E.7})$$

and \hat{J}_b and \hat{K}_b are Coulomb and exchange operators which constitute the Hartree-Fock potential $\hat{V}^{HF}(\underline{r}_1)$. (For their definition, see, for example, Ref. [70].)

In practical applications, the spatial molecular orbitals ψ_a of the Hartree-Fock equations (E.6) are expressed by a finite linear combination of K basis functions ϕ_ν centered at the atoms, *i. e.* by applying the LCAO-MO ansatz (Linear Combination of Atomic Orbitals to Molecular Orbitals):

$$\psi_a(\underline{r}_1) = \sum_{\nu=1}^K C_{\nu a} \phi_\nu(\underline{r}_1) \quad . \quad (\text{E.8})$$

By multiplying Eq. (E.6) by $\phi_\mu^*(\underline{r}_1)$ from the left, and integration over \underline{r}_1 one obtains the so-called Roothaan-Hall equations in matrix form

$$\underline{\underline{F}} \underline{C}_i = \varepsilon_i \underline{\underline{S}} \underline{C}_i \quad (\text{E.9})$$

which can be solved numerically.

Here, the matrix elements $F_{\mu\nu}$ and $S_{\mu\nu}$ of Fock and overlap matrix are

$$F_{\mu\nu} = \int d\underline{r}_1 \phi_\mu^*(\underline{r}_1) \hat{f}(\underline{r}_1) \phi_\nu(\underline{r}_1) = \langle \phi_\mu | \hat{f} | \phi_\nu \rangle \quad (\text{E.10})$$

$$S_{\mu\nu} = \int d\underline{r}_1 \phi_\mu^*(\underline{r}_1) \phi_\nu(\underline{r}_1) = \langle \phi_\mu | \phi_\nu \rangle \quad (\text{E.11})$$

Further, ε_i are the HF orbital energies, and

$$\underline{C}_i = \begin{pmatrix} C_{1i} \\ C_{2i} \\ \vdots \\ C_{Ki} \end{pmatrix} \quad (\text{E.12})$$

is the coefficient vector of MO i . Eq. (E.9) is solved by a self-consistent field (SCF) procedure.

E.2 Density functional theory

As a powerful alternative to wave-function based methods such as HF, density functional theory (DFT), which is based on the electronic density $\rho(\underline{r})$ has emerged. DFT methods are founded on the so-called Hohenberg-Kohn theorems.

E.2.1 Basics

One consequence of the Hohenberg-Kohn theorems is an expression for the ground state energy:

$$E_{HK}[\rho] = T[\rho] + \int \rho(\underline{r}) V_{en}(\underline{r}) d\underline{r} + J[\rho] + E_{xc}[\rho] \quad (\text{E.13})$$

Here, $\rho = \rho(\underline{r})$ is the electronic density, $T[\rho]$ the kinetic energy functional, $\int \rho(\underline{r}) V_{en}(\underline{r}) d\underline{r}$ is the electron-nuclear attraction, $J[\rho]$ the classical inter-electronic repulsion and $E_{xc}[\rho]$ the non-classical exchange-correlation functional.

While the Coulomb functional $J[\rho]$ can be written immediately as

$$J[\rho] = \frac{1}{2} \iint \frac{\rho(\underline{r}_1)\rho(\underline{r}_2)}{r_{12}} d\underline{r}_1 d\underline{r}_2 \quad , \quad (\text{E.14})$$

and $T[\rho]$ is calculated in the frame of the Kohn-Sham equations (see section E.2.2), suitable functionals for the nonclassical contributions to the energy must be found.

The functional $E_{xc}[\rho]$ is normally expressed as a sum of a correlation functional $E_c[\rho]$ and an exchange functional $E_x[\rho]$

$$E_{xc}[\rho] = E_c[\rho] + E_x[\rho] \quad . \quad (\text{E.15})$$

For the exchange functional $E_x[\rho]$, the local density approximation (LDA)

$$E_x^{LDA}[\rho] = -\alpha C_x \int \rho^{\frac{4}{3}}(\underline{r}) d\underline{r} \quad (\text{E.16})$$

$$(\text{E.17})$$

or the generalized gradient approximation (GGA)

$$E_x^{GGA}[\rho] = E_x^{LDA}[\rho] - \int \frac{|\nabla\rho|^2}{\rho(\underline{r})^{\frac{4}{3}}} f\left(\frac{|\nabla\rho|^2}{\rho(\underline{r})^{\frac{4}{3}}}\right) \quad (\text{E.18})$$

are popular, with α being atom-specific and C_x being a constant [185]. Further, in the semi-empirical Becke functional [186] $E_x^{B88}(=E_x^B)$ one uses

$$f(x) = \frac{\beta}{1 + 6\beta x \frac{1}{\sinh x}} \quad \text{with} \quad x = \frac{|\nabla\rho|}{\rho(\underline{r})^{\frac{4}{3}}} \quad . \quad (\text{E.19})$$

and β being a constant.

For the correlation energy a variety of functionals has been developed. Examples are the LDA correlation functional E_c^{LDA} and the the so-called LYP functional (GGA) of Lee, Yang and Parr [187] which contains one empirical parameter, and which is denoted as E_c^{LYP} . In the following we will mostly use the widely used B3LYP-functional [116]:

$$\begin{aligned} E_{xc}^{B3LYP} &= (1 - a')E_{xc}^{LDA} + a'E_x^{ex} + b'E_x^{B88} \\ &+ c'E_c^{LYP} + (1 - c')E_c^{LDA} \quad . \end{aligned} \quad (\text{E.20})$$

The parameters a , b , c and a' , b' , c' are obtained by fitting to sets of atomic and molecular data. B3LYP is a hybrid functional which also contains some ‘‘exact’’ (HF-like) exchange energy E_x .

E.2.2 Kohn-Sham equations

The Kohn-Sham equations offer a numerical way to compute the kinetic energy functional $T[\rho]$ and the ground state electron density $\rho(\underline{r})$ by introducing orbitals ψ_a^s .

In analogy to the Hartree-Fock one-particle operator \hat{f} in Eq. (E.7), a Kohn-Sham operator \hat{f}_{KS} can be defined and the canonical Kohn-Sham equations for RKS (Restricted Kohn-Sham) are

$$\underbrace{\left[-\frac{\Delta_1}{2} + V_{eff}(\underline{r}_1)\right]}_{\hat{f}_{KS}} \psi_a^s(\underline{r}_1) = \varepsilon_a^s \psi_a^s(\underline{r}_1) \quad . \quad (\text{E.21})$$

Solution of Eq. (E.21) yields Kohn-Sham orbitals ψ_a^s and orbital energies ε_a^s . The effective one-particle potential $V_{eff}(\underline{r}_1)$ is the sum of the external potential $V_{en}(\underline{r}_1)$, the Coulomb potential V_J and the exchange-correlation potential V_{xc}

$$V_{eff}(\underline{r}_1) = V_{en}(\underline{r}_1) + \underbrace{\frac{\delta J[\rho]}{\delta \rho}}_{V_J} + \underbrace{\frac{\delta E_{xc}[\rho]}{\delta \rho}}_{V_{xc}} \quad (\text{E.22})$$

in which the notation $\frac{\delta A[\rho]}{\delta \rho}$ represents functional derivatives. In contrast to the effective Hartree-Fock potential \hat{V}^{HF} , the effective Kohn-Sham potential V_{eff} is local.

The ground state electron density $\rho(\underline{r}_1)$ is simply given by

$$\rho(\underline{r}_1) = 2 \sum_{i=1}^{\frac{N}{2}} |\psi_i^s(\underline{r}_1)|^2 \quad . \quad (\text{E.23})$$

In a SCF procedure, starting from initial Kohn-Sham orbitals ψ_a^s , $\rho^{[0]}$, solutions for $V_{xc}^{[0]}$ and $V_{eff}^{[0]}$ are obtained. The n th iteration yields the orbital energies $\varepsilon_a^{s[n]}$ and the orbitals $\psi_a^{s[n]}$, so that $\rho^{[n]}$, $V_{xc}^{[n]}$ and $V_{eff}^{[n]}$ can be calculated. The iteration stops, when $E_{KS}^{[n]}$ and $\rho^{[n]}$ stay almost invariant in comparison with the previous iteration ($n-1$).

E.3 Effective core potentials

For chemical elements of third row and higher, like the metals copper and ruthenium for which quantum chemical calculations are carried out in this work, there is a large number

of core electrons which play no role in a chemical sense. But in order to represent the valence orbitals, these core orbitals, nevertheless, need to be expanded by a large number of basis functions, which would make it costly or impossible to calculate larger metal clusters. Further, relativistic effects are of importance in the second half of the periodic system, and they are not included in normal HF or DFT theory using Slater or Gaussian type orbital basis sets.

These two problems can be overcome by using so-called effective core potentials (ECPs) or pseudopotentials replacing the core electrons [188]. These are created by (1) generating a good all-electron wavefunction for the atom by either a numerical Hartree-Fock or a relativistic Dirac-Hartree-Fock calculation, (2) replacing the valence orbitals by a set of node-less pseudo-orbitals designed such that they behave correctly in the outer part, but do not have a nodal structure in the core region, (3) replacing the core electrons by a potential so that the solution of the Schrödinger (or Dirac) equation produces valence orbitals matching the pseudo-orbitals and (4) fitting this numerical potential to a suitable set of analytical functions, normally (two to seven) Gaussians

$$V_{ECP}(r) = \sum_i a_i r^{n_i} e^{-\alpha_i r^2} \quad . \quad (\text{E.24})$$

Parameters a_i , n_i and α_i depend on the angular momentum (s-, p-, d-, ...-shell) and are determined by least square fits.

The quasi-relativistic ECP used here for copper and ruthenium is LANL2 (Los Alamos National Laboratory 2) of Hay and Wadt [117]. Quasi-relativistic means that still a one-component wavefunction is employed (*i. e.*, no antimatter states and no spin-orbit coupling), however, the most important relativistic contributions such as the mass-velocity and so-called Darwin terms, are included. Ref. [117] also provides spacial atomic orbital basis sets to be used in conjunction with the ECPs.

Appendix F

A new parametrization of the CO/Cu(100) dipole function

A simple approach is chosen to fit an improved dipole function $\mu_z(r, Z)$ according to Eq. (3.9), based on cluster calculations:

- One-dimensional potentials $\tilde{V}(r, Z_0)$ and $\tilde{V}(r_0, Z)$ and the corresponding dipole functions $\tilde{\mu}_z(r, Z_0)$ and $\tilde{\mu}_z(r_0, Z)$ are calculated with the help of a cluster model and equilibrium distances $r_0 = 2.13 a_0$, $Z_0 = 4.81$ according to the potential of Refs. [36, 37].
- The points of the calculated $\tilde{\mu}_z(r, Z_0)$ and $\tilde{\mu}_z(r_0, Z)$ are fitted to the linear form

$$\tilde{\mu}_0 + a(r - r_0) \tag{F.1}$$

along r and Mecke form along Z

$$[\tilde{\mu}_0 - b(Z - Z_0)] e^{-\frac{Z-Z_0}{c}} \quad , \tag{F.2}$$

respectively, where $\tilde{\mu}_0$ is the equilibrium dipole moment (along z) of the cluster model. The intervals in which these two fits are carried out are determined by a certain limit in the squared difference between the Tully potential $V(r, Z)$ and the calculated potential $\tilde{V}(r, Z)$. Here, this limit is chosen to be $5 \cdot 10^{-4} E_h$ – the precision of energy convergence of the SCF procedure.

- The parameters obtained in this way enter Eq. (3.9). The disparity between the actual μ_0 and the $\tilde{\mu}_0$ of the cluster model is not affecting the linear term in r , being a mere addition in the total dipole expression, but it changes the curvature in the Mecke term when transferring parameters b and c from $\tilde{\mu}_z(r, Z)$ to $\mu_z(r, Z)$, due to the requirement of correct asymptotic behaviour for ($Z \rightarrow \infty$).

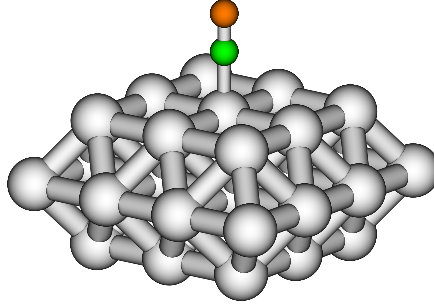


Figure F.1: CO@Cu₃₄ cluster on which the B3LYP calculations for the improved dipole function were performed.

Shown in Fig. F.1 is the cluster model which was found to be most suitable. It consists of 34 copper atoms, arranged in three layers á 9, 16 and 9 atoms, respectively. The bonding distances were chosen in accordance with the potential of Tully *et al.* [36, 37], that is $r_0 = 2.126 a_0$, $Z_0 = 4.81 a_0$ and a lattice constant of $6.829 a_0$ – copper being of fcc (face-centered cubic) structure. As method, B3LYP [116] (see also Eq. (E.20) in Sec. E.2.1) was chosen. The basis for C and O was 6-311G (d,p) [189]. For all Cu atoms a quasi-relativistic effective core potential – LANL2 (Los Alamos National Laboratories 2) – and the corresponding basis set for 19 valence electrons per copper was chosen. The first and third metal layer are treated completely in double-zeta basis (LANL2DZ), likewise the four inner atoms of the second layer (having direct bonds to the first layer Cu-atom upon which CO is absorbed). The outer atoms of the second layer are treated within minimal basis (LANL2MB). See Appendix E, Sec. E.3 for more details on pseudopotentials and LANL2(DZ/MB) in particular. All calculations were carried out using the GAUSSIAN 03 programme package [108]

The top panels of Fig. F.2 (a) and (b), display in dashed lines the potential energy surfaces $V(r, Z_0) - V(r_0, Z_0)$ and $V(r_0, Z) - V(r_0, Z_0)$ as obtained from the potential of Tully *et al.* [36, 37], by setting all system coordinates to their equilibrium values in Eqs. (3.3), (3.4)

and (3.5), with the exception of r (a) and Z (b) respectively. Plotted in green solid lines are the results for $\tilde{V}(r, Z_0) - \tilde{V}(r_0, Z_0)$ and $\tilde{V}(r_0, Z) - \tilde{V}(r_0, Z_0)$ from cluster calculations. In both cases the calculations underestimate the repulsion for negative displacements and overestimate it for positive displacements, both thought to be a result of having a finite cluster instead of a surface¹. Close to the respective equilibrium positions the agreement is good. The points within the regions where squared difference between the (relative) cluster potential and the potential of Tully and co-workers is smaller than $5 \cdot 10^{-4} E_h$ is chosen for the dipole fits (see above) which are plotted in the middle panels of (a) and (b): The dashed line indicates the calculated points and the solid green line the fits to Eq. (F.1) in (a) and to Eq. (F.2) in (b). These fits deliver, with a precision of $0.001 e / 0.001 a_0$, $a = -1.810 e$ for the linear term and $b = -0.510 e$ and $c = 1.808 a_0$ for the Mecke term. The lower panels finally show $\mu_z(r, Z_0) = \mu_0 + a(r - r_0)$ and $\mu_z(r_0, Z) = [\mu_0 - b(Z - Z_0)] e^{-\frac{Z-Z_0}{c}}$ in solid green lines, with the parameters obtained from $\mu_z(r, Z_0)$ and $\mu_z(r_0, Z)$, respectively. Plotted for comparison (dashed lines) are the same terms from the old dipole function (3.8). Note, that the “bend” in $\tilde{\mu}_z(r, Z_0)$ occurring shortly after $r = 2.3 a_0$ is probably due to an arbitrary change of sign of the cluster dipole moment.

An extended two-dimensional model is taken into account to present the differences between old and new dipole function. It consists not only of 21 states, as is the case for the model presented in Sec. 3.1.1, which is suited to study low-energetic excitations – containing only two states above the desorption limit – but contains further “continuum states”, compare Sec. 4.1.2. Plotted in Fig. F.3 are the dipole transition moments of interest, being those between “pure” states $|0, n_Z\rangle$, $|0, m_Z\rangle$ in the Z mode. Fig. F.3 (a) and (b) display those values obtained for the old dipole function (3.8). As can be seen in (a) $\mu_{(0, n_Z)(0, m_Z)}$ increases for single quantum transitions $[(m_Z = n_Z \pm 1)$, the row parallel to the diagonal ($n_Z = m_Z$)] up to a quantum number of 8, then it decreases. Double excitations $[(m_Z = n_Z \pm 2)$, the row parallel to the single excitation terms] display a similar behaviour, but peaking later on around quantum numbers 16/17 and having in general smaller values. Still smaller values are obtained for triple excitations, which gain a role only at or above the desorption limit ($>$ quantum number 14). For still higher quantum numbers, though, the dipole transition moments for single transitions explode to very large values due to the quadratic term in Z . For the new dipole form (3.9), the data shown in (c), this does not happen. After running through their maxima the dipole transition momenta for one-, two- and three-quanta transitions approach zero for $(n_Z, m_Z \rightarrow \infty)$.

¹However, it is also not clear whether the potential surface of Refs. [36, 37] is accurate.

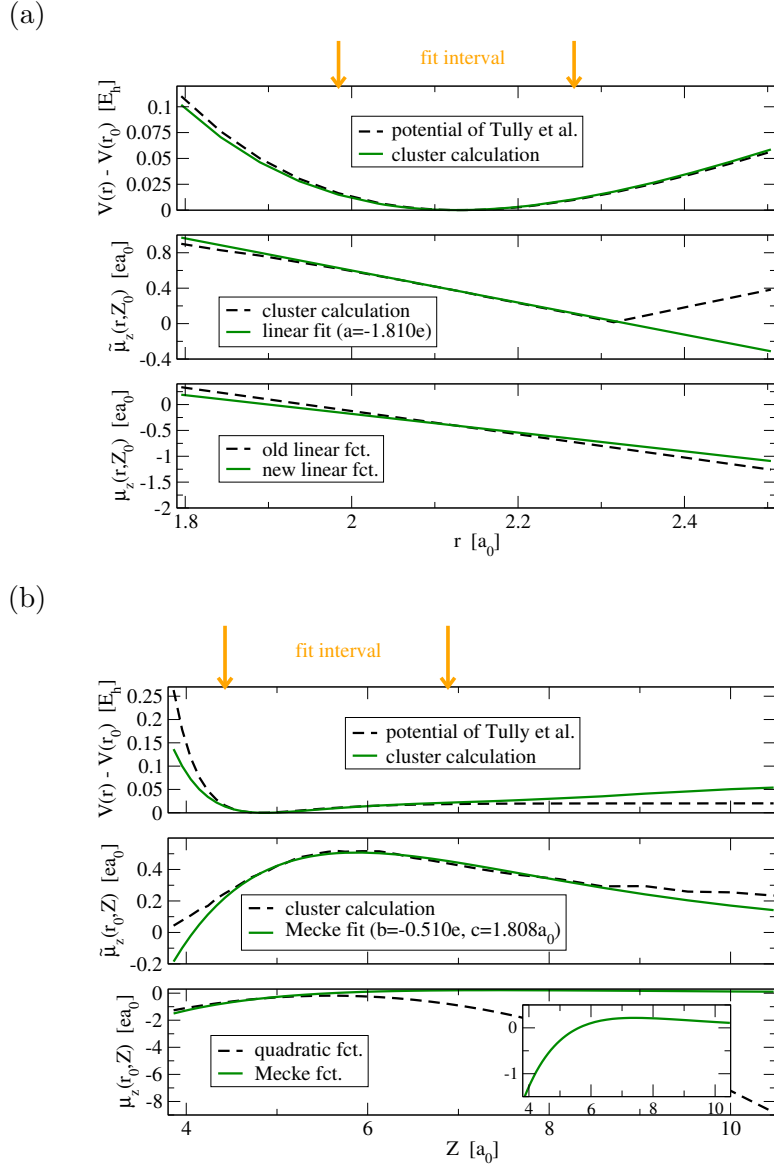
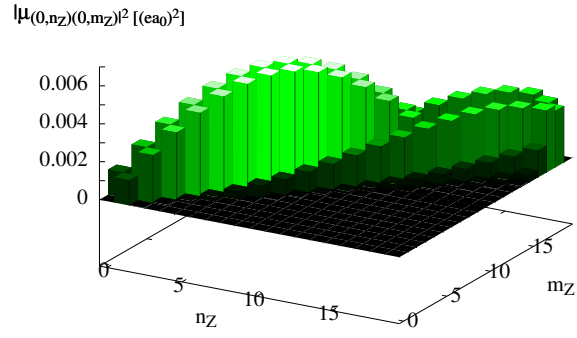
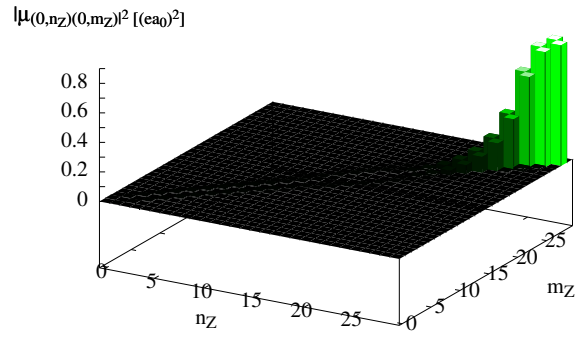


Figure F.2: Cluster calculations and fits to improve $\mu_z(r, Z_0)$ (a) and $\mu_z(r_0, Z)$ (b). Top panels: The potentials $V(r, Z_0) - V(r_0, Z_0)$ and $V(r_0, Z) - V(r_0, Z_0)$ (dashed lines) as derived from the six-dimensional PES of Tully *et al.* [36,37] and potentials $\tilde{V}(r, Z_0)$ and $\tilde{V}(r_0, Z)$ (solid green lines) calculated from the CO@Cu₃₄ cluster (Fig. F.1) within B3LYP/LANL2(DZ/MB). Middle panels: Dipole functions $\tilde{\mu}_z(r, Z_0)$ (a) and $\tilde{\mu}_z(r_0, Z)$ (b) as obtained from the cluster calculations (dashed lines) and fits (solid green lines) to Eq. (F.1) in (a) and to Eq. (F.2) in (b). Lower panels: $\mu_z(r, Z_0)$ (a) and $\mu_z(r_0, Z)$ (b) according to the old dipole function of Eq. (3.8) with parameters $A = -2.25 e$, $B = 0.566 e$ and $C = -0.361 e/a_0$ (dashed lines) and according to the new functional form of Eq. (3.9) with the parameters obtained from the fits.

(a)



(b)



(c)

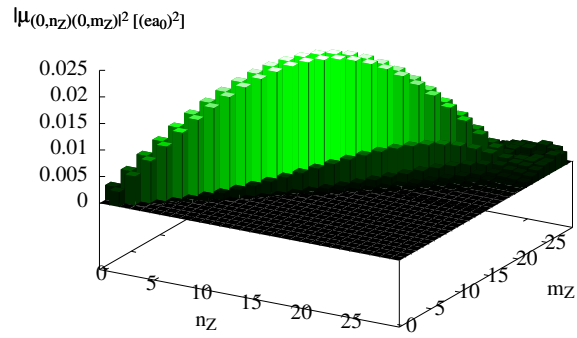


Figure F.3: Squared dipole transition matrix elements $|\mu_{(0,n_z)(0,m_z)}|^2$ as obtained within the 2D model of CO/Cu(100) for the old dipole form of Eq. (3.8) (a+b) and the new form of Eq. (3.9) (c).

Appendix G

Non-Markovian theory

One variant of reduced density matrix theory for the laser-driven vibrational system dynamics used in Ref. [104] and Sec. 4.2.2 includes “memory” (non-Markovian theory) and is described in the following.

The interaction picture is used here, *i. e.* the system-bath interaction (see the Hamiltonian for the combined total system in Eq. (3.21)) can generally be written as

$$\hat{H}_{SB} = \sum_k \hat{Q}_k(s_1, s_2, \dots, s_N) \hat{F}_k(q_1, q_2, \dots, q_M) \quad . \quad (\text{G.1})$$

\hat{H}_{SB} is bilinear in system and bath operators $\hat{Q}_k(s_1, s_2, \dots, s_N)$ and $F_k(q_1, q_2, \dots, q_M)$, where s_1, s_2, \dots, s_N ($=r, \phi$, here) and q_1, q_2, \dots, q_M are the N system and M bath coordinates, respectively. In the model for H/Si(100) used here,

$$\hat{H}_{SB} = \sum_{i=1}^M \lambda_i(r, \phi) q_i + \sum_{i=1}^M \sum_{j=1}^M \Lambda_{ij}(r, \phi) q_i q_j \quad . \quad (\text{G.2})$$

Further, the system and bath Hamiltonians \hat{H}_S and \hat{H}_B are given by Eqs. (3.18) and (3.22). The density operator characterizing the total system in the interaction picture¹ is denoted by $\hat{\sigma}^I(t)$. Its time evolution is governed by the Liouville equation, see, *e. g.*, Ref. [54],

$$\frac{\partial \hat{\sigma}^I(t)}{\partial t} = \frac{i}{\hbar} F_z(t) [\mu_z^I(r, \phi, t), \hat{\sigma}^I(t)] - \frac{i}{\hbar} [\hat{H}_{SB}^I(r, \phi, \{q_i\}, t), \sigma^I(t)] \quad . \quad (\text{G.6})$$

¹The density operator $\sigma^I(t)$ and the operators of Eq. (G.6) in the interaction picture are related

The statistical description of the system coupled to an unobserved bath is provided by the reduced density operator $\hat{\rho}^I(t) = \text{Tr}_B \{ \hat{\sigma}^I(t) \}$. The equation of motion for the reduced density operator is obtained [54] by making use of the formal solution of the Liouville equation (G.6) which gives – under the condition of irreversibility, *i. e.* $\hat{\sigma}^I(t) = \hat{\rho}^I(t) \hat{\rho}_B(0)$ – the equation of motion for the reduced density operator

$$\frac{\partial \hat{\rho}^I(t)}{\partial t} = \frac{i}{\hbar} F_z(t) [\mu^I(r, \phi, t), \hat{\rho}^I(t)] - \frac{1}{\hbar^2} \hat{R}^I(r, \phi, t) \quad , \quad (\text{G.7})$$

where $\hat{R}^I(r, \phi, t)$, which will be referred to as the time-dependent relaxation operator, is

$$\begin{aligned} \hat{R}^I(r, \phi, t) &= \hat{R}_1^I(r, \phi, t) + \hat{R}_2^I(r, \phi, t) = \\ &= \sum_i^M \int_0^t dt' \left\{ \left[\lambda_i^I(r, \phi, t), \lambda_i^I(r, \phi, t') \hat{\rho}^I(t') \right] \langle Q_i(t) Q_i(t') \rangle \right. \\ &\quad \left. - \left[\lambda_i^I(r, \phi, t) \quad , \hat{\rho}^I(t') \lambda_i^I(r, \phi, t') \right] \langle Q_i(t') Q_i(t) \rangle \right\} \\ &\quad + \frac{1}{2} \sum_i^M \sum_j^M \int_0^t dt' \left\{ \left[\Lambda_{ij}^I(r, \phi, t), \Lambda_{ij}^I(r, \phi, t') \hat{\rho}^I(t') \right] \langle Q_{ij}(t) Q_{ij}(t') \rangle \right. \\ &\quad \left. - \left[\Lambda_{ij}^I(r, \phi, t), \hat{\rho}^I(t') \Lambda_{ij}^I(r, \phi, t') \right] \langle Q_{ij}(t') Q_{ij}(t) \rangle \right\} \quad . \end{aligned} \quad (\text{G.8})$$

The overall relaxation operator $\hat{R}^I(r, \phi, t)$ consists of two parts, $\hat{R}_1^I(r, \phi, t)$ accounting for one-phonon relaxation, and $\hat{R}_2^I(r, \phi, t)$ accounting for two-phonon relaxation. The $\langle Q_i(t) Q_i(t') \rangle = \text{Tr}_B \{ q_i^I(t) q_i^I(t') \hat{\rho}_B(0) \}$ and the $\langle Q_{ij}(t) Q_{ij}(t') \rangle = \text{Tr}_B \{ q_i^I(t) q_j^I(t) q_i^I(t') q_j^I(t') \hat{\rho}_B(0) \}$ are time correlation functions and it can be easily shown that $\langle Q_{ij}(t) Q_{ij}(t') \rangle = \langle Q_i(t) Q_i(t') \rangle \langle Q_j(t) Q_j(t') \rangle$.

For the bath represented by normal modes (an ensemble of harmonic oscillators) [see Eq. (3.22)] it can be shown that the time correlation function for one-phonon transitions, $\langle Q_i(t) Q_i(t') \rangle$, has the following form:

$$\langle Q_i(t) Q_i(t') \rangle = \frac{\hbar}{2M_i \omega_i} \Phi(\omega_i, t - t', T) \quad ,$$

$$\Phi(\omega_i, t - t', T) = [\bar{n}(\omega_i) + 1] \exp[-i\omega_i(t - t')] + \bar{n}(\omega_i) \exp[i\omega_i(t - t')] \quad , \quad (\text{G.9})$$

to the Schrödinger picture as follows:

$$\hat{\sigma}^I(t) = e^{i(\hat{H}_S + \hat{H}_B)t/\hbar} \hat{\sigma}(t) e^{-i(\hat{H}_S + \hat{H}_B)t/\hbar} \quad , \quad (\text{G.3})$$

$$B^I(r, \phi, t) = e^{i\hat{H}_S t/\hbar} B(r, \phi) e^{-i\hat{H}_S t/\hbar} \quad (\text{with } B = \mu_z, \lambda_i, \text{ or } \Lambda_{ij}) \quad , \quad (\text{G.4})$$

$$q_i^I(t) = e^{i\hat{H}_B t/\hbar} q_i e^{-i\hat{H}_B t/\hbar} \quad . \quad (\text{G.5})$$

where

$$\bar{n}(\omega_i) = \frac{1}{\exp(\hbar\omega_i/k_B T) - 1} \quad (\text{G.10})$$

is the Bose-Einstein distribution function.

Equation of motion (G.7) has been treated numerically in the system-state representation. Taking matrix elements between the system eigenstates $|n\rangle = \psi_n(r, \phi)$, one gets

$$\frac{d\rho_{nn'}^I(t)}{dt} = \frac{i}{\hbar} F_z(t) [\mu_z^I(t), \hat{\rho}^I(t)]_{nn'} - \frac{1}{\hbar^2} [R_{1nn'}^I(t) + R_{2nn'}^I(t)] \quad . \quad (\text{G.11})$$

The explicit treatment of the two-phonon relaxation with matrix $R_{2nn'}^I(t)$ is very costly, therefore a quiresonant model, similar to those used in previous works [190, 191] and a partial averaging over one of two bath variables have been used. A partial averaging over the j -coordinate of the bath yields

$$\begin{aligned} R_{2nn'}^I(t) \Rightarrow & \frac{\hbar^2}{8} \sum_i^M \int_0^t dt' \left\{ \frac{[\Lambda_i^I(t), \Lambda_i^I(t') \hat{\rho}^I(t')]_{nn'}}{M_i \omega_i} \sum_j^M \Phi(\omega_i, t - t', T) \Phi(\omega_j, t - t', T) \right. \\ & \left. - \frac{[\Lambda_i^I(t), \hat{\rho}^I(t') \Lambda_i^I(t')]_{nn'}}{M_i \omega_i} \sum_j^M \Phi(\omega_i, t - t', T)^* \Phi(\omega_j, t - t', T)^* \right\} \quad , \quad (\text{G.12}) \end{aligned}$$

where the products of the matrix elements between the system states for the two-phonon transitions are defined as:

$$\Lambda_i^I(t)_{nk} \Lambda_i^I(t')_{ln'} = \frac{1}{M} \sum_j^M \frac{\Lambda_{ij}^I(t)_{nk} \Lambda_{ij}^I(t')_{ln'}}{M_j \omega_j} \quad . \quad (\text{G.13})$$

The products of the matrix elements given by Eq. (G.13) have been calculated in the Schrödinger picture by making use of the results given in Appendix B of Ref. [52], see Eq. (33) therein, and subsequently transformed into the interaction picture.

A quiresonant model for the two-phonon relaxation has been employed as follows. Taking into account that the most efficient energy exchange among coupled systems occurs in the case of resonance, it is reasonable to assume that the two-phonon relaxation depends on the bath frequency ω_j in a resonant way with respect to any system frequency ω_{mn} and the other bath frequency ω_i . Specifically, similar to previous works [190, 191], the following substitution is made in Eq. (G.12):

$$\sum_j^M \Phi(\omega_i, t - t', T) \Phi(\omega_j, t - t', T) \Rightarrow$$

$$\Rightarrow \sum_{m=1}^{v_{max}} \sum_{n=0}^{m-1} \int_{A_{mn}}^{B_{mn}} \Phi(\omega_i, t - t', T) \Phi(\Omega, t - t', T) g_{mni}(\Omega) d\Omega \quad , \quad (\text{G.14})$$

where ($A_{mn} < \omega_{mn} < B_{mn}$) and $g_{mni}(\Omega)$ is represented by a Lorentzian-type distribution function

$$g_{mni}(\Omega) = \frac{1}{\pi} \frac{\gamma_{mn}}{\gamma_{mn}^2 + [(\omega_{mn} - \omega_i) - \Omega]^2} \quad , \quad (\text{G.15})$$

which has a maximum at ($\Omega = \omega_{mn} - \omega_i$), and ($\gamma_{mn} > 0$) determines the width of the distribution (G.15), corresponding to a combined system-bath frequency ($\omega_{mn} - \omega_i$). The γ_{mn} are treated here as empirical parameters, determined from criteria discussed in Sec. 4.2.2. Within the quiresonant model used here, we keep only the sum frequencies $\omega_i + \omega_j$ in Eq. (G.14) and suppose that the Bose-Einstein distribution functions $\bar{n}(\Omega)$ can be reasonably approximated by their "central values" ($\bar{n}(\omega_{mn} - \omega_i)$) in each frequency interval ($A_{mn} \leq \Omega \leq B_{mn}$). Taking into account that the bath is supposed to be in thermal equilibrium at all times, we assume that the energy exchange among the system and the bath at a certain system frequency ω_{mn} is not affected by those occurring at other system frequencies. We therefore allow the respective distributions $g_{mni}(\Omega)$ defined by Eq. (G.15) to be overlapping and set ($A_{mn} = -\infty$) and ($B_{mn} = \infty$). This yields tabulated integrals [192] in Eq. (G.14), which finally reads as follows:

$$\begin{aligned} & \sum_j^M \Phi(\omega_i, t - t', T) \Phi(\omega_j, t - t', T) \Rightarrow \\ & \Rightarrow \sum_{m=1}^{v_{max}} \sum_{n=0}^{m-1} \exp(-\gamma_{mn}|t - t'|) \{ [\bar{n}(\omega_i) + 1] [\bar{n}(\omega_{mn} - \omega_i) + 1] \exp[-i\omega_{mn}(t - t')] \\ & \quad \bar{n}(\omega_i) \bar{n}(\omega_{mn} - \omega_i) \exp[i\omega_{mn}(t - t')] \} \quad . \quad (\text{G.16}) \end{aligned}$$

Equation (G.11) is the basic equation of motion in the present work for the investigation of the non-Markovian dissipative quantum dynamics of the system driven by the IR laser field. Through the relaxation terms, it depends on all previous times. It has been solved by using several modifications of standard numerical methods [193], in particular, the Adams-Bashforth-Moulton schemes for a predictor-corrector method similar to the previous works [190, 191, 194–196]. The solution of Eq. (G.11) yields the reduced density matrix elements $\rho_{nn'}^I(t)$ of which, in particular, the time-dependent populations

$$P_n(t) = \rho_{nn}^I(t) \quad (\text{G.17})$$

are interesting for the comparison of Markovian and non-Markovian theories for the two-dimensional model of H/Si(100) in Sec. 4.2.2.

Appendix H

Local control of vibrational excitation in a non-dissipative system

In order to gain experience on whether and how the C–O internal stretch mode r and the CO-surface stretch mode Z are IR-excitabile, local control theory (LCT) calculations are done for the two-dimensional model of CO/Cu(100) (Sec. 3.1.1) in the non-dissipative case, *i. e.* all energy relaxation and dephasing rates $\Gamma_{i \rightarrow j}$ and γ_{ij} are zero. Therefore, a time-evolution in the wavepacket picture according to Eq. (2.4) is sufficient; in the implementation done in this work a SPO propagator (Appendix D) is used. The control field is generated according to Eq. (2.45), obeying the objective functional (2.44) as proposed by Ohtsuki *et al.* in Ref. [35].

In the following, for illustration, pure excitations in r are presented. We also applied the method for the excitation of the Z mode and of (r, Z) combination modes, which will not be described here for brevity.

Shown in Fig. (H.1) is the simplest, possible approach for an excitation in the r mode: From states $|n_r = 0, n_Z = 0\rangle \equiv |0\rangle$ and $|n_r = 1, n_Z = 0\rangle \equiv |1\rangle$ a two-level model is constructed, see the sketch on the left bottom corner of Fig. (H.1). The target operator is a projection operator on state $|1\rangle$, *i. e.* $\hat{O} = |1\rangle\langle 1|$. The control time was chosen as $t_f = 2.0$ ps.

In the case presented in Fig. (H.1), a time-independent penalty factor $\alpha \neq f(t) = 57$ is found to be the largest possible for complete population inversion $|0\rangle \rightarrow |1\rangle$. The maximum intensity of the pulse is $2.2 \cdot 10^{11} \text{ W/cm}^2$ and its fluence 30 mJ/cm^2 . As typical for local control pulses, due to the single forward propagation plus optimization mechanism, the pulse starts as “flatline” with $F_z(t) \approx 0$ till about $t = 900 \text{ fs}$, then a highly symmetric pulse, at first glance resembling a π pulse and of an approximate duration of 1 ps, completely transfers the population from state $|0\rangle$ to state $|1\rangle$. The envelope function of a 1 ps π pulse of \sin^2 -shape is also shown in the figure. According to Eqs. (2.39) and (2.40) and a \sin^2 shape function

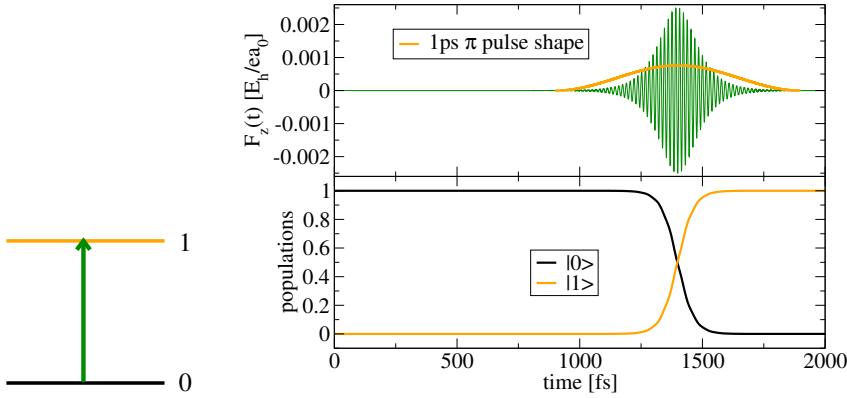


Figure H.1: Excitation of the fundamental transition in $r |0,0\rangle \rightarrow |1,0\rangle$ within a two-state model of CO/Cu(100) (see sketch in the left bottom corner), where $|0,0\rangle \equiv |0\rangle$ and $|1,0\rangle \equiv |1\rangle$. The parameters for the LCT calculation are: control time $t_f = 2 \text{ ps}$, penalty factor $\alpha = 57$ and target operator $\hat{O} = |1\rangle\langle 1|$. The upper panel displays the obtained local control field and, for comparison the shape of the \sin^2 -shaped π pulse of 1000 fs (centered at $t = 1400 \text{ fs}$), and the lower panel the associated population dynamics of states $|0\rangle$ and $|1\rangle$.

$s(t) = \sin^2\left(\frac{\pi t}{t_f}\right)$ the fluence f of a π pulse transferring population from state $|0\rangle$ to state $|1\rangle$ is

$$f^\pi = 3\epsilon_0 c \frac{1}{t_f} \left(\frac{\pi \hbar}{2|\mu_{01}|} \right)^2, \quad (\text{H.1})$$

where $|\mu_{01}|$ is the absolute transition dipole moment (here: $|\mu_{01}| = 0.20 \text{ ea}_0$, compare Table 3.5). Its maximum intensity is

$$I_{\max}^\pi = \frac{1}{2} \epsilon_0 c |F_0^\pi|^2 = 2\epsilon_0 c \left(\frac{\pi \hbar}{t_f |\mu_{01}|} \right)^2 \quad (\text{H.2})$$

Taking $t_f = 1.0 \text{ ps}$ for the π pulse this gives $f^\pi = 7.6 \text{ mJ/cm}^2$ and $I_{\max}^\pi = 2.0 \cdot 10^{10} \text{ W/cm}^2$. Comparing this to the values of the LCT pulse, one sees that the shape of latter is considerably

“sharper”, leading to an intensity 10 times larger than in case of the π pulse and accordingly also to an almost 4 times larger fluence. For strongly dissipative cases, such “sharp” pulses, where also the population inversion occurs faster than in case of a π pulse, should, although more energetic, prove more successful.

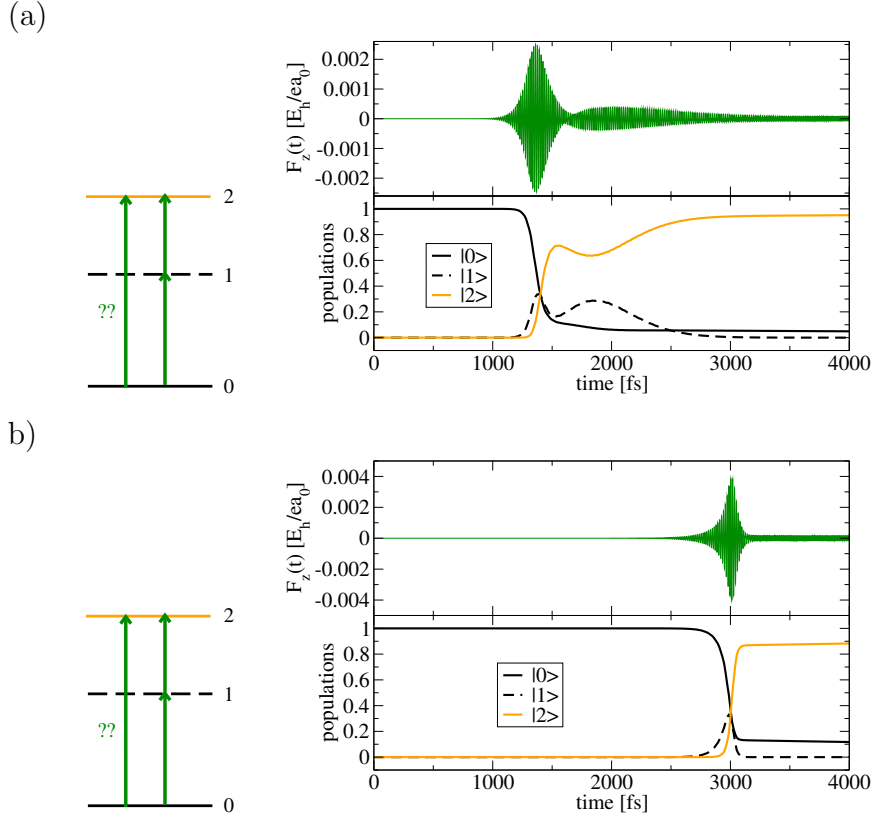


Figure H.2: Hot band excitation in r within a non-dissipative three-state model of CO/Cu(100) (see sketches on the left), where $|0,0\rangle \equiv |0\rangle$, $|1,0\rangle \equiv |1\rangle$ and $|2,0\rangle \equiv |2\rangle$. Taken for both LCT calculations (a) and (b) are the parameters $t_f = 3$ ps and $\alpha = 25$, but two different target operators as described in the text. The upper and lower panels show LCT field and population dynamics, respectively. Maximum intensities are $2.2 \cdot 10^{11}$ W/cm² (a) and $5.7 \cdot 10^{11}$ (b); pulse fluences are 36 J/cm² (a) and 48 mJ/cm² (b) and populations at $(t = t_f)$ are $P_0 = 0.049122$, $P_1 = 0.000022$, $P_2 = 0.950856$ (a) and $P_0 = 0.117392$, $P_1 = 0.000002$, $P_2 = 0.882606$ (b).

The next question to be addressed, is whether a hot-band excitation $|0\rangle \rightarrow |1\rangle \rightarrow |2\rangle$, with $|2\rangle \equiv |2,0\rangle$ is feasible and whether the direct pathway to transfer population to the target state $|2\rangle$, $|0\rangle \rightarrow |2\rangle$, plays a role. Again a minimal model, this time with 3 states, is set up, see also the sketches on the left side of Fig. H.2, where the two- and one-photon excitation mechanisms to reach state $|2\rangle$ are depicted. The control time t_f is chosen as 4 ps as shorter values deliver too intense pulses within this LCT scheme and for both calculations (a) and (b) the penalty factor α is 25. Two different target operators were chosen: $\hat{O} = 0.45 |1\rangle\langle 1| + 0.55 |2\rangle\langle 2|$ in case of (a) and $\hat{O} = 0.2 |1\rangle\langle 1| + 0.8 |2\rangle\langle 2|$ in case of (b). Note that $\hat{O} = |2\rangle\langle 2|$ does not yield any useful result (that is at least some percentage of population is transferred to state $|2\rangle$) for reasonable pulse parameters. These two examples show, how local control, although lacking an iterative mechanism and thus a clear definition of a boundary condition at $(t = t_f)$, the target operator \hat{O} influences the OCT pulse. In case (a), where state $|1\rangle$ and $|2\rangle$ have almost the same weight, the pulse sets in earlier, is less intense, chooses a reaction path where state $|1\rangle$ is intermediately populated for more than one picosecond, and “pushes” population into the target in two “waves” and is more successful to depopulate the ground state $|0\rangle$. In the other case, where more weight is laid on state $|2\rangle$, the “flatline” goes beyond $(t = 2 \text{ ps})$, the pulse is short, intense, does not show any sub-structure as in case (a) and the intermediate population of state $|1\rangle$ lasts only for ca. 500 fs. Both pulses display a cw-like “tail” in the end, this is due to the fact that in both cases the population transfer to state $|2\rangle$ is not 100 % and the algorithm tries to improve this until the end of control time. In both cases, the final target population can still be improved by smaller α values, but it is not possible to reach 100 % within reasonable pulse intensities and fluences – on the contrary in case (b) where from a certain α on the outcome gets worse, as the shorter (actual) pulse here is more prone to stimulated emission, which causes population transfer $|2\rangle \rightarrow |1\rangle \rightarrow |0\rangle$.

The question, whether direct excitation $|0\rangle \rightarrow |2\rangle$ happens can not be answered from the population dynamics alone, therefore the Husimi distributions of both pulses (a) and (b) are calculated according Eq. (2.55) and shown in Fig. H.3 (a) and (b) respectively. In both cases $(n_r + 1)$ transitions dominate, at higher frequencies (not shown for better resolution) the Husimi distribution shows only negligible contributions for an additional $(n_r + 2)$ excitation. The energy pattern in case of (a) reveals that, at least around ca. $(t = 1000 - 2000 \text{ fs})$, both processes $|0\rangle \rightarrow |1\rangle$ (setting in some hundred fs earlier) and $|1\rangle \rightarrow |2\rangle$ are triggered by the pulse via two contributions of higher and lower energy respectively. This fits well with population dynamics as depicted in Fig. (H.2) (a). Interestingly, neither frequency matches the exact resonance frequencies of 2152 and 2127 cm^{-1} , one is considerably larger than the

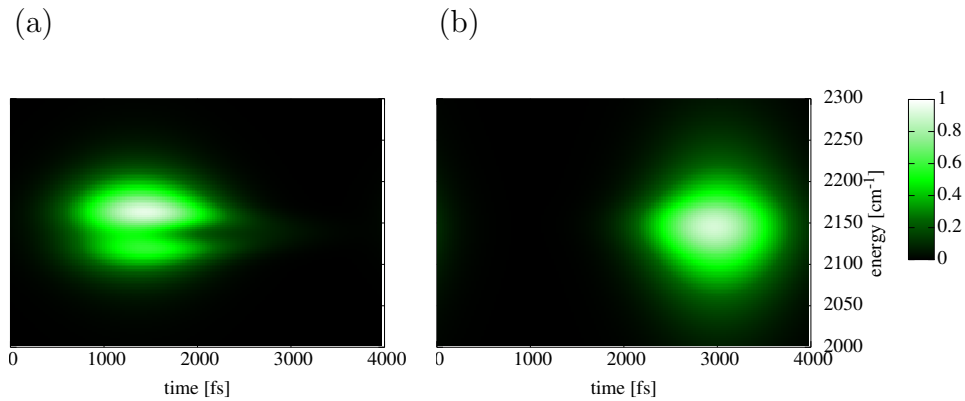


Figure H.3: Husimi plots for the two LCT pulses in Fig. H.2 (a) and (b).

former, the other slightly smaller than the latter. Pulse (b) has a signal being broader in the energy space and which does not reveal two different contributions, this is due to the higher fluence and intensities in this case. The maximum of the signal in the energy domain is again off-resonant with respect to both transition frequencies, but as the signal is so broad, considerable portions of the pulse do contain resonant contributions, thus the final target state population is lower in this case, owing to losses through stimulated emission.

Bibliography

- [1] U. Höfer, I. L. Shumay, C. Reuß, U. Thomann, W. Wallauer, and T. Fauster, *Science* **277**, 1480 (1997); M. Bauer, S. Pawlik, and M. Aeschlimann, *Phys. Rev. B* **55**, 10040 (1997); N.-H. Ge, C. M. Wong, R. L. Lingle, Jr., J. D. McNeill, K. J. Gaffney, and C. B. Harris, *Science* **279**, 202 (1998); M. Bonn, S. Funk, C. Hess, D. N. Denzler, C. Stampfl, M. Scheffler, M. Wolf, and G. Ertl, *Science* **285**, 1042 (1999); H. Petek, M. J. Weida, H. Nagano, and S. Ogakawa, *Science* **288**, 1402 (2000)
- [2] S. Thiel, M. Pykavy, T. Klüner, H.-J. Freund, R. Kosloff, and V. Staemmler, *J. Chem. Phys.* **116**, 762 (2002)
- [3] V. S. Letokhov, *Science* **180**, 451 (1973); F. F. Crim, *Science* **249**, 1387 (1990); M. Shapiro and P. Brumer, *J. Chem. Phys.* **98**, 201 (1993)
- [4] P. Saalfrank, S. Holloway, and G. R. Darling, *J. Chem. Phys.* **103**, 6720 (1995)
- [5] P. Saalfrank and T. Klamroth, *Ber. Bunsengesellschaft, Phys. Chem.* **99**, 1347 (1995)
- [6] P. Saalfrank and R. Kosloff, *J. Chem. Phys.* **105**, 2441 (1996)
- [7] G. Boendgen and P. Saalfrank, *J. Phys. Chem. B* **102**, 8029 (1998)
- [8] G. K. Paramonov and P. Saalfrank, *J. Chem. Phys.* **110**, 6500 (1999)
- [9] K. Nakagami, Y. Ohtsuki, and Y. Fujimura, *Chem. Phys. Lett.* **360**, 91 (2002)
- [10] G. K. Paramonov and P. Saalfrank, *Chem. Phys. Lett.* **301**, 509 (1999)
- [11] A. Abe, K. Yamashita, and P. Saalfrank, *Phys. Rev. B* **67**, 235411 (2003)
- [12] P. Saalfrank and G. K. Paramonov, *J. Chem. Phys.* **107**, 10723 (1997)

- [13] I. Hussla, H. Seki, T. J. Chuang, Z. W. Gortel, H. J. Kreuzer, and P. Piercy, *Phys. Rev. B* **32**, 3489 (1985)
- [14] Z. Liu, L. C. Feldman, N. H. Tolk, Z. Zhang, and P. I. Cohen, *Science* **312**, 1024 (2006); J. C. Tully, *Science* **312**, 1004 (2006)
- [15] H.-C. Chang and G. E. Ewing, *J. Vac. Sci. Technol. A* **9**, 2644 (1990); H.-C. Chang and G. E. Ewing, *Phys. Rev. Lett.* **65**, 2125 (1990)
- [16] P. Guyot-Sionnest, P. Dumas, Y. J. Chabal, and G. Higashi, *Phys. Rev. Lett.* **64**, 2156 (1990); Y. J. Chabal, *J. Mol. Struct.* **292**, 65 (1993)
- [17] Y.-Y. Sun, H. Gai, and G. A. Voth, *Chem. Phys.* **205**, 11 (1996)
- [18] K. Laß, X. Han, and E. Hasselbrink, *J. Chem. Phys.* **123**, 051102 (1992)
- [19] R. P. Chin, X. Blase, Y. R. Shen, and S. G. Louie, *Europhys. Lett.* **30**, 399 (1995)
- [20] M. Morin, N. J. Levinos, and A. L. Harris, *J. Chem. Phys.* **96**, 3950 (1992)
- [21] D. N. Denzler, C. Frischkorn, M. Wolf, and G. Ertl, *J. Phys. Chem. B* **108**, 14503 (2004)
- [22] A. P. Peirce, A. Dahleh, and H. Rabitz, *Phys. Rev. A* **37**, 4950 (1988)
- [23] S. Shi, A. Woody, and H. Rabitz, *J. Chem. Phys.* **88**, 6870 (1988)
- [24] S. Shi and H. Rabitz, *J. Chem. Phys.* **92**, 364 (1990)
- [25] W. Jakubetz, J. Manz, and H.-J. Schreier, *Chem. Phys. Lett.* **165**, 100 (1990).
- [26] R. Kosloff, R. A. Rice, P. Gaspard, S. Tersigni, and D. J. Tannor, *Chem. Phys.* **139**, 201 (1989)
- [27] J. E. Combariza, B. Just, J. Manz, and G. K. Paramonov, *J. Phys. Chem.* **95**, 10351 (1991)
- [28] A. Bartana, R. Kosloff, and D. J. Tannor, *J. Chem. Phys.* **99**, 196 (1993)
- [29] A. Bartana, R. Kosloff, and D. J. Tannor, *J. Chem. Phys.* **106**, 1435 (1997)
- [30] Y. Ohtsuki, W. Zhu, and H. Rabitz, *J. Chem. Phys.* **110**, 9825 (1999)
- [31] C. M. Tesch, L. Kurtz, and R. de Vivie-Riedle, *Chem. Phys. Lett.* **343**, 633 (2001); C. M. Tesch and R. de Vivie-Riedle, *Phys. Rev. Lett.* **89**, 157901 (2002)

- [32] J. P. Palao and R. Kosloff, *Phys. Rev. Lett.* **89**, 188301 (2002)
- [33] Y. Ohtsuki, G. Turinici, and H. Rabitz, *J. Chem. Phys.* **120**, 5509 (2004)
- [34] Y. Ohtsuki, H. Kono, and Y. Fujimura, *J. Chem. Phys.* **109**, 9318 (1998)
- [35] Y. Ohtsuki, Y. Yahata, H. Kono, and Y. Fujimura, *Chem. Phys. Lett.* **287**, 627 (1998)
- [36] M. Head-Gordon and J. C. Tully, *J. Chem. Phys.* **96**, 3939 (1992)
- [37] J. C. Tully, M. Gomez, and M. Head-Gordon, *J. Vac. Sci. Technol. A* **11**, 1914 (1993)
- [38] S. Hervé and R. Marquardt, *Mol. Phys.* **103**, 1075 (2005)
- [39] C. J. Hirschmugl, G. P. Williams, F. M. Hofmann, and Y. J. Chabal, *Phys. Rev. Lett.* **65**, 480 (1990); F. Hofmann and J. P. Toennies, *Chem. Rev. (Washington D.C.)* **96**, 1307 (1996); A. P. Graham, F. Hofmann, G. P. Williams, C. J. Hirschmugl, and J. Ellis, *J. Chem. Phys.* **108**, 7825 (1998)
- [40] S. C. Park, J. M. Bowman, and D. A. Jelski, *J. Chem. Phys.* **104**, 2457 (1996)
- [41] L. M. Struck, L. J. Richter, S. A. Buntin, R. R. Cavanagh, and J. C. Stephenson, *Phys. Rev. Lett.* **77**, 4576 (1996)
- [42] S. Carter, S. J. Culik, and J. M. Bowman, *J. Chem. Phys.* **107**, 10458 (1997)
- [43] A. Bahel and Z. Bačić, *J. Chem. Phys.* **111**, 11164 (1999)
- [44] C. Cattarius and H.-D. Meyer, *J. Chem. Phys.* **121**, 9283 (2004)
- [45] Y. Nagata, Y. Tanimura, and S. Mukamel, *J. Chem. Phys.* **126**, 204703 (2007)
- [46] M. Luppi, R. A. Olsen, and E. J. Baerends, *Phys. Chem. Chem. Phys.* **8**, 688 (2006)
- [47] J. K. Vincent, R. A. Olsen, G. J. Kroes, M. Luppi, and E. J. Baerends, *J. Chem. Phys.* **122**, 044701 (2005)
- [48] A. C. Luntz, M. Persson, S. Wagner, C. Frischkorn, and M. Wolf, *J. Chem. Phys.* **124**, 244702 (2006)
- [49] S. Wagner, C. Frischkorn, M. Wolf, M. Rutkowski, H. Zacharias, and A. C. Luntz, *Phys. Rev. B.* **72**, 205404 (2005)
- [50] D. N. Denzler, C. Frischkorn, M. Wolf, and G. Ertl, *J. Phys. Chem. B* **108**, 14503 (2004)

- [51] I. Andrianov and P. Saalfrank, Chem. Phys. Lett. **350**, 191 (2001)
- [52] I. Andrianov and P. Saalfrank, J. Chem. Phys. **124**, 034710 (2006)
- [53] P. Guyot-Sionnest, P. H. Lin, and E. M. Miller, J. Chem. Phys. **102**, 4269 (1995)
- [54] K. Blum, *Density Matrix Theory and Applications* (Plenum, New York, 1989)
- [55] K. Finger and P. Saalfrank, Chem. Phys. Lett. **268**, 291 (1997)
- [56] D. Kröner, T. Klamroth, M. Nest, and P. Saalfrank, Appl. Phys. A: Mater. Sci. Process. **88**, 535 (2007)
- [57] G. Lindblad, Commun. Math. Phys. **48**, 119 (1976)
- [58] P. Saalfrank, Chem. Phys. **268**, 291 (1996)
- [59] K. Finger and P. Saalfrank, J. Chem. Phys. **93**, 2859 (1997)
- [60] L. I. Schiff, *Quantum Mechanics*, 3rd ed. (McGraw-Hill, New York, 1968), p. 379
- [61] P. Roman, *Advanced Quantum Theory* (Addison-Wesley, Reading, Massachusetts, 1965), p. 93
- [62] W. H. Louisell, *Quantum Statistical Properties of Radiation*, (Wiley, New York, 1973), p. 76
- [63] A. G. Redfield, IBM J. Res. Dev. **1**, 19 (1957)
- [64] K. Mølmer, Y. Castin, and J. Dalibard, J. Opt. Soc. Am. B **10**, 524 (1993)
- [65] V. Gorini, A. Kossakowski, and E. C. G. Sudarshan, J. Math. Phys. **17**, 821 (1976)
- [66] D. E. Makarov and H. Metiu, J. Chem. Phys. **111**, 10126 (1999)
- [67] J. C. Tully in *Dynamics of Molecular Collision*, edited by W. H. Miller (Plenum, New York, 1976)
- [68] See for example, M. Weissbluth, *Atoms and Molecules* (Academic, New York, 1978)
- [69] M. Born and J. R. Oppenheimer, Ann. Phys. **84**, 457 (1927)
- [70] See for example, A. Szabo and N. S. Ostlund, *Modern Quantum Chemistry: Introduction to Advanced Electronic Structure Theory* (MacMillan Publishing Co. Inc., New York, 1982)

- [71] P. Bořr, Chem. Phys. Lett. **345**, 331 (2001)
- [72] M. Nest and P. Saalfrank, Chem. Phys. **268**, 65 (2001)
- [73] A. L. Harris, N. J. Levinos, L. Rothberg, L. H. Dubois, L. Dhar, S. F. Shane, and M. Levinos, J. Electron Spectrosc. Relat. Phenom. **54/55**, 5 (1990)
- [74] A. Frigerio and V. Gorini, J. Math. Phys. **17**, 123 (1976); R. Kosloff, M. A. Ratner, and W. B. Davis, J. Chem. Phys. **106**, 7036 (1997)
- [75] G. K. Paramonov, I. Andrianov, and P. Saalfrank, J. Phys. Chem. C **111**, 5432 (2007)
- [76] P. Brumer and M. Shapiro, Chem. Phys. Lett. **126** 541 (1986)
- [77] P. Gross, D. Neuhauser, and H. Rabitz, J. Chem. Phys. **96**, 2834 (1992)
- [78] M. Sugawara and Y. Fujimura, J. Chem. Phys. **100**, 5646 (1994)
- [79] M. Sugawara and Y. Fujimura, J. Chem. Phys. **101**, 6586 (1994)
- [80] K. Sundermann and R. de Vivie-Riedle, J. Chem. Phys. **110**, 1896 (1999)
- [81] M. Artamonov, T.-S. Ho, and H. Rabitz, J. Chem. Phys. **124**, 064306 (2006)
- [82] M. Kono, K. Hoki, H. Kono, and Y. Fujimura, J. Chem. Phys. **127**, 204314 (2007)
- [83] E. Räsänen, A. Castro, J. Werschnik, A. Rubio, and E. K. U. Gross, Phys. Rev. Lett. **98**, 157404 (2007)
- [84] D. J. Tannor, V. Kazakov, and V. Orlov, *Time-Dependent Quantum Molecular Dynamics*, Vol. **299** of NATO ASI, Series B: Physics, edited by J. Broeckhove and L. Lathouwers (Plenum, New York, 1992)
- [85] W. Zhu, J. Botina, and H. Rabitz, J. Chem. Phys. **108**, 1953 (1998)
- [86] W. Zhu and H. Rabitz, J. Chem. Phys. **109**, 385 (1998)
- [87] Y. Maday and G. Turinici, J. Chem. Phys. **118**, 8191 (2003)
- [88] T. Hornung, M. Motzkus, and R. de Vivie-Riedle, J. Chem. Phys. **115**, 3105 (2001)
- [89] J. C. Butcher, Math. Comp. **18**, 50 (1964)
- [90] J. C. Butcher, BIT Num. Math. **16**, 237 (1976)

- [91] Y.-J. Yan, R. E. Gillilan, R. M. Whitnell, K. R. Wilson, and S. Mukamel, *J. Phys. Chem.* **97**, 2320 (1993)
- [92] Z. Nehari, *Conformal Mapping* (McGraw-Hill, New York, 1952)
- [93] T. A. Driscoll and L. N. Trefethen, *Schwarz-Christoffel Mapping* (Cambridge University Press, Cambridge, 2002)
- [94] E. Wigner, *Phys. Rev.* **40**, 749 (1932)
- [95] K. Husimi, *Prog. Phys. Math. Soc. Japan* **22**, 264 (1940)
- [96] S. Beyvers, Y. Ohtsuki, and P. Saalfrank, *J. Chem. Phys.* **124**, 234706 (2006)
- [97] J. C. Tremblay, S. Beyvers, and P. Saalfrank, *J. Chem. Phys.* **128**, 194709 (2008)
- [98] D. T. Colbert and W. H. Miller, *J. Chem. Phys.* **96**, 1982 (1992)
- [99] H.-D. Meyer, U. Manthe, and L. S. Cederbaum, *Chem. Phys. Lett.* **165**, 73 (1990)
- [100] G. A. Worth, M. H. Beck, A. Jäckle, and H.-D. Meyer, *The MCTDH Package*, Version 8.2 (2000); H.-D. Meyer, Version 8.3 (2002)
- [101] K. Hermann, P. S. Bagus, and C. W. Bauschlicher, Jr., *Phys. Rev. B* **30**, 7313 (1984)
- [102] J. M. Ricard, A. Clotet, F. Illas, and J. Rubio, *J. Chem. Phys.* **100**, 1988 (1994)
- [103] S. Beyvers, *Quantum Chemical Calculations of Vibrational Lifetimes of Adsorbates on Metal Surfaces*, Diploma Thesis (Universität Regensburg, 2005)
- [104] G. K. Paramonov, S. Beyvers, I. Andrianov, and P. Saalfrank, *Phys. Rev. B* **75**, 045405 (2007)
- [105] A. Dyson and P. Smith, *Surf. Sci.* **355**, 140 (1996)
- [106] A. Dyson and P. Smith, *Mol. Phys.* **96**, 1491 (1999)
- [107] C. Sbraccia, P. Silvestrelli, and F. Ancilotto, *Surf. Sci.* **519**, 147 (2002)
- [108] GAUSSIAN 03, Revision C.02, M. J. Frisch, G. W. Trucks, H. B. Schlegel, G. E. Scuseria, M. A. Robb, J. R. Cheeseman, J. A. Montgomery, Jr., T. Vreven, K. N. Kudin, J. C. Burant, J. M. Millam, S. S. Iyengar, J. Tomasi, V. Barone, B. Mennucci, M. Cossi, G. Scalmani, N. Rega, G. A. Petersson, H. Nakatsuji, M. Hada, M. Ehara, K. Toyota, R. Fukuda, J. Hasegawa, M. Ishida, T. Nakajima, Y. Honda, O. Kitao, H. Nakai,

M. Klene, X. Li, J. E. Knox, H. P. Hratchian, J. B. Cross, V. Bakken, C. Adamo, J. Jaramillo, R. Gomperts, R. E. Stratmann, O. Yazyev, A. J. Austin, R. Cammi, C. Pomelli, J. W. Ochterski, P. Y. Ayala, K. Morokuma, G. A. Voth, P. Salvador, J. J. Dannenberg, V. G. Zakrzewski, S. Dapprich, A. D. Daniels, M. C. Strain, O. Farkas, D. K. Malick, A. D. Rabuck, K. Raghavachari, J. B. Foresman, J. V. Ortiz, Q. Cui, A. G. Baboul, S. Clifford, J. Cioslowski, B. B. Stefanov, G. Liu, A. Liashenko, P. Piskorz, I. Komaromi, R. L. Martin, D. J. Fox, T. Keith, M. A. Al-Laham, C. Y. Peng, A. Nanayakkara, M. Challacombe, P. M. W. Gill, B. Johnson, W. Chen, M. W. Wong, C. Gonzalez, and J. A. Pople, Gaussian, Inc., Wallingford CT, 2004

- [109] G. K. Paramonov, I. Andrianov, and P. Saalfrank, *J. Phys. Chem.* **111**, 5432 (2007)
- [110] T. Klamroth and P. Saalfrank, *J. Chem. Phys.* **112**, 10571 (2000)
- [111] T. Vazhappilly, S. Beyvers, T. Klamroth, M. Luppi, and P. Saalfrank, *Chem. Phys.* **338**, 299 (2007)
- [112] P. Feulner and D. Menzel, *Surf. Sci.* **154**, 465 (1985)
- [113] I. M. Ciobîcă, F. Frechard, R. A. van Santen, A. W. Kleyn, and J. Hafner, *Chem. Phys. Lett.* **311**, 185 (1999)
- [114] B. Hammer, L. B. Hansen, and J. K. Nørskov, *Phys. Rev. B* **59**, 7413 (1999)
- [115] H. Shi and K. Jacobi, *Surf. Sci.* **313**, 289 (1994)
- [116] A. D. Becke, *J. Chem. Phys.* **98**, 5648 (1993); C. F. Chabalowski, M. J. Frisch, P. J. Stevens, and J. F. Devlin, *J. Phys. Chem* **98**, 11623 (1994)
- [117] P. J. Hay and W. R. Wadt, *J. Chem. Phys.* **82**, 270 (1985)
- [118] M. W. Schmidt, K. K. Baldrige, J. A. Boatz, S. T. Elbert, M. S. Gordon, J. H. Jensen, S. Koseki, N. Matsunaga, K. A. Nguyen, S. Su, T. L. Windus, M. Dupuis, and J. A. Montgomery *J. Comput. Chem.* **14**, 1347 (1993)
- C. Keller, W. Wurth, and D. Menzel, *Phys. Rev. B* **63**, 205419 (2001)
- [119] M. Bonn, C. Hess, and M. Wolf, *J. Chem. Phys.* **115**, 7725 (2001)
- [120] Y. Ohtsuki, K. Nakagami, W. Zhu, and H. Rabitz, *Chem. Phys.* **287**, 197 (2003)
- [121] T. Mančal, U. Kleinkathehöfer, and V. May, *J. Chem. Phys.* **117**, 636 (2002)

- [122] G. K. Paramonov and P. Saalfrank, Chem. Phys. Lett. **301**, 509 (1999)
- [123] D. Gerbashi, M. Shapiro, and P. Brumer, J. Chem. Phys. **115**, 5349 (2001); D. Gerbashi, M. Shapiro, and P. Brumer, J. Chem. Phys. **124**, 074315 (2006);
- [124] R. Unanyan, M. Fleischhauer, B. W. Shore, and K. Bergmann, Optics Commun. **155**, 144 (1998)
- [125] V. Kurkal and S. Rice, Chem. Phys. Lett. **344**, 125 (2001)
- [126] S. Lall, J. E. Marsden, and S. Glavaški, Int. J. Robust Nonlinear Control **12**, 519 (2002)
- [127] C. W. Rowley, Int. J. on Bifurcation and Chaos **15**, 997 (2005)
- [128] C. Hartmann, V.-M. Vulcanov, and C. Schütte, SIAM J. Control and Optimization *submitted* (2007)
- [129] S. A. Corcelli and J. C. Tully, J. Chem. Phys. **116**, 8079 (2002)
- [130] I. Grigorenko, M. E. Garcia, and K. H. Bennemann, Phys. Rev. Lett. **89**, 233003 (2002)
- [131] A. Kaiser and V. May, J. Chem. Phys. **121**, 2528 (2004)
- [132] R. Xu, J. Cheng, and Y. J. Yan, J. Phys. Chem. A **103**, 10611 (1999)
- [133] W. Zhu and H. Rabitz, J. Chem. Phys. **119**, 3619 (2003)
- [134] M. Sugawara, J. Chem. Phys. **118**, 6784 (2003)
- [135] I. Serban, J. Werschnik, and E. K. U. Gross, Phys. Rev. A **71**, 053810 (2005)
- [136] D. O. Harris, G. G. Engerholm, and W. H. Gwinn, J. Chem. Phys. **43**, 1515 (1965)
- [137] P. F. Endres, *ibid.* **47**, 798 (1967)
- [138] A. S. Dickinson and P. R. Certain, J. Chem. Phys. **49**, 4209 (1968)
- [139] Z. Bacic and J. C. Light, J. Chem. Phys. **85**, 4594 (1986)
- [140] J. V. Lill, G. A. Parker, and J. C. Light, Chem. Phys. Lett. **89**, 483 (1982)
- [141] J. C. Light, I. P. Hamilton, and J. V. Lill, J. Chem. Phys. **82**, 1400 (1985)
- [142] J. V. Lill, G. A. Parker, and J. C. Light, J. Chem. Phys. **85**, 900 (1986)
- [143] S. E. Choi and J. C. Light, J. Chem. Phys. **92**, 2129 (1990)

- [144] J. C. Light, R. M. Whitnell, T. J. Park, and S. E. Choi, NATO ASI Ser. C **277**, 187 (1989)
- [145] W. Yang and A. C. Peet, Chem. Phys. Lett. **153**, 98 (1988)
- [146] A. C. Peet and W. Yang, J. Chem. Phys. **90**, 1746 (1989)
- [147] A. C. Peet and W. Yang, J. Chem. Phys. **92**, 522 (1990)
- [148] C. C. Marston and G. G. Balint-Kurti, J. Chem. Phys. **91**, 3571 (1989)
- [149] P. A. M. Dirac, *The Principles of Quantum Mechanics* (International Series of Monographs on Physics), 4th ed. (Oxford University Press, USA, 1982)
- [150] C. Cohen-Tannouji, B. Diu, and F. Laloë, *Quantenmechanik 1*, 2. Auflage (de Gruyter, Berlin, 1999)
- [151] C. E. Shannon, Proc. Institute of Radio Engineers **37**, 10 (1949)
- [152] E. Angerson, Z. Bai, J. Dongarra, A. Greenbaum, A. McKenney, J. Du Croz, S. Hammarling, J. Demmel, C. Bischof, and D. Sorensen, University of Tennessee Computer Science Technical Report, UT-CS-90-105 (1990)
- [153] X. Wang and T. Carrington, Jr., J. Chem. Phys. **117**, 6923 (2002)
- [154] H.-G. Yu, J. Chem. Phys. **117**, 8190 (2002)
- [155] X. Wang and T. Carrington, Jr., Int. J. Quant. Chem. **99**, 556 (2004)
- [156] J. C. Tremblay and T. Carrington, Jr., J. Chem. Phys. **125**, 094311 (2006)
- [157] R. W. Freund and N. M. Nachtigal, *Linear Algebra for Large Scale and Real-Time Applications* (Kluwer Academic Publishers, 1993)
- [158] R. W. Freund and N. M. Nachtigal, SIAM J. Sci. Stat. Comp. **15**, 313 (1994)
- [159] H. O. Karlsson and S. Holmgren, J. Chem. Phys. **117**, 9116 (2002)
- [160] E. R. Davidson, J. Comput. Phys. **17**, 87 (1975)
- [161] W. H. Press, S. A. Teukolsky, W. T. Vetterling, and B. P. Flannerly, *Numerical Recipes in FORTRAN 77 The Art of Scientific Programming* (Cambridge University Press, 1986)

- [162] G. H. Golub and C. F. V. Loan, *Matrix Computations* (John Hopkins University Press, Baltimore, 1989)
- [163] F. Sartoretto, G. Pini, and G. Gambolati, *J. Comput. Phys.* **81**, 53 (1989)
- [164] L. N. Trefethen and D. Bau III, *Numerical Linear Algebra* (Society for Industrial and Applied Mathematics, Philadelphia, 1997)
- [165] Y. Saad, *Iterative methods for sparse linear systems* (Society for Industrial and Applied Mathematics, Philadelphia, 2003)
- [166] P. Arbenz, U. L. Hetmaniuk, R. B. Lehoucq, and R. S. Tuminaro, *Internat. J. Numer. Methods Engrg.* **64**, 204 (2005)
- [167] Z. Bai, J. Demmel, J. Dongarra, A. Ruhe, and H. van der Vorst, *Templates for the Solution of Algebraic Eigenvalue Problems: A Practical Guide* (Society for Industrial and Applied Mathematics, Philadelphia, 2000)
- [168] G. W. Stewart, *Matrix Algorithms volume II: Eigensystems* (Society for Industrial and Applied Mathematics, Philadelphia, 2001)
- [169] J. T. Muckerman, *Chem. Phys. Lett.* **173**, 1400 (1985)
- [170] C. Leforestier, *J. Chem. Phys.* **94**
- [171] J. Echave and D. C. Clary, *Chem. Phys. Lett.* **190**, 225 (1992)
- [172] M. J. Bramley and T. Carrington, Jr., *J. Chem. Phys.* **99**, 8519 (1993)
- [173] H. Wei, *J. Chem. Phys.* **106**, 6885 (1997)
- [174] J. C. Light and T. Carrington, Jr., *Adv. Chem. Phys.* **114**, 263 (2000)
- [175] H.-G. Yu, *J. Chem. Phys.* **122**, 164107 (2005)
- [176] H. Köppel, W. Domke, and L. S. Cederbaum, *Adv. Chem. Phys.* **57**, 59 (1984)
- [177] R. E. Wyatt, *Adv. Chem. Phys.* **73**, 231 (1989)
- [178] A. McNichols and T. Carrington, Jr., *Chem. Phys. Lett.* **202**, 464 (1993)
- [179] M. R. Wall and D. Neuhauser, *J. Chem. Phys.* **102**, 8011 (1995)
- [180] T. P. Grozdanov, V. A. Mandelshtam, and H. S. Taylor, *J. Chem. Phys.* **103**, 7990 (1995)

- [181] H.-G. Yu and S. C. Smith, Ber. Bunsenges. Phys. Chem. **101**, 400 (1997)
- [182] R. Chen and H. Guo, J. Chem. Phys. **108**, 6068 (1998)
- [183] X. Wang and T. Carrington, Jr., **115**, 9781 (2001)
- [184] A. D. Bandrauk, E. Aubanel, and S. Chelowski, in *Femtosecond Chemistry*, edited by J. Manz and L. Wöste (Verlag Chemie, New York, 1995)
- [185] See for example, R. G. Parr and W. Yang, *Density Functional Theory for Atoms and Molecules* (Oxford University Press, New York, 1989)
- J. P. Perdew and Y. Yang, Phys. Rev. B **33**, 8800 (1986)
- A. Zupan, P. Blaha, J. P. Perdew, and S. Kurth, Phys. Rev. Lett. **82**, 2544 (1999)
- [186] A. D. Becke, Phys. Rev. A **38**, 3098 (1988)
- [187] W. Yang, R. G. Parr, and C. Lee, Phys. Rev. B, **37**, 785 (1985)
- [188] G. Frenking, I. Antes, M. Böhme, S. Dapprich, A. W. Ehlers, V. Jonas, A. Nauhaus, M. Otto, R. Stegmann, A. Veldkamp, and S. F. Vyboishchikov, Rev. Comput. Chem. **8**, 63 (1996); T. R. Cundari, M. T. Benson, M. L. Lutz, and S. O. Sommerer, Rev. Comput. Chem. **8**, 145 (1996)
- [189] R. Krishnan, J. S. Binkley, R. Seeger, and J. A. Pople, J. Chem. Phys. **72**, 650 (1980)
- [190] M. V. Korolkov and G. K. Paramonov, Phys. Rev. A **55**, 589 (1997)
- [191] P. Saalfrank and G. K. Paramonov, J. Chem. Phys. **110**, 6500 (1999)
- [192] I. S. Gradshteyn and I. M. Ryzhik, *Table of Integrals, Series, and Products* (Academic Press, New York, 1980)
- [193] W. H. Press, B. P. Flannery, S. A. Teukolsky, and W. T. Vetterling, *Numerical Recipes* (Cambridge University Press, Cambridge, 1986)
- [194] M. V. Korolkov, J. Manz, and G. K. Paramonov, J. Phys. Chem. **101**, 13927 (1996)
- [195] M. V. Korolkov, J. Manz, and G. K. Paramonov, J. Chem. Phys. **105**, 10874 (1996)
- [196] M. V. Korolkov and G. K. Paramonov, Phys. Rev. A **56**, 3860 (1997)

Danksagung

Die vorliegende Arbeit entstand in der Zeit von Februar 2005 bis Juli 2008 am Institut für Chemie der Universität Potsdam. Ich möchte allen danken, die durch ihr direktes und indirektes Mitwirken zum Gelingen dieser Arbeit beigetragen haben.

Mein besonderer Dank gilt Herrn Prof. Dr. Peter Saalfrank, der mir diese Arbeit ermöglichte, mich hervorragend betreute und mir wertvolle Ideen und Hinweise lieferte.

Für fachliche Unterstützung bedanke ich mich weiterhin bei Dr. habil. Tillmann Klamroth, Dr. Ivan Andrianov und Dr. habil. Mathias Nest.

Für seine Freundschaft und sein Ruhe austrahlendes Wesen möchte ich mich bei Dr. Ivan Andrianov bedanken, mit dem ich mir lange Zeit das Büro teilte.

Dank gilt auch Jean Christophe Tremblay, Pascal Krause, Jadranka Dokić und Gernot Füchsel, für die gute gemeinsame Zeit, sowie allen weiteren Mitgliedern des Lehrstuhls für Theoretische Chemie der Universität Potsdam, für die angenehme Arbeitsatmosphäre.

Annika Hogeckamp möchte ich danken, für die angenehme, gemeinsame Zerstreuung in der raren Freizeit während des Zusammenschreibens.

Meinem Vater Dr. Gottfried Beyvers danke ich für seine Hilfe, Rechtschreib- und Grammatikfehler aufzuspüren.

Spezieller Dank gilt meinen Großeltern Herma und Ludwig Christl, für ihre Liebe und Unterstützung!

Erklärung

Hiermit versichere ich, dass ich die vorliegende Arbeit mit den angegebenen Hilfsmitteln selbständig angefertigt habe.

Potsdam, im Juli 2008